

AD-A053 377 ARMY ARMAMENT RESEARCH AND DEVELOPMENT COMMAND ABERD--ETC F/G 19/4
COMPUTER STUDY OF THE EFFECTS OF ROD DIAMETER AND TARGET THICKNESS--ETC(U).
FEB 78 V KUCHER

UNCLASSIFIED

ARBRL-TR-02046

SBIE-AD-E400 140

NL

| OF |
ADA
053377



END
DATE
FILED
6-78
DDC

AD-E100 140

ADA053377

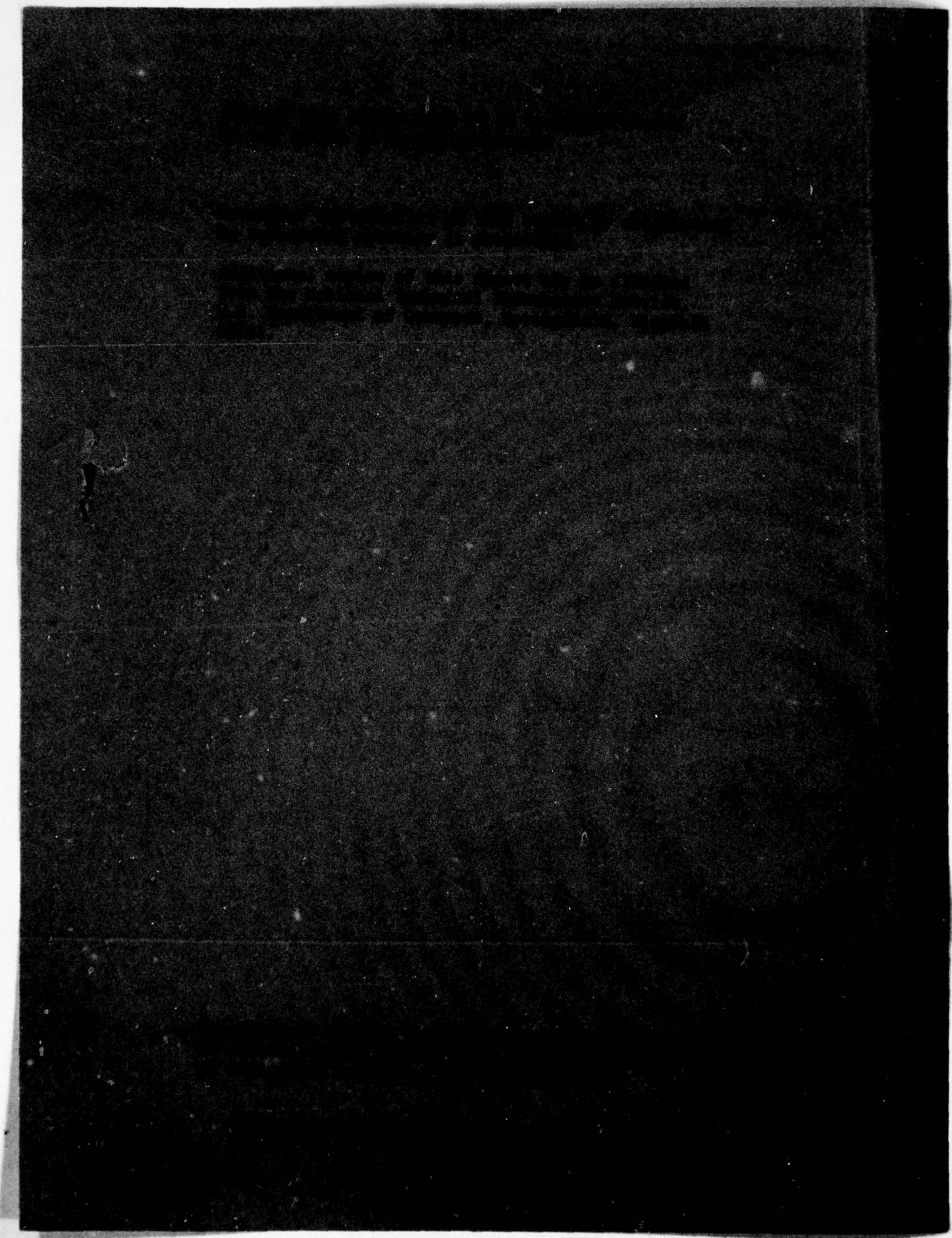
ORNL REPORT

TECHNICAL REPORT ARSRL-TR-0206

COMPUTER STUDY OF THE EFFECTS OF ROD DIAMETER AND TARGET THICKNESS ON THE PENETRATION PROCESS

V. Kucher

January 1978



UNCLASSIFIED

SECURITY CLASSIFICATION OF THIS PAGE (When Data Entered)

18

SBIE

19

AD-E400 140

REPORT DOCUMENTATION PAGE			READ INSTRUCTIONS BEFORE COMPLETING FORM
1. REPORT NUMBER TECHNICAL REPORT ARBRL-TR-92946	2. GOVT ACCESSION NO.	3. RECIPIENT'S CATALOG NUMBER	
4. TITLE (and Subtitle) COMPUTER STUDY OF THE EFFECTS OF ROD DIAMETER AND TARGET THICKNESS ON THE PENETRATION PROCESS.		5. TYPE OF REPORT OR TECHNICAL COVERED FINAL rep't.	
6. AUTHOR(s) V. Kucher		7. CONTRACT OR GRANT NUMBER(s)	
8. PERFORMING ORGANIZATION NAME AND ADDRESS US Army Ballistic Research Laboratory (ATTN: DRDAR-BLT) Aberdeen Proving Ground, MD 21005		9. PROGRAM ELEMENT, PROJECT, TASK AREA & WORK UNIT NUMBERS 1W662618AH80	
10. CONTROLLING OFFICE NAME AND ADDRESS US Army Armament Research and Development Command US Army Ballistic Research Laboratory (ATTN: DRDAR-BL) Aberdeen Proving Ground, MD 21005		11. REPORT DATE FEB 12 1978	
12. NUMBER OF PAGES 81		13. SECURITY CLASS. (of this report) UNCLASSIFIED	
14. MONITORING AGENCY NAME & ADDRESS (if different from Controlling Office)		15. DECLASSIFICATION/DOWNGRADING SCHEDULE	
16. DISTRIBUTION STATEMENT (of this Report) Approved for public release; distribution unlimited.			
17. DISTRIBUTION STATEMENT (of the abstract entered in Block 20, if different from Report) REF ID: A21111 B			
18. SUPPLEMENTARY NOTES			
19. KEY WORDS (Continue on reverse side if necessary and identify by block number) Penetration Mechanics Hypervelocity Impact Shaped-Charge Penetration Two-Dimensional Computer Code Eulerian Computer Code			
20. ABSTRACT (Continue on reverse side if necessary and identify by block number) A computer parametric study of the 7.5 km/s impact of a long, slender, copper rod on a steel target was made to obtain hole growth information. The rod radius was varied (1, 3, and 9 mm) and the target thickness was varied (7.5 and 37.5 mm). In addition to hole growth histories, penetration histories and pressure and particle velocity profiles along the axis of symmetry of the rod are presented.			

DD FORM 1 JAN 73 1473

EDITION OF 1 NOV 68 IS OBSOLETE

UNCLASSIFIED

1 SECURITY CLASSIFICATION OF THIS PAGE (When Data Entered)

393 471

See

TABLE OF CONTENTS

	Page
LIST OF ILLUSTRATIONS	5
I. INTRODUCTION	7
II. COMPUTER CODE	7
III. ROD-TARGET CONFIGURATION	7
IV. COMPUTATIONAL GRID	8
V. COMPUTER RESULTS, 7.5-MM TARGET	9
A. Computer Output	9
B. Tracer Particle Motion	9
C. Pressure and Particle Velocity	10
VI. COMPUTER RESULTS, 37.5-MM TARGET	11
A. Computer Output	11
B. Tracer Particle Motion	11
C. Pressure and Particle Velocity	11
VII. DISCUSSION	12
ACKNOWLEDGMENTS	13
DISTRIBUTION LIST	79

ACCESSION for	
NTIS	White Section <input checked="" type="checkbox"/>
DDC	Buff Section <input type="checkbox"/>
UNANNOUNCED	<input type="checkbox"/>
JUSTIFICATION _____	
BY _____	
DISTRIBUTION/AVAILABILITY CODES	
Dist. AVAIL and/or SPECIAL	
A	

LIST OF ILLUSTRATIONS

Figure	Page
1. Grid Configuration for a 1-mm Radius Rod.	14
2. Grid Configuration for a 3-mm Radius Rod.	15
3. Grid Configuration for a 9-mm Radius Rod.	16
4-13. Comparison of the Deformation of a 7.5-mm Steel Target Impacted by 1, 3, and 9-mm Copper Rods.	17
14. Position of the Rod-Target Interface on the Axis of Symmetry Versus Time.	27
15. Comparison of Hole Growth	28
16-25. Comparison of Pressure and Velocity Profiles.	29
26. Comparison of Pressure Profiles along the Axis of Symmetry.	39
27-45. Comparison of the Deformation of a 37.5-mm Steel Target Impacted by 1, 3, and 9-mm Copper Rods.	40
46. Position of the Rod-Target Interface on the Axis of Symmetry Versus Time.	59
47. Comparison of Hole Growth	60
48-64. Comparison of Pressure and Velocity Profiles.	61
65. Comparison of Pressure Profiles along the Axis of Symmetry.	78

I. INTRODUCTION

In order to model hole growth in a target impacted by a high-speed, long, slender rod, experimental and analytical data are required. A method of generating analytical data is through the use of hydrodynamic computer codes. A parametric study, using the DORF-9 code, was made by varying the rod radius and the target thickness while holding the rod and target materials and rod impact velocity constant. Some of the enormous amount of data that were generated from running the code are presented here. These data are useful not only for studying hole growth, which has been modeled from these data¹, but also for increasing the understanding of the impact phenomena and for providing data for setting up future computer runs.

II. COMPUTER CODE

The DORF-9 code² was used to generate data on the impact phenomena. The code is a two-dimensional, multimaterial, continuous, Eulerian, hydrodynamic code coupled with an elastic-plastic strength model. An option of Cartesian (x,y) or cylindrically symmetric (r,z) coordinates is available in the code. Also, tracer particles can be used to provide a Lagrangian look to the plotted output. The code was run on the high-speed digital computer, BRLESC-2, which is located at the Ballistic Research Laboratory.

III. ROD-TARGET CONFIGURATION

In all the cases that were run on the computer, the impact was normal (zero obliquity), thus permitting the problem to be considered as being axisymmetric. The rod was treated as being semi-infinite in length with a constant diameter and a uniform initial velocity in contrast to a rod with an initial velocity gradient in it. The rod was copper with radii of 1, 3, and 9 mm.

The steel target was an infinite plate with thicknesses of 7.5 and 37.5 mm being considered. The stationary target was impacted by the rod at 7.5 km/s.

-
1. J. Majerus, V. Kucher, and A. Merendino, "A Hole Growth Model for Target Impact by Shaped Charge Jets," Ballistic Research Laboratory Memorandum Report to be published.
 2. W. E. Johnson, "Development and Application of Computer Programs Related to Hypervelocity Impact," Systems, Science and Software, 3SR-749, AD 889143, July 1971.

IV. COMPUTATIONAL GRID

A computational grid was laid out to cover the cross-sectional region of interest of the rod-target configuration with the rod's centerline coinciding with the z-axis. See Figures 1-3. The rod's initial motion was in the positive z-direction. The bottom boundary of the grid was selected to be transmittive, thus allowing rod material to be fed into the grid as a simulation of a semi-infinite rod. The right boundary of the grid was selected to be transmittive thus allowing the simulation of an infinite plate. The top boundary was also transmittive, permitting material to flow out of the region of interest.

The overall physical dimensions of the grid was 50 mm by 81 mm with a corresponding grid size of 35 by 90 cells. Starting at the top boundary, the length, Δz , of the first cell was 10 mm followed by 82 cells with a length of 0.625 mm. Thereafter, the length increased over the final 7 cells as a geometric progression to a maximum Δz of 6.119 mm. This system of incrementing the z-axis was used for all the cases that were run on the computer.

Depending on the radius of the rod, three different systems of incrementing the r-axis were used. For a rod radius of 1 mm (see Figure 1), starting at the left boundary, the width, Δr , of each of the first 20 cells was 0.25 mm; thereafter, the width increased over the final 15 cells as a geometric progression to a maximum Δr of 10.080 mm. For a rod radius of 3 mm (see Figure 2), starting at the left boundary, the width of each of the first 10 cells was 0.5 mm; thereafter, the width increased over the final 25 cells as a geometric progression to a maximum Δr of 4.155 mm. Finally, for a rod radius of 9 mm (see Figure 3), starting at the left boundary, the width of each of the first 30 cells was 1.0 mm; thereafter, the width increased over the final 5 cells as a geometric progression to a maximum Δr of 7.706 mm. Four or more cells, in the radial direction, were used to fill in the physical radii of the three rods³.

The cells, occupying the initial volume of the rod, were given the following initial conditions:

1. Density = 8.9 Mg/m³.
2. Pressure = 0.0 Mbar.
3. Radial velocity = 0.0 km/s.
4. Axial velocity = 7.5 km/s.
5. Specific internal energy = 0.0 J/g.

Similar initial conditions were given to the cells occupying the initial volume of the target except that the density was that of the steel target material, 7.86 Mg/m³, and the axial velocity was zero. The yield stresses in shear that were used for copper and steel were 1.275 and 6.8 kbar, respectively.

3. V. Kucher, "Preliminary Computer Computations for Slender Rod Impact Problems," Ballistic Research Laboratory Report No. 1957, Feb 1977.

In all the cases that were run, the impact surface of the target was at $z = 21$ mm on the grid. The back surface of the target was at $z = 28.5$ or 58.5 mm, depending on the target thickness of 7.5 or 37.5 mm, respectively.

V. COMPUTER RESULTS, 7.5-MM TARGET

A. Computer Output

The computational results were printed out at 0 , $\frac{1}{4}$, and $\frac{1}{2}$ μ s and at $\frac{1}{2}$ μ s intervals thereafter. The three cases of rod radii of 1, 3, and 9 mm, that were run on the computer will be referred to as R1, R3, and R9, respectively.

B. Tracer Particle Motion

The DORF-9 code has an option for incorporating tracer particles into its computations. These computations of the motion of the tracer particles are passive in that the Eulerian solution to a problem is not affected by these additional computations. The motion of a particle is determined by the weighted velocity from the cell containing the particle and from neighboring cells.

Tracer particles were initially positioned to outline the front and back surfaces of the target and the free surface of the rod. In addition, two rows of tracer particles were positioned in the target so that the deformation of the target could be recorded. Figure 4 shows the initial position of line segments which pass through the tracer particles and give a Lagrangian appearance to the computer solutions of the problems.

Figures 4 - 13 show a history of the rod-target deformation for the three radii being considered. These figures are useful for studying the depth of penetration of the rod into the target and the hole growth in the target. Figure 14 shows the penetration-time relation for the three rod radii being considered. The depth of penetration is measured from the original front surface of the target. From incompressible jet penetration theory⁴, the penetration rate is 3.87 km/s. At this rate, about 1.94μ s would be required for the rod to pass through the 7.5-mm target. However, other phenomena such as a rarefaction wave from the back surface of the target would affect the perforation time. The computer output shows the penetration rate, based on two data points, to be 3.81, 3.80, and 3.92 km/s for R1, R3, and R9, respectively, over the time period from $\frac{1}{4}$ to 1 μ s. After the rod passes the original position of the back of the target, the front of the rod takes a velocity of 6.13, 5.35, and 5.86 km/s for R1, R3, and R9, respectively. This velocity was

4. E. M. Pugh, R. J. Eichelberger, and N. Rostoker, "Theory of Jet Formation with Lined Conical Cavities," *Journal of Applied Physics*, May 1952.

determined over the time period from 3 to 4 μ s and was based on two data points.

Figures 4 - 13 were also used for measuring hole radii at the front and back surfaces of the target. These results are shown in Figure 15 where the hole radius has been nondimensionalized with respect to the radius of the rod. Over the period that the problems were run, the hole radii did not reach a steady-state value. After 4 μ s, for all cases, the hole radius at the back surface of the target was larger than the hole radius at the front surface.

C. Pressure and Particle Velocity

Pressure and material particle velocity profiles along the axis of symmetry of the rod-target configuration are shown in Figures 16 - 25. The rod-target interface on the axis of symmetry is indicated by a triangular symbol above the abscissa.

Using Tillotson's equation of state⁵ for copper and iron, we find that the rod-target interface is shocked to a pressure of 3.0 Mbar and that the particle velocity in this region is 3.92 km/s. These conditions would prevail in the interface region until the rarefaction wave from the free surface of the rod reaches the center-line of the rod. This occurs at 0.11, 0.34, and 1.02 μ s after impact for R1, R3, and R9, respectively.

Since the computer print-out at $\frac{1}{4}$ μ s occurs after the pressure in the rod was released by the rarefaction wave from the free surface of the rod, the peak pressure of 3.0 Mbar has already decayed for R1; however, for R3, the peak pressure is shown to exist in Figure 17, and for R9, in Figures 17 and 18. Beginning with Figure 19, the decay of the front of the shock wave due to the release of the pressure at the back surface of the target, which was originally at $z = 28.5$ mm, is shown.

Figure 25 shows that pressure still persists in the rod of R9 at 4 μ s in contrast to R1 and R3.

In Figures 19 - 25, the particle velocity of the back surface is of the order of the impact velocity for R9. This occurs in Figure 25 (4 μ s) for R1, but has not occurred for R3 at this time.

Figure 26 shows the pressure histories for the three cases over a period of $2\frac{1}{2}$ μ s. In each case a steady-state pressure was not attained. Furthermore, each case produced different pressure histories. For R9, the pressure release came from the front of the pressure wave; for R1 and R3, the pressure release came from the rear of the pressure wave.

5. J. H. Tillotson, "Metallic Equations of State for Hypervelocity Impact," Gulf General Atomic, GA-3216, July 1962.

VI. COMPUTER RESULTS, 37.5-MM TARGET

A. Computer Output

The computational results were printed out at 0, $\frac{1}{4}$, and $\frac{1}{2}$ μ s and at $\frac{1}{2}$ - μ s intervals between $\frac{1}{2}$ and 5 μ s and 1- μ s intervals thereafter. The three cases of rod radii of 1, 3, and 9 mm, that were run on the computer, will be referred to as R1X, R3X, and R9X, respectively.

B. Tracer Particle Motion

Tracer particles were initially positioned to outline the front and back surfaces of the target and the free surface of the rod. In addition, four rows of tracer particles were positioned in the target so that the deformation of the target could be recorded. Figure 27 shows the initial position of line segments which pass through the tracer particles and give a Lagrangian appearance to the computer solutions of the problems.

Figures 27 - 45 show a history of the rod-target deformation for the three radii being considered. Figure 46 shows the penetration-time relation for these radii. The depth of penetration is measured from the original front surface of the target. From incompressible jet penetration theory, the penetration rate is 3.87 km/s. At this rate, about 9.69 μ s would be required for the rod to pass through the 37.5-mm target. However, other phenomena such as a rarefaction wave from the back surface of the target would affect the perforation time. The computer output shows the penetration rate, based on 8 data points, to be 3.73, 3.64, and 3.60 km/s for R1X, R3X, and R9X, respectively, over the time period from 2 to 6 μ s. Although the 9-mm rod has the lowest velocity while it is penetrating the target, its velocity increases near the back surface of the target, and it is the first rod to reach the back surface.

Figures 27 - 45 were also used for measuring hole radii at the front and back surfaces of the target and four intermediate planes between these surfaces. These results are shown in Figure 47 where the hole radius has been nondimensionalized with respect to the radius of the rod. The distance, h , is measured from the front surface of the target into the target. Over the period that the problems were run, the hole radii did not reach a steady-state value for R3X and R9X; however, except for the rear portion of the hole, the R1X hole does attain a steady-state size. The rear hole size for R1X and R9X is shown to be larger than the front hole size.

C. Pressure and Particle Velocity

Pressure and material particle velocity profiles along the axis of symmetry of the rod-target configuration are shown in Figures 48 - 64. The rod-target interface on the axis of symmetry is indicated by a triangular symbol above the abscissa.

Using Tillotson's equation of state⁵ for copper and iron, we find that the rod-target interface is shocked to a pressure of 3.0 Mbar and that the particle velocity in this region is 3.92 km/s. These conditions would prevail in the interface region until the rarefaction wave from the free surface of the rod reaches the center-line of the rod. This occurs at 0.11, 0.34, and 1.02 μ s after impact for R1X, R3X, and R9X, respectively.

Since the computer print-out at $\frac{1}{4} \mu$ s occurs after the pressure in the rod was released by the rarefaction wave from the free surface of the rod, the peak pressure of 3.0 Mbar has already decayed for R1X; however, for R3X, the peak pressure is shown to exist in Figure 49, and, for R9X, in Figures 49 and 50.

In Figures 49 - 51, the steady-state particle velocity of 3.92 km/s exists for R9X; in Figure 49, this velocity is present for R3X.

Figure 51 shows that although the interface (triangular symbol) is at approximately the same position on the z axis, for all cases the position of the shock front from the interface is greatest for R9X and decreases as the rod radius becomes smaller.

Figure 65 shows the pressure histories for the three cases over a period of 10 or 11 μ s. For all cases, the pressure histories are dissimilar. For R1X, a constant pressure peak of 0.43 Mbar exists from time 2 μ s to 8 μ s. Over this same time period, a constant pressure peak of 0.65 Mbar exists for R3X. For R9X, the peak pressure continuously decays after $\frac{1}{2} \mu$ s.

VII. DISCUSSION

The DORF-9 code was used to make a parametric study of the impact of a long, slender, high speed copper rod on a steel target mainly to obtain hole growth information. The rod radius was varied (1, 3, and 9 mm) and the target thickness was varied (7.5 and 37.5 mm). The impact velocity remained constant at 7.5 km/s for all cases.

Hole growth information was obtained from tracer particle graphs showing the rod-target deformation. Although the computer runs were not long enough to obtain the final hole profiles, information on the rate of hole growth can be extracted from the data presented. The hole data indicates that, for both the thin and thick targets, the rear radius of the hole was larger than the front radius.

The penetration histories for the case of the thin target did not indicate a relation between the rod radius and penetration velocity; however, for the thick target, the penetration velocity increased with rod radius. For both target thicknesses, the velocity of the rod-target interface increased when the interface approached the back

face of the target with the 9-mm radius rod passing the back face first.

The velocity and pressure profiles along the axis of symmetry indicate dissimilarities between all the cases that were run. For the thin target case, steady-state pressure or particle velocity profiles were never attained. For the thick target case, constant peak pressures were attained for the 1 and 3-mm radius rod over a period during penetration; however, for the 9-mm radius rod, the peak pressure continued to decay once the rarefaction wave from the rod's free surface acted on the rod-target shock wave.

ACKNOWLEDGEMENTS

The author would like to acknowledge Allen Delp, Neil Wolfe, and Vincent Marchesand for their computer and graphical support.

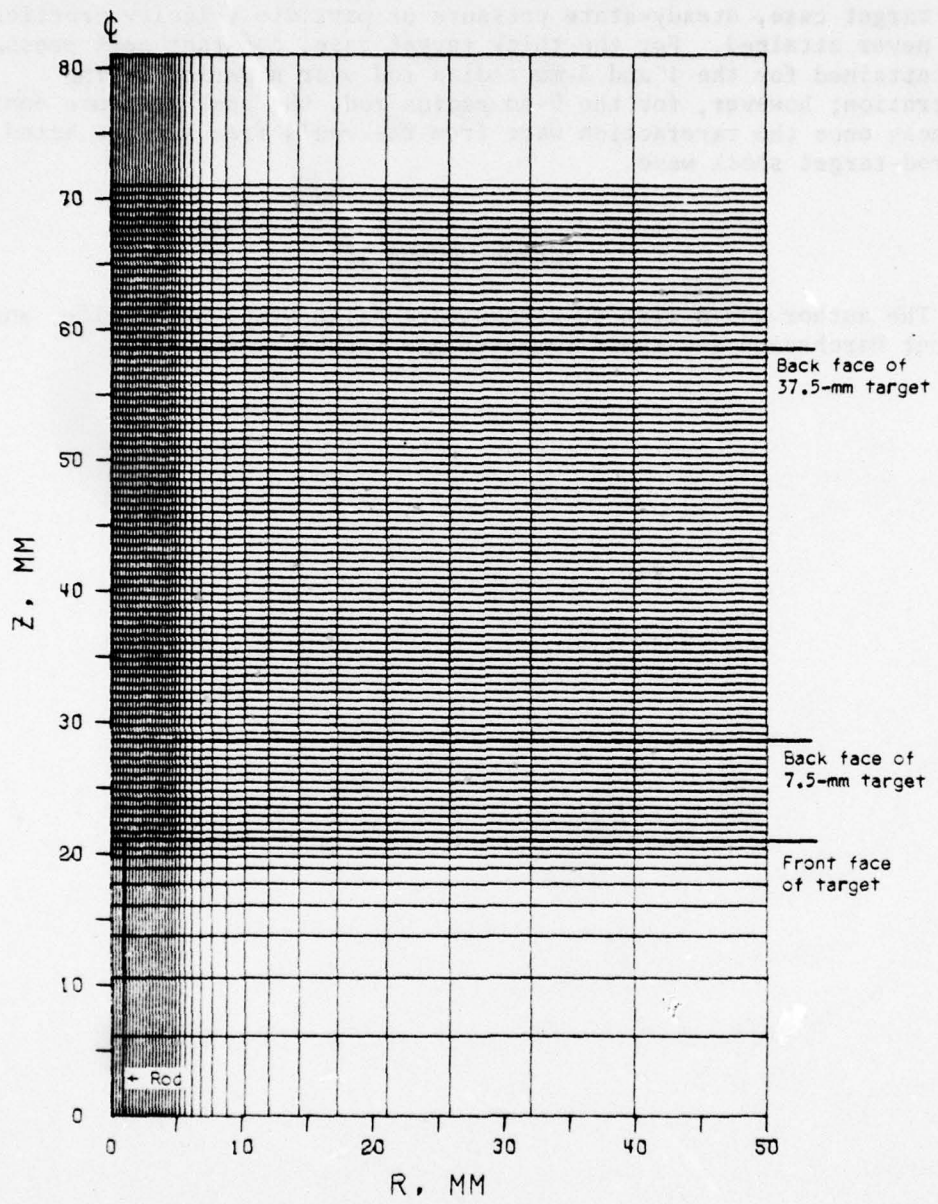


Figure 1. Grid Configuration for a 1-mm Radius Rod

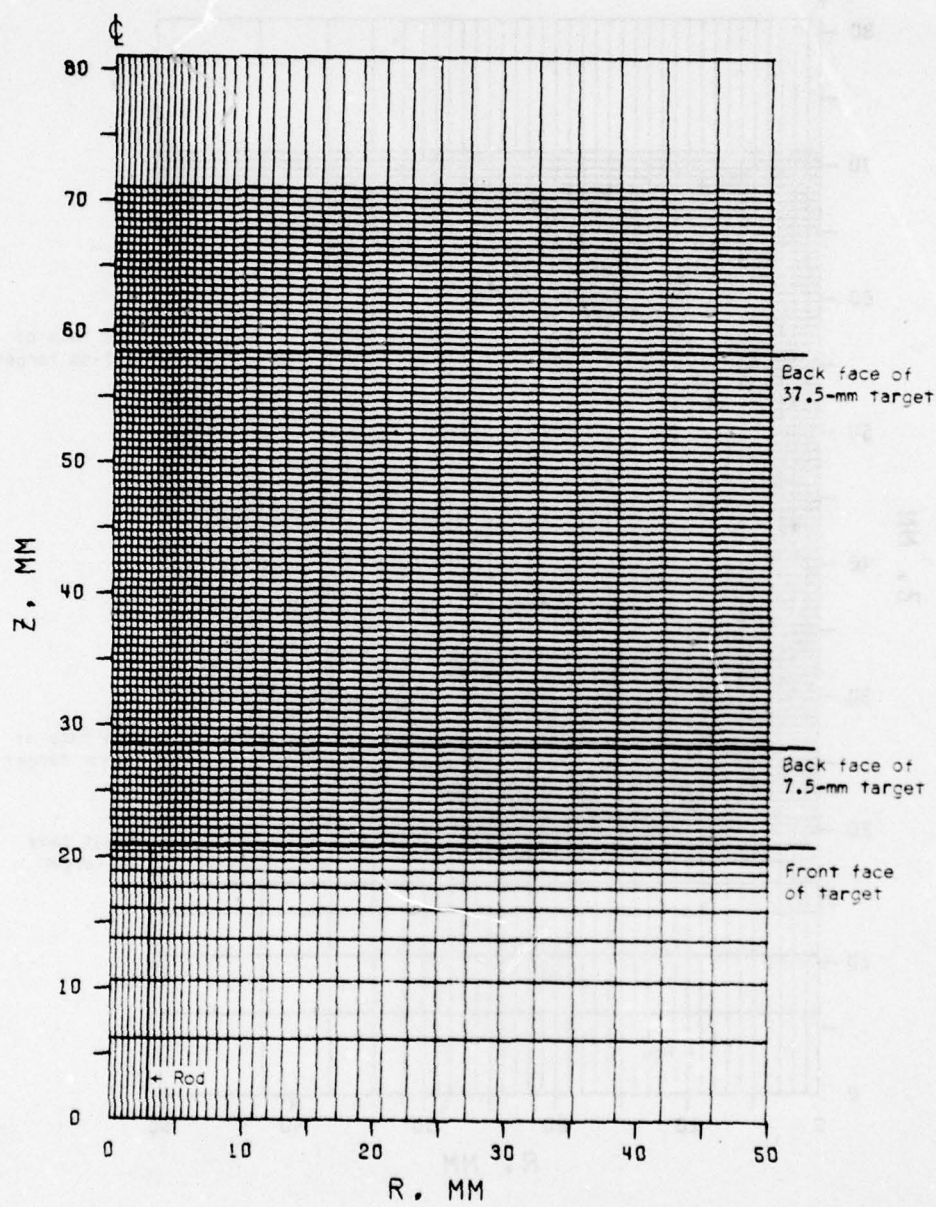


Figure 2. Grid-Configuration for a 3-mm Radius Rod

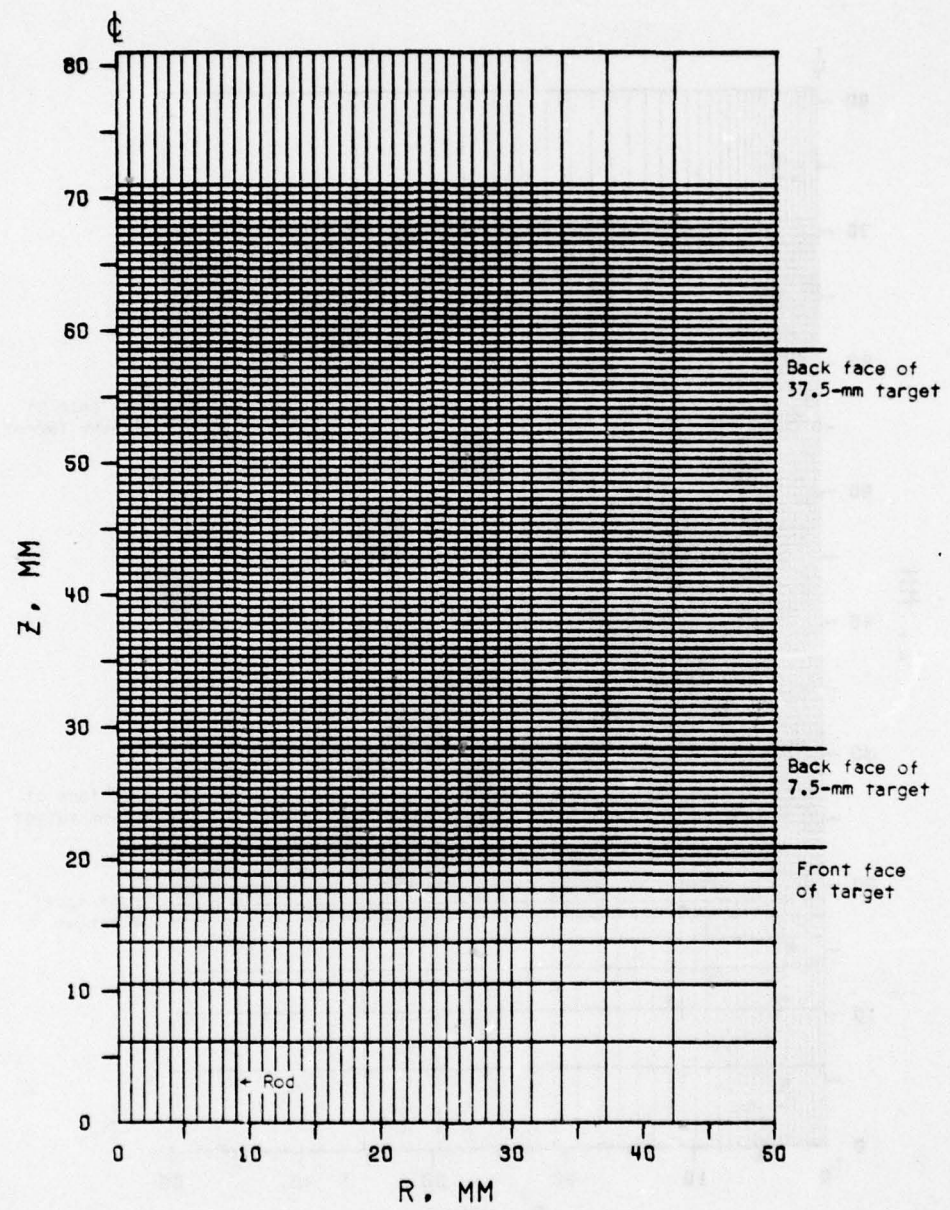


Figure 3. Grid Configuration for a 9-mm Radius Rod

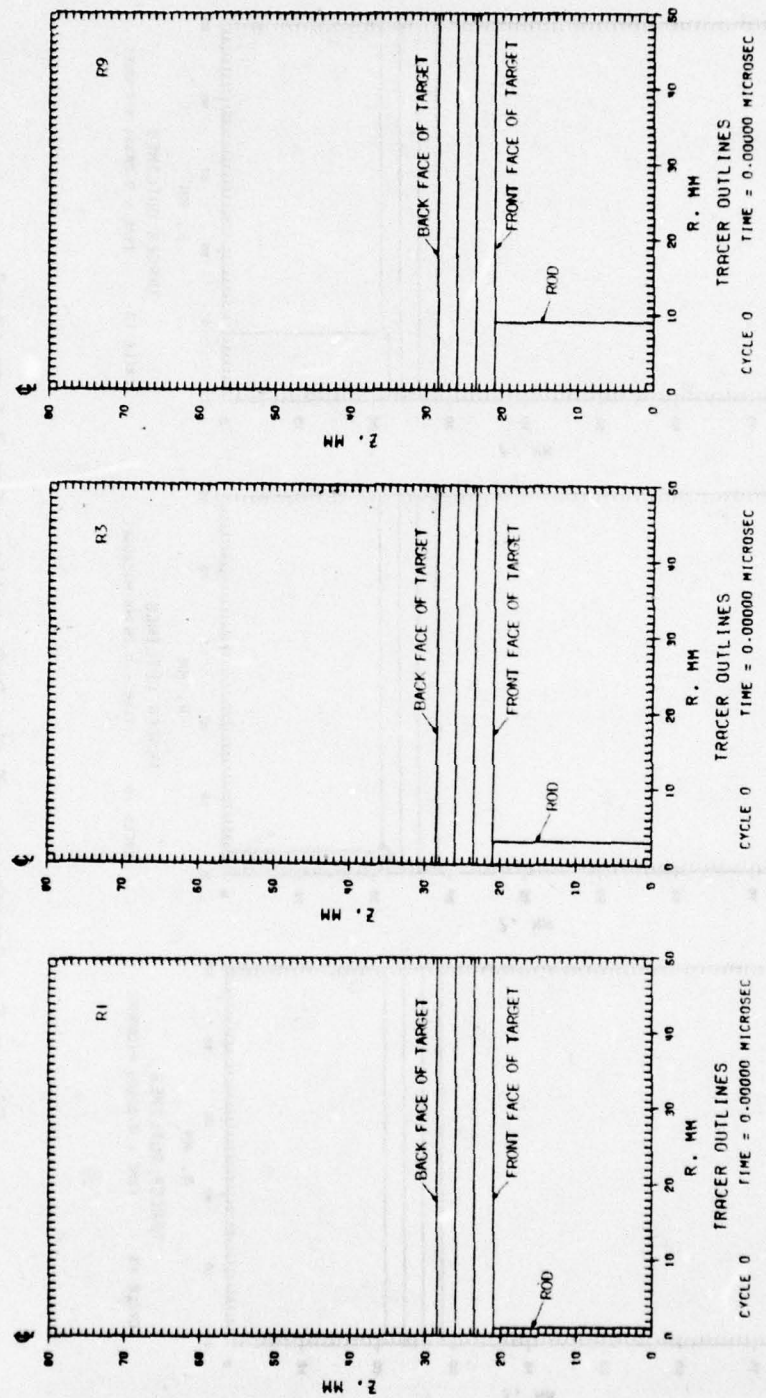


Figure 4. Comparison of the Deformation of a 7.5-mm Steel Target Impacted by 1, 3, and 9-mm Copper Rods

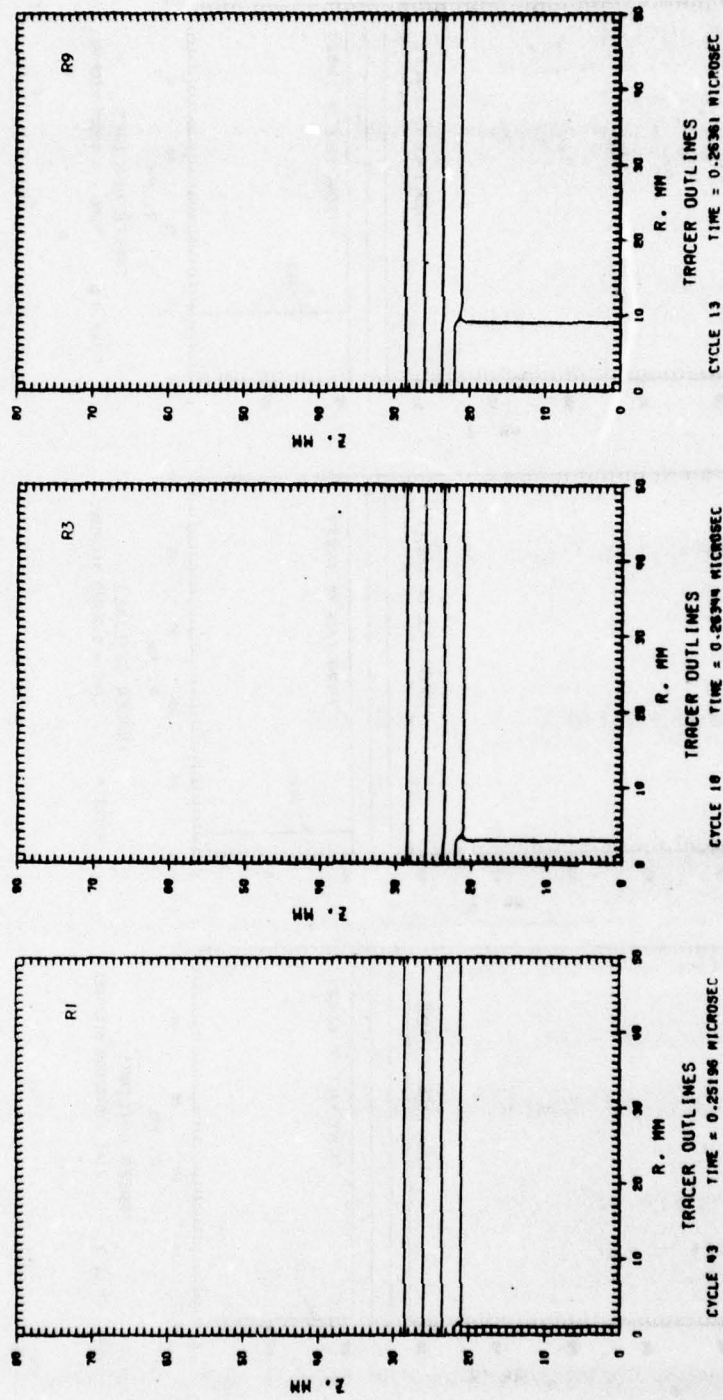


Figure 5. Comparison of the Deformation of a 7.5-mm Steel Target Impacted by 1, 3, and 9-mm Copper Rods

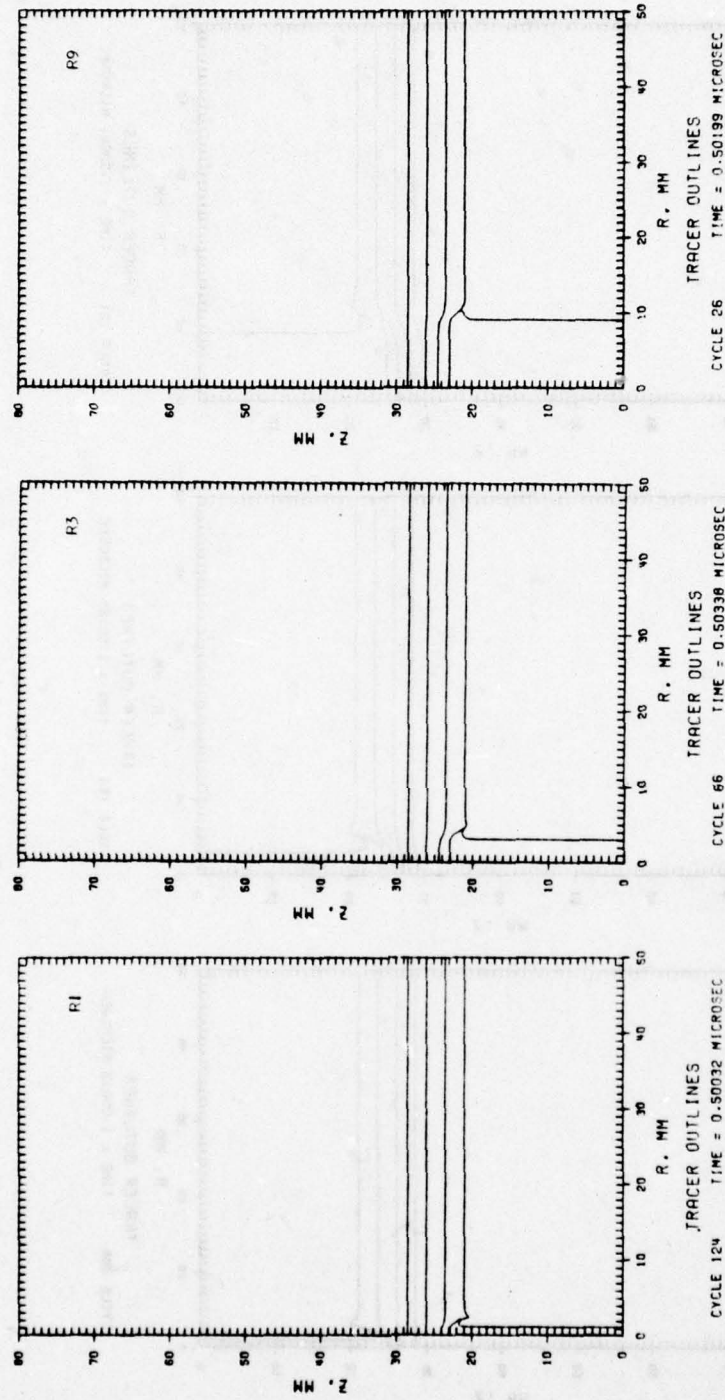


Figure 6. Comparison of the Deformation of a 7.5-mm Steel Target Impacted by 1, 3, and 9-mm Copper Rods

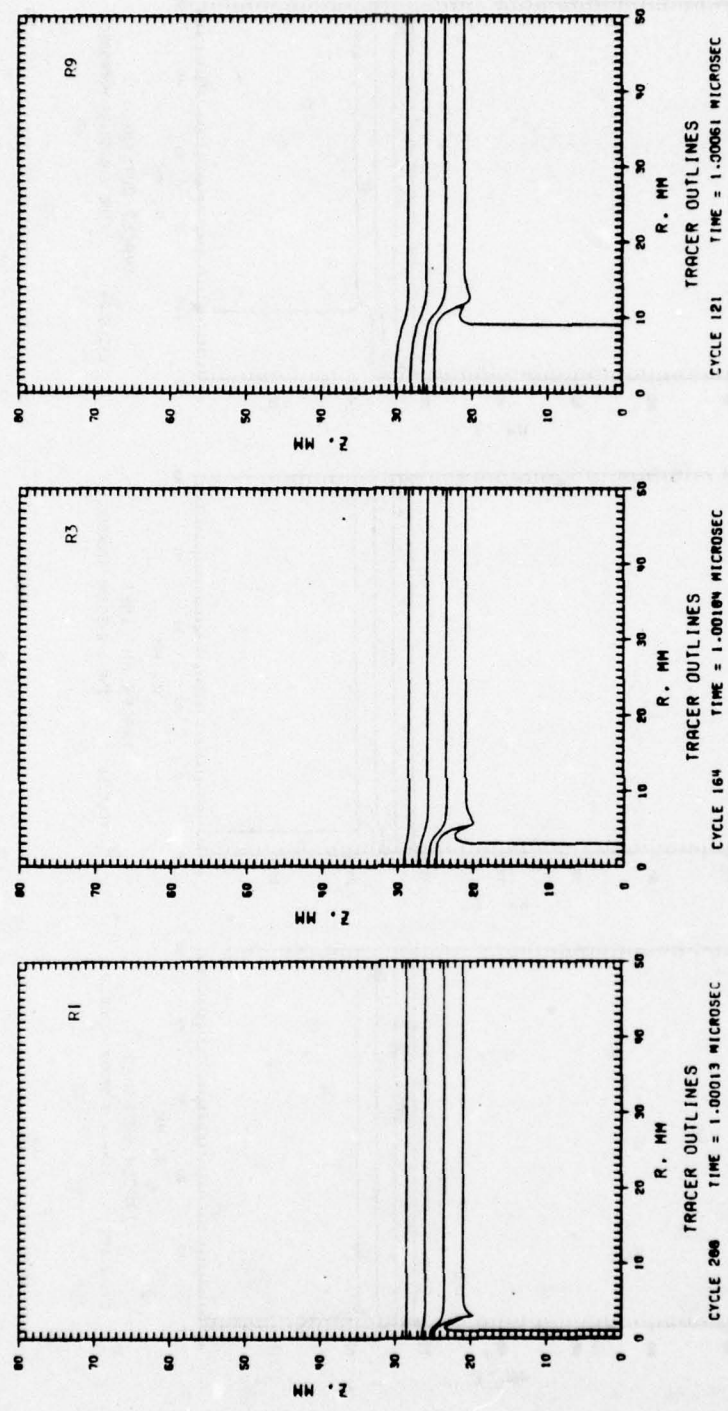


Figure 7. Comparison of the Deformation of a 7.5-mm Steel Target Impacted by 1, 3, and 9-mm Copper Rods

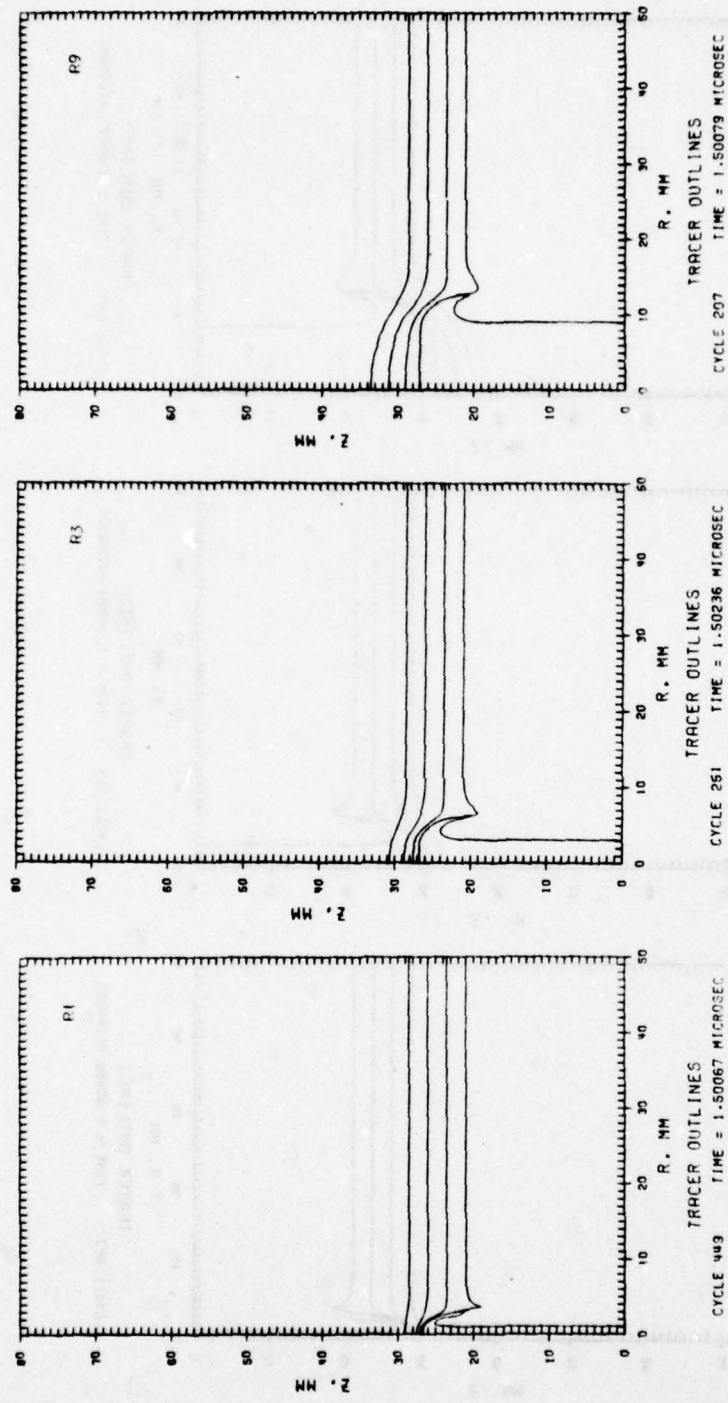


Figure 8. Comparison of the Deformation of a 7.5-mm Steel Target Impacted by 1, 3, and 9-mm Copper Rods

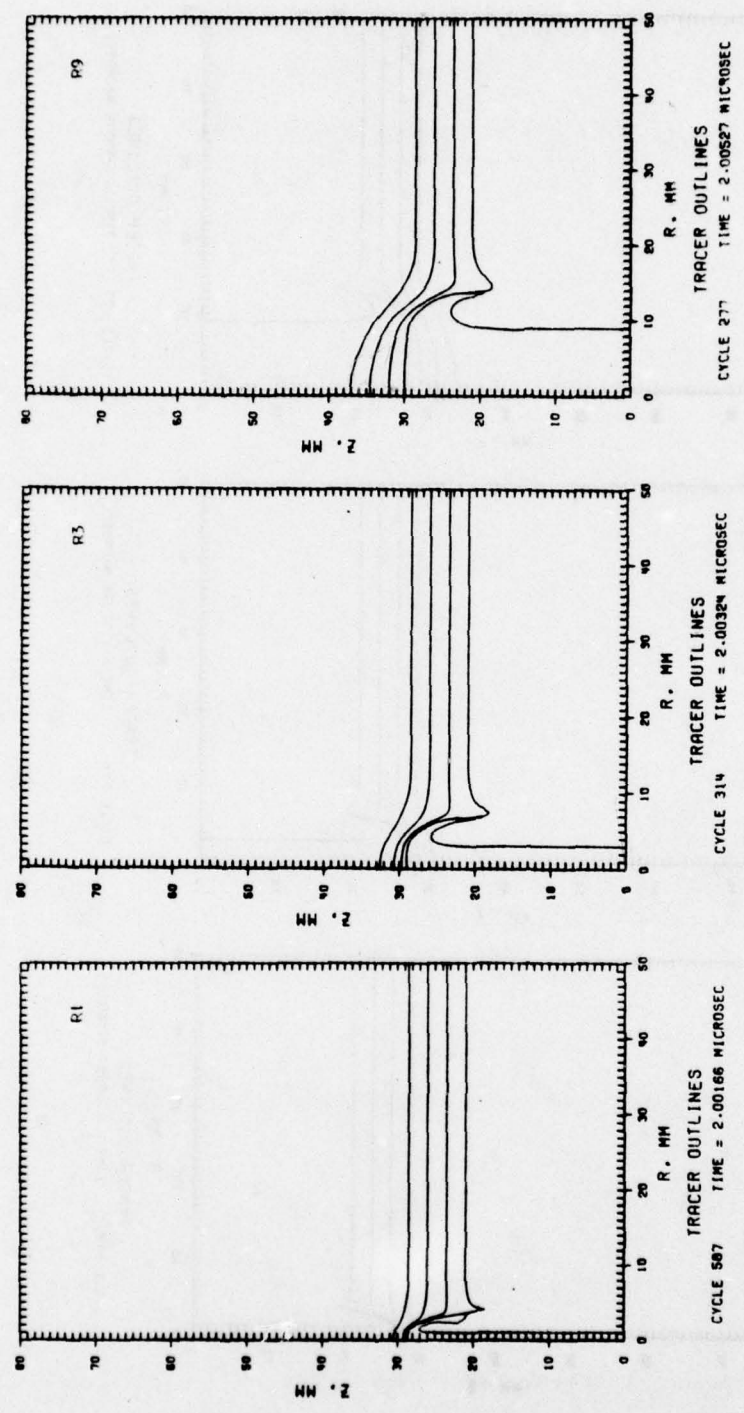


Figure 9. Comparison of the Deformation of a 7.5-mm Steel Target Impacted by 1, 3, and 9-mm Copper Rods

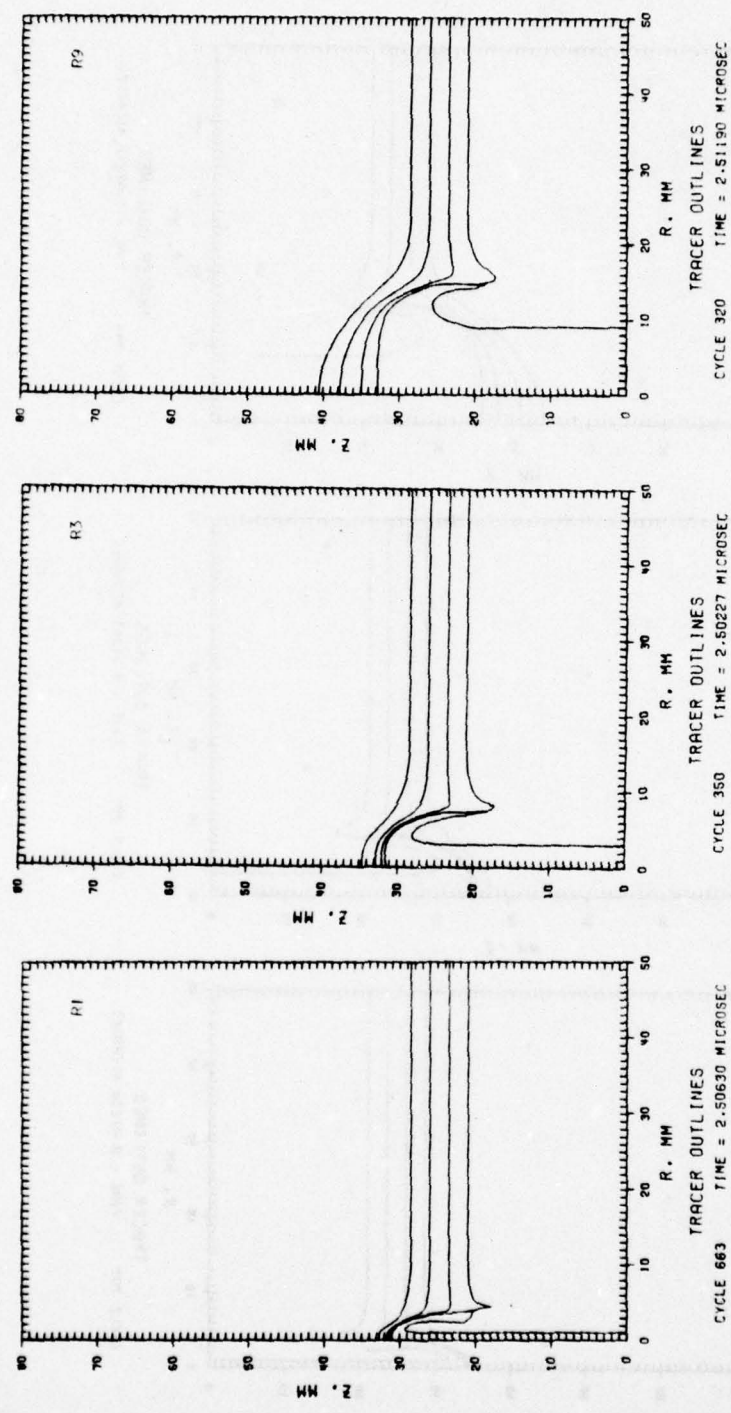


Figure 10. Comparison of the Deformation of a 7.5-mm Steel Target Impacted by 1, 3, and 9-mm Copper Rods

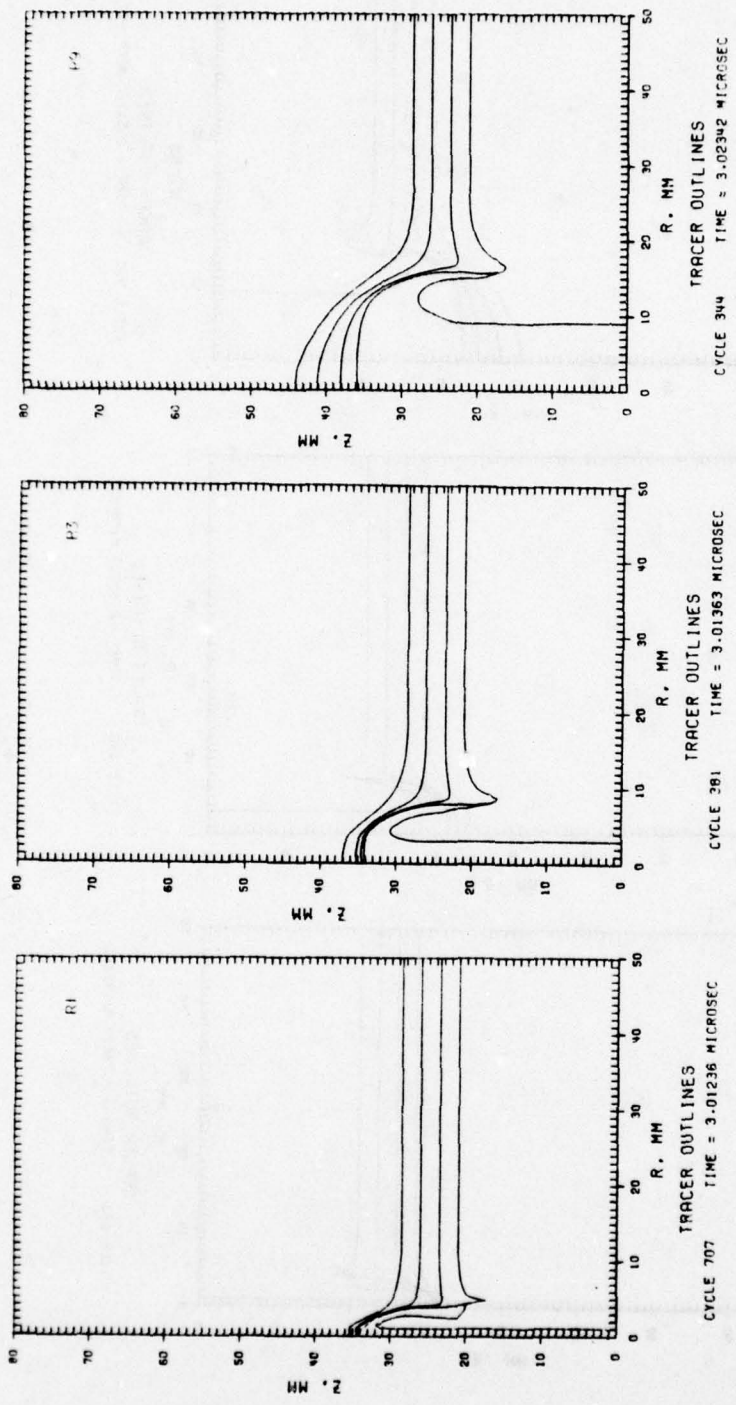


Figure 11. Comparison of the Deformation of a 7.5-mm Steel Target Impacted by 1, 3, and 9-mm Copper Rods

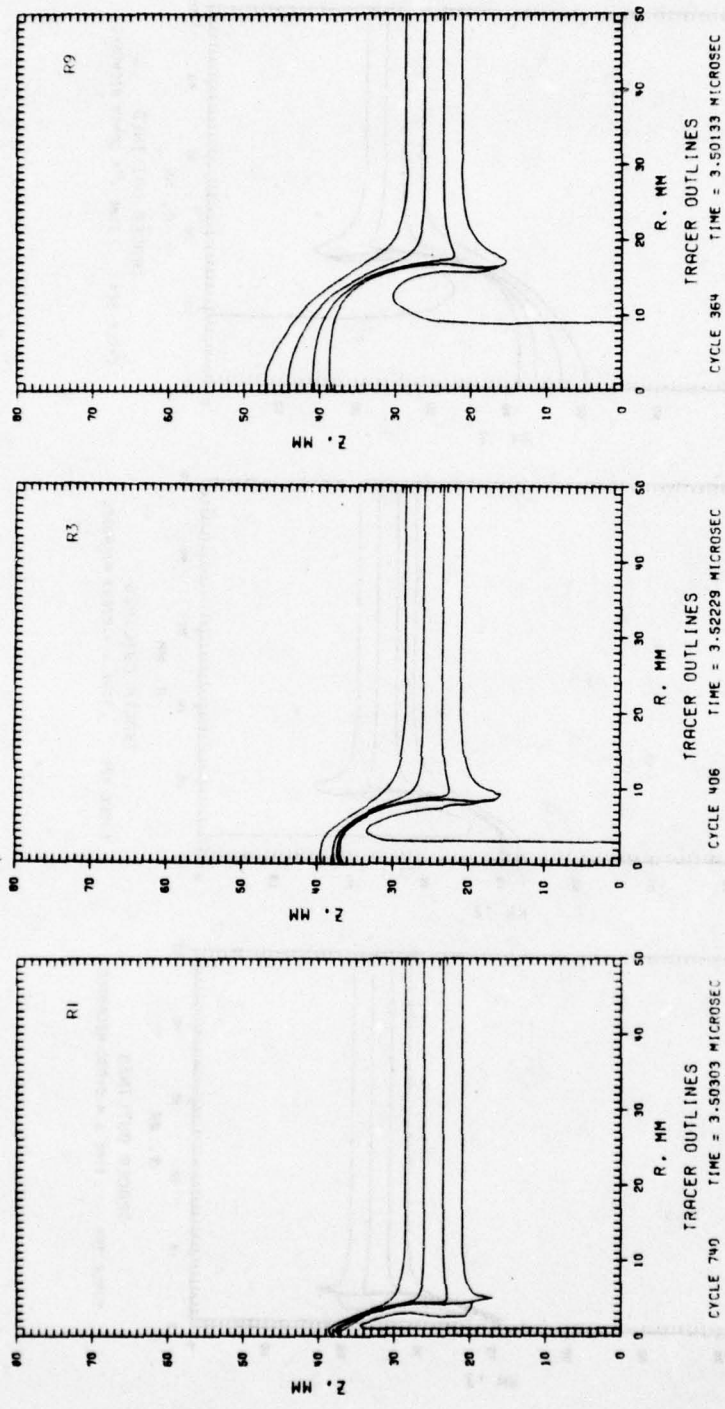


Figure 12. Comparison of the Deformation of a 7.5-mm Steel Target Impacted by 1, 3, and 9-mm Copper Rods

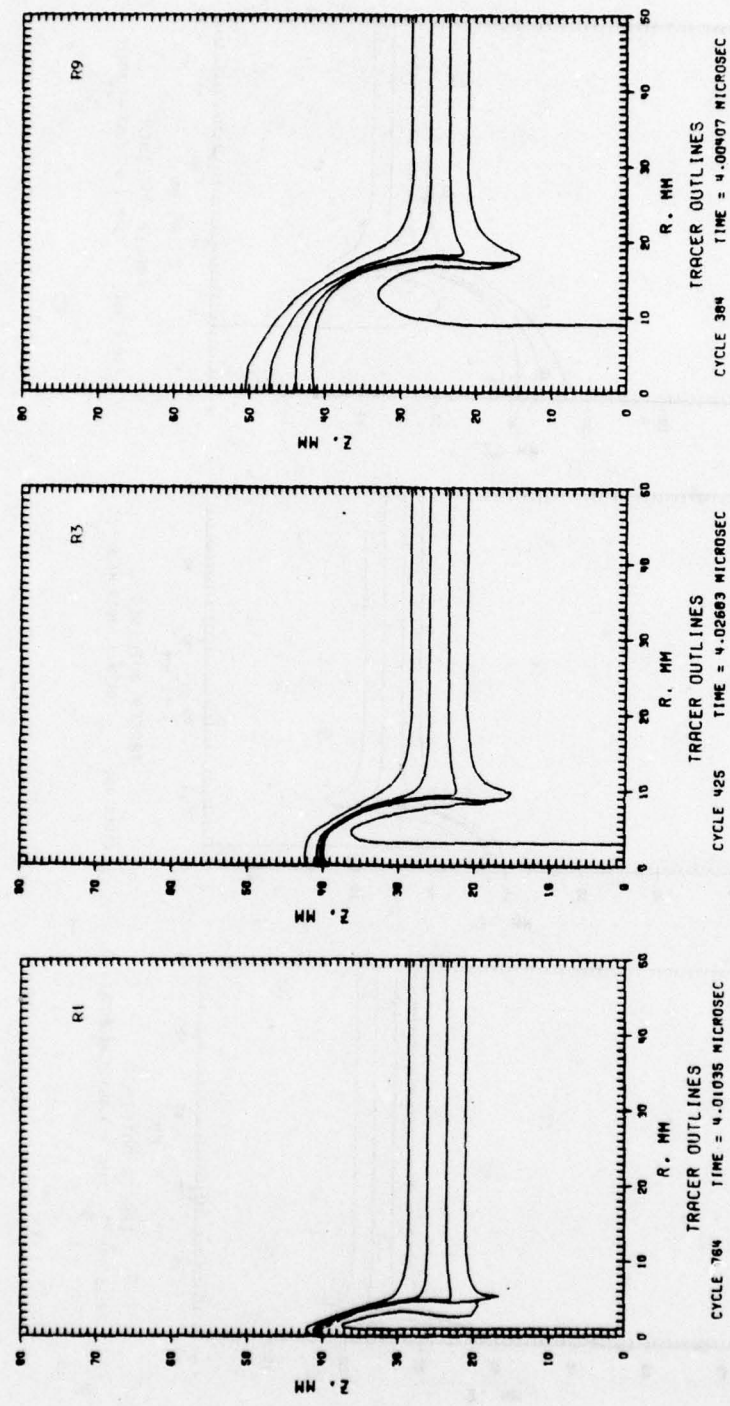


Figure 13. Comparison of the Deformation of a 7.5-mm Steel Target Impacted by 1, 3, and 9-mm Copper Rods

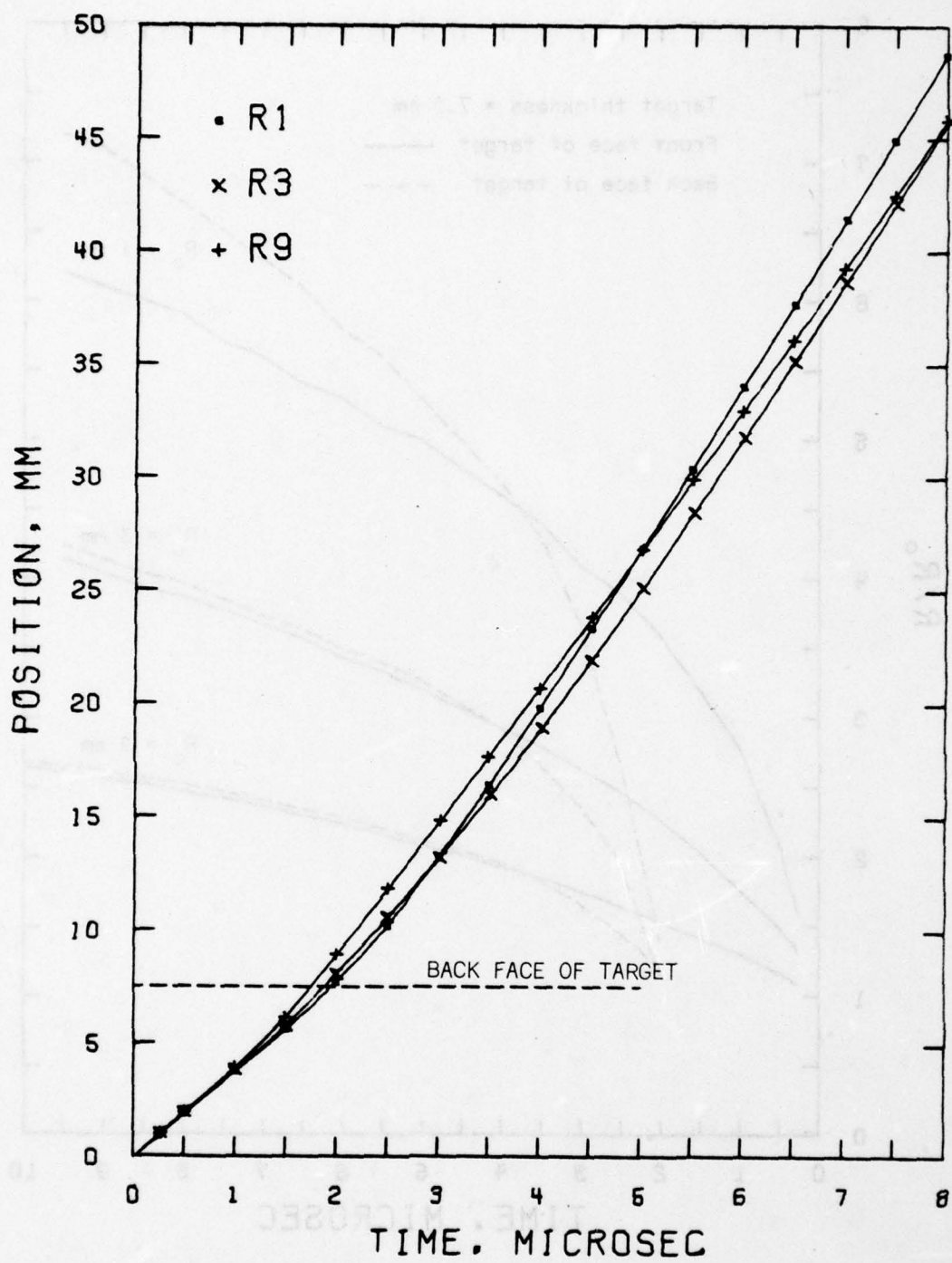


Figure 14. Position of the Rod-Target Interface on the Axis of Symmetry Versus Time

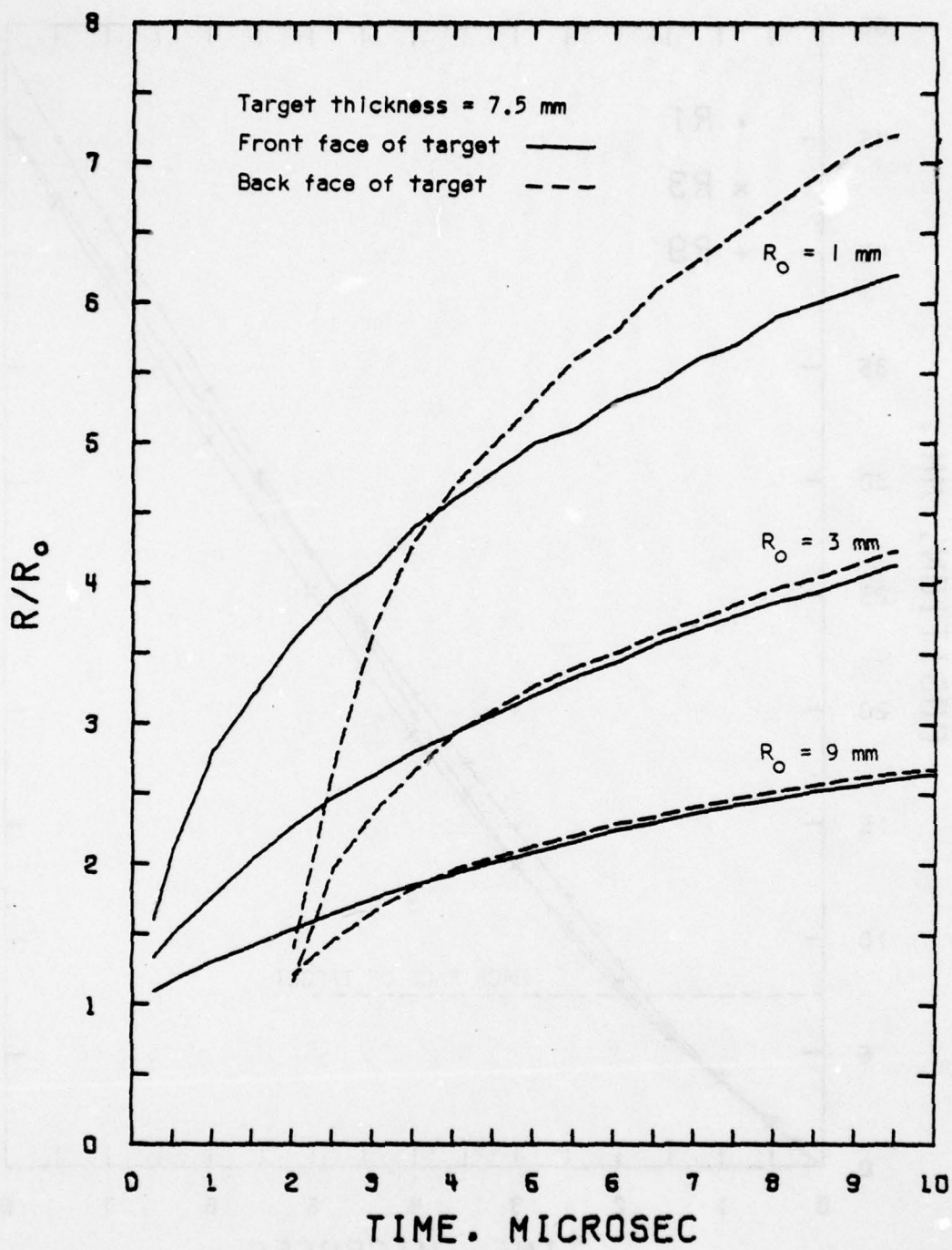


Figure 15. Comparison of Hole Growth

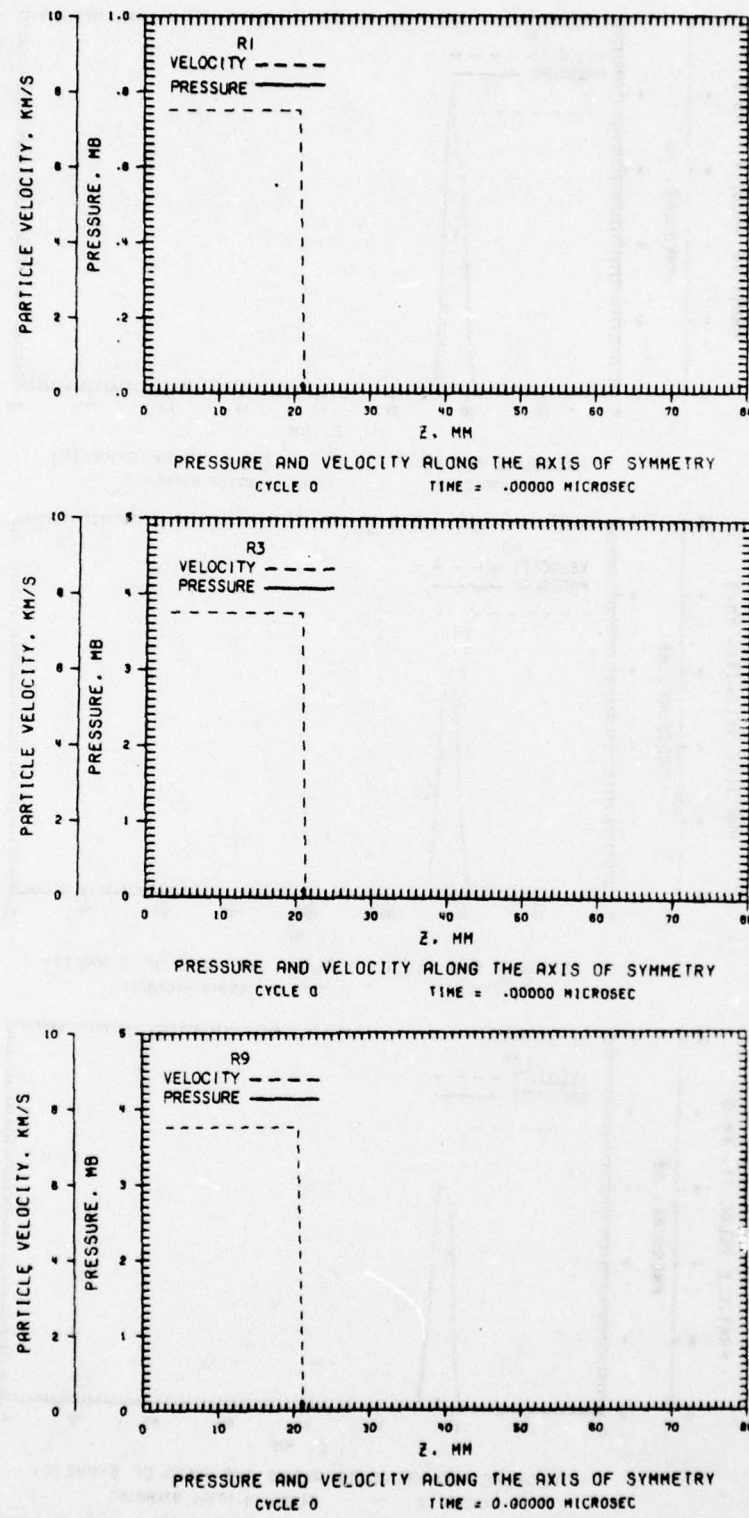


Figure 16. Comparison of Pressure and Velocity Profiles

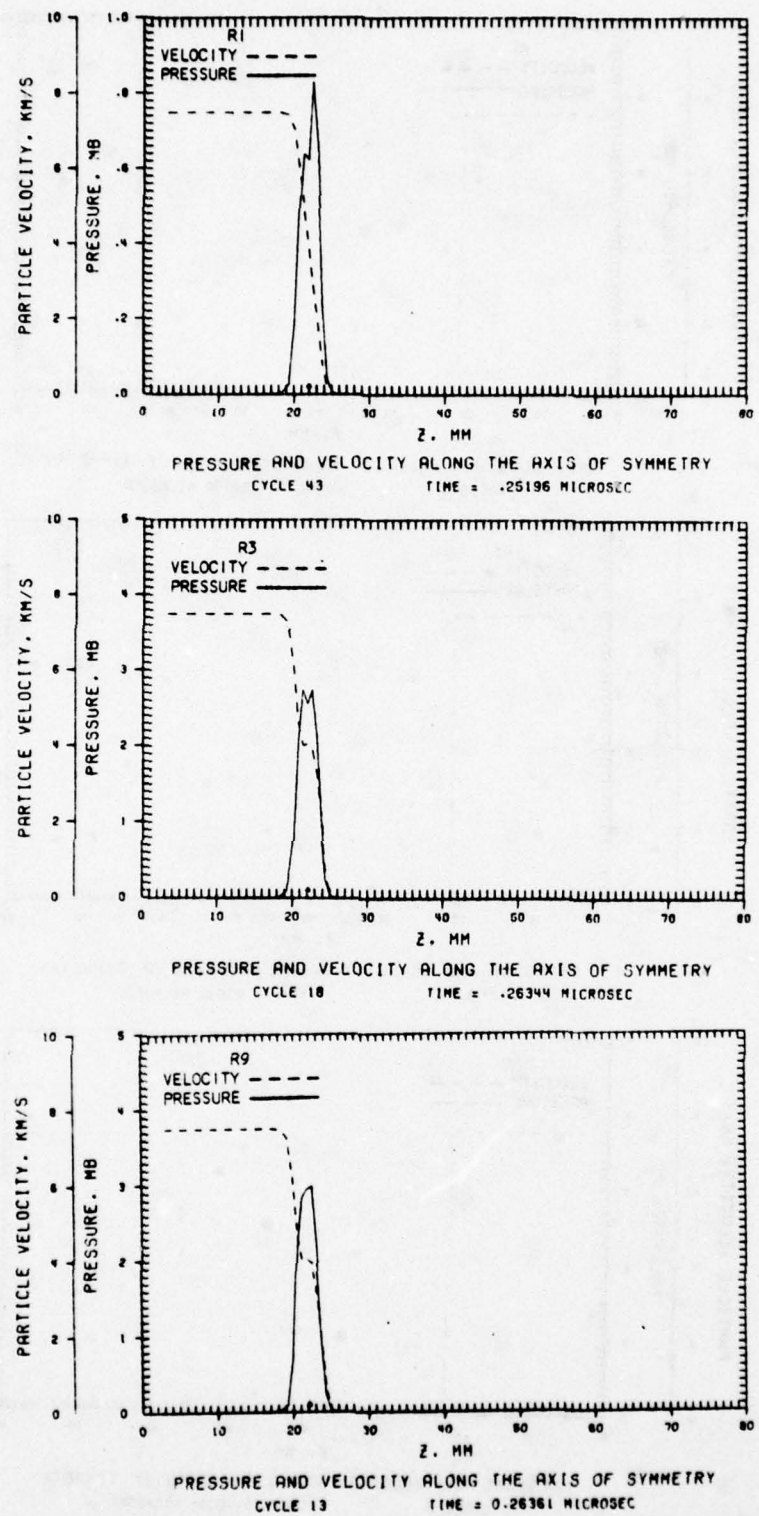


Figure 17. Comparison of Pressure and Velocity Profiles

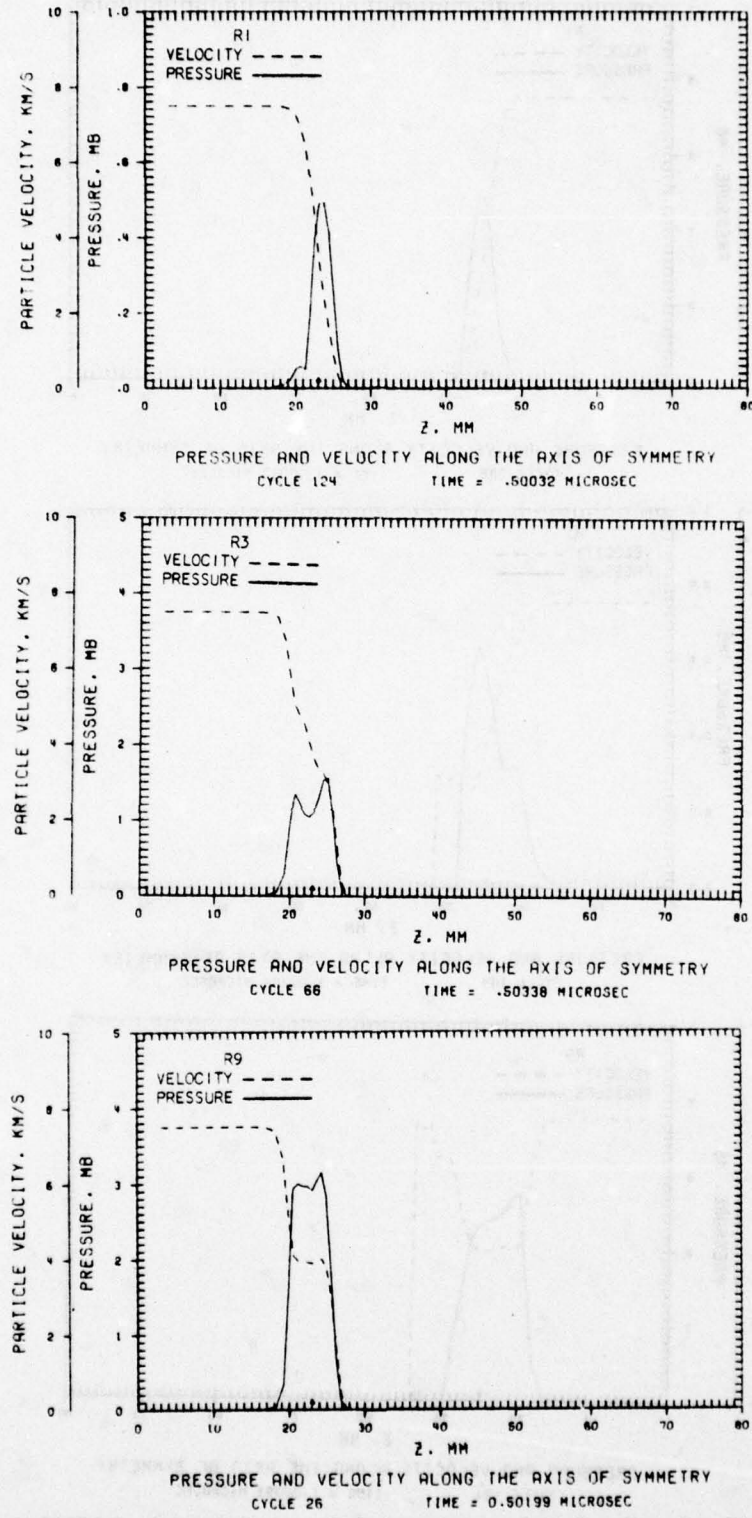


Figure 18. Comparison of Pressure and Velocity Profiles

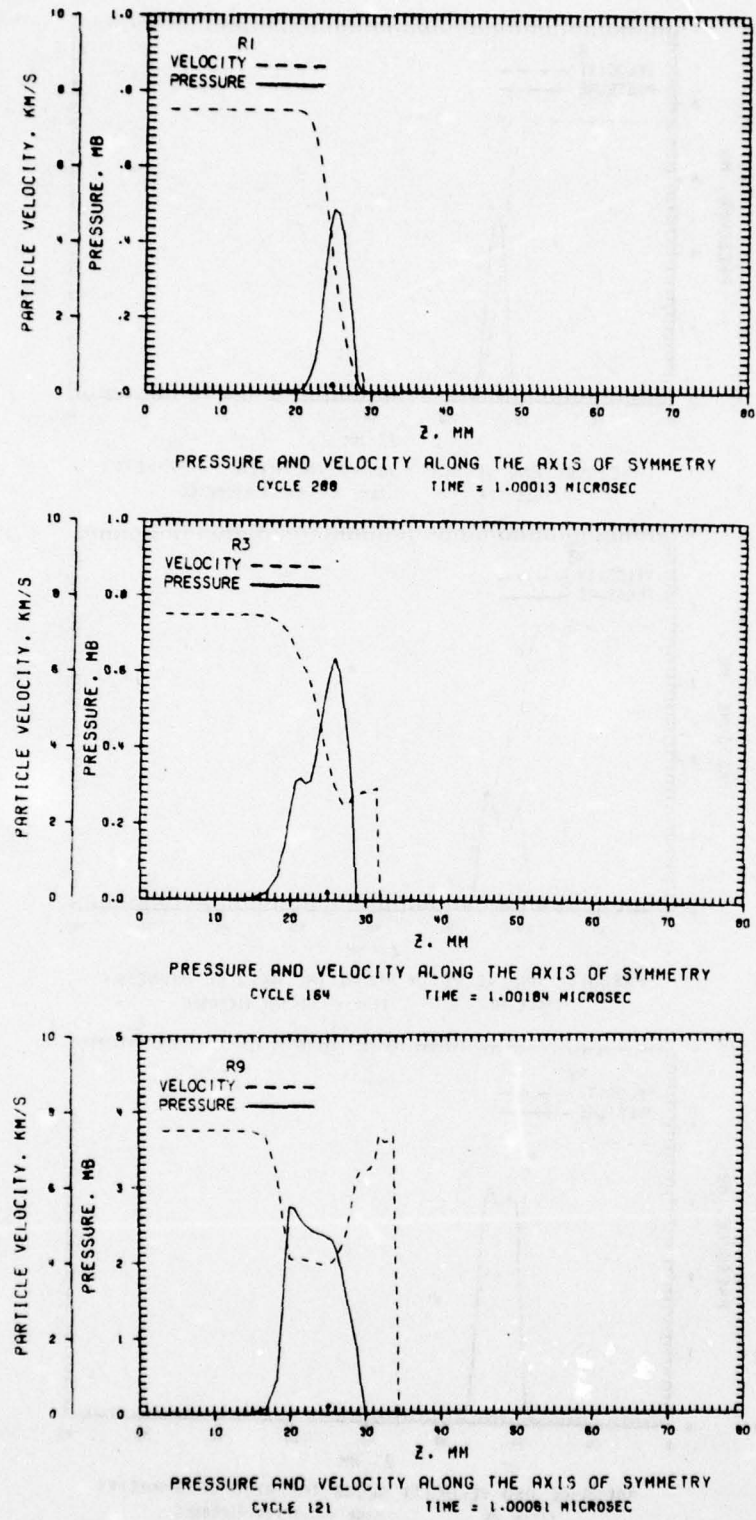


Figure 19. Comparison of Pressure and Velocity Profiles

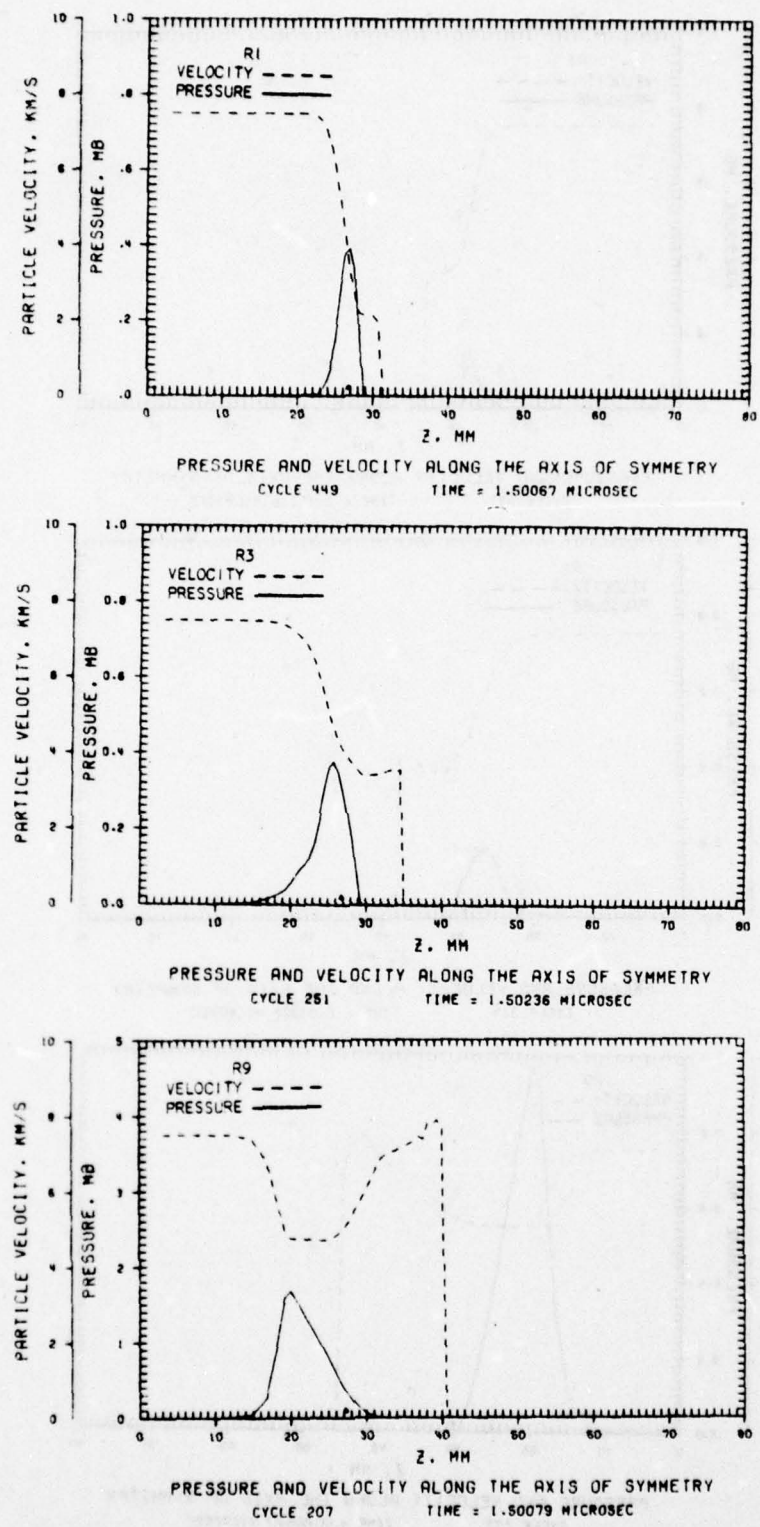


Figure 20. Comparison of Pressure and Velocity Profiles

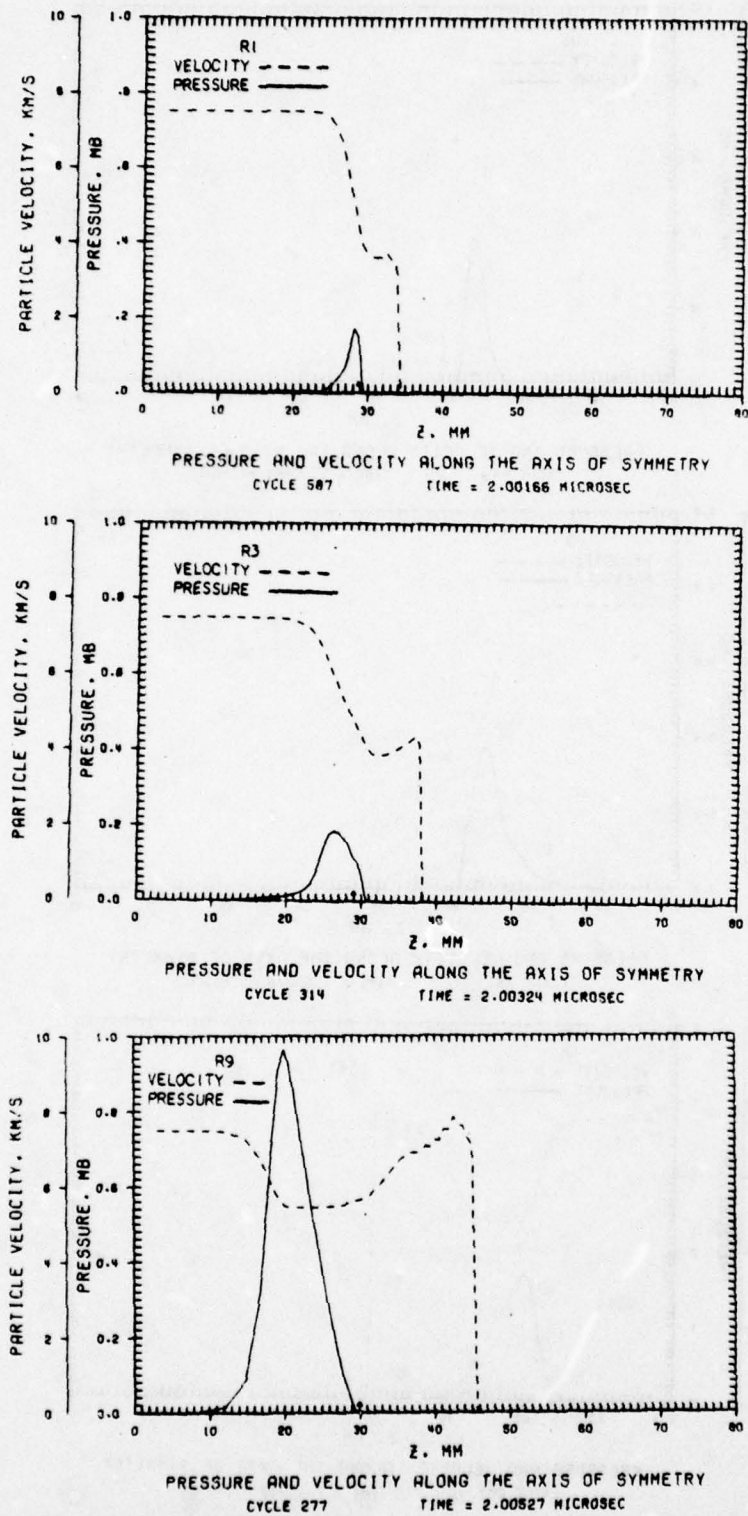


Figure 21. Comparison of Pressure and Velocity Profiles

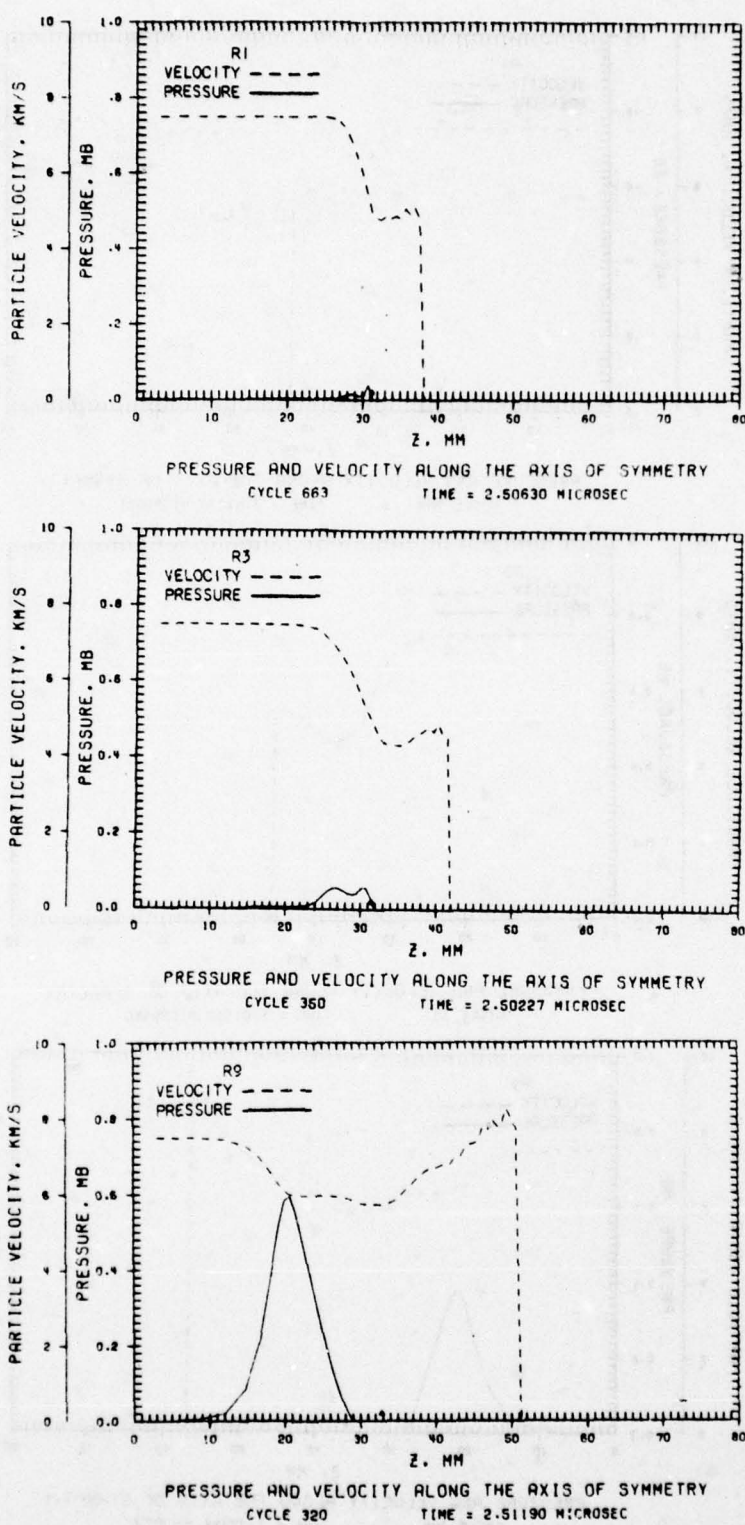


Figure 22. Comparison of Pressure and Velocity Profiles

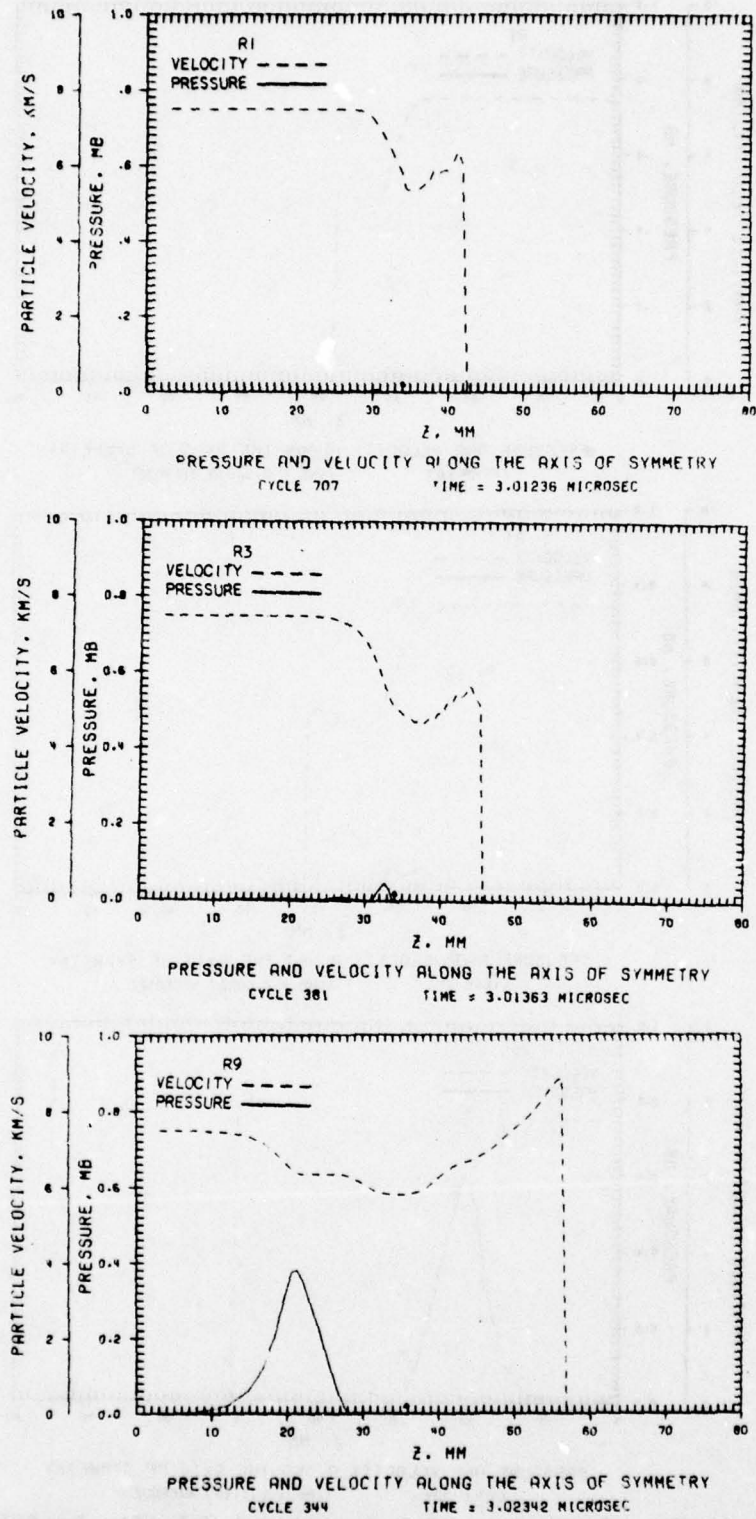


Figure 23. Comparison of Pressure and Velocity Profiles

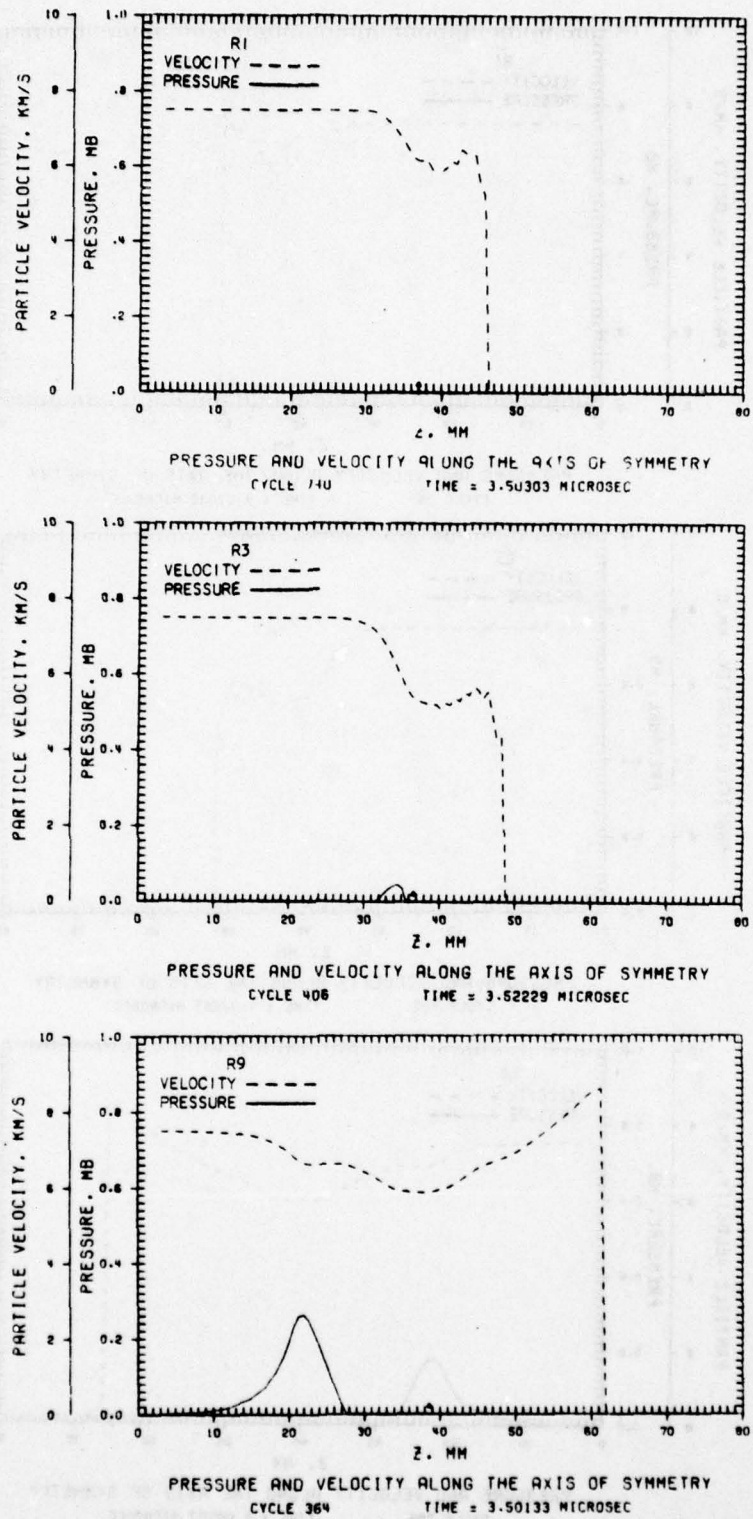


Figure 24. Comparison of Pressure and Velocity Profiles

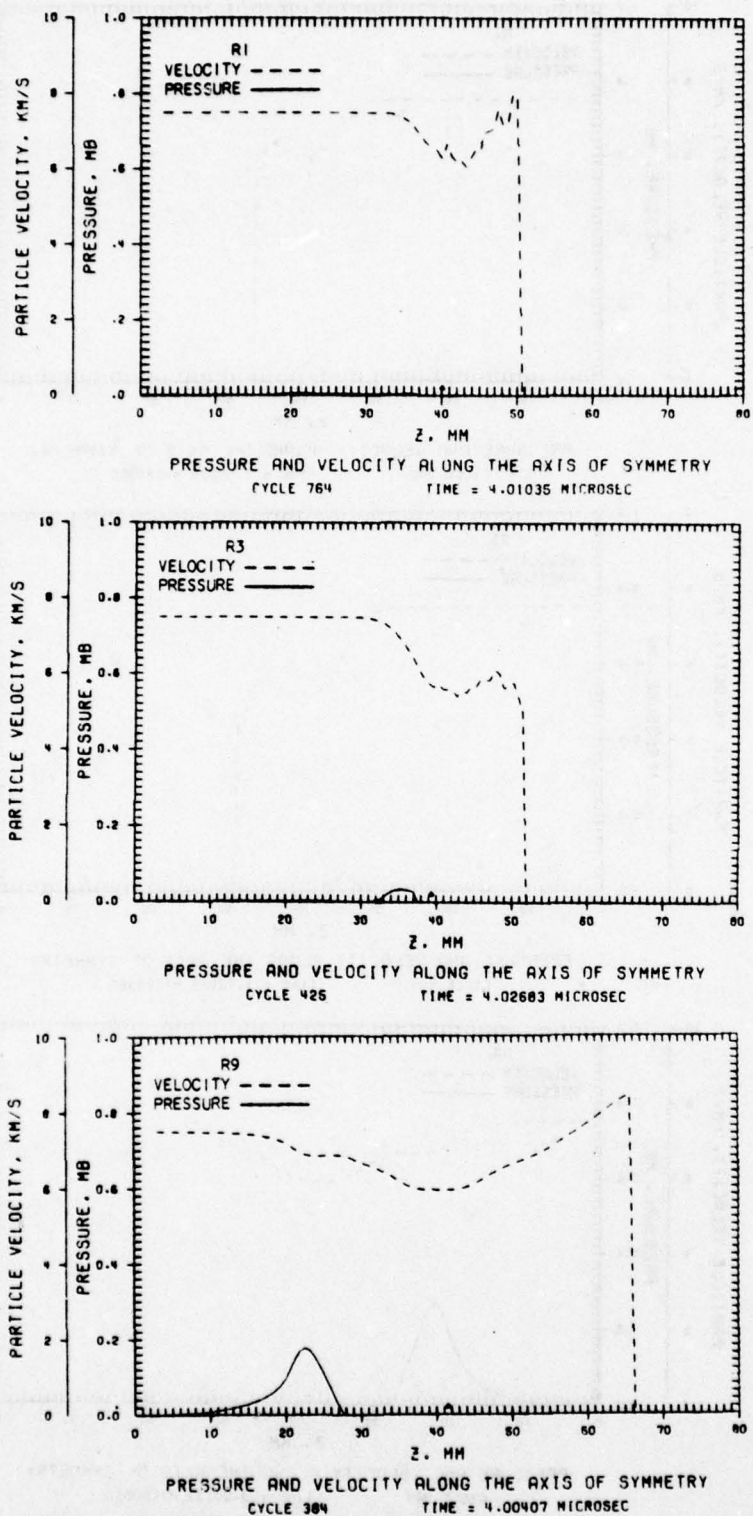


Figure 25. Comparison of Pressure and Velocity Profiles

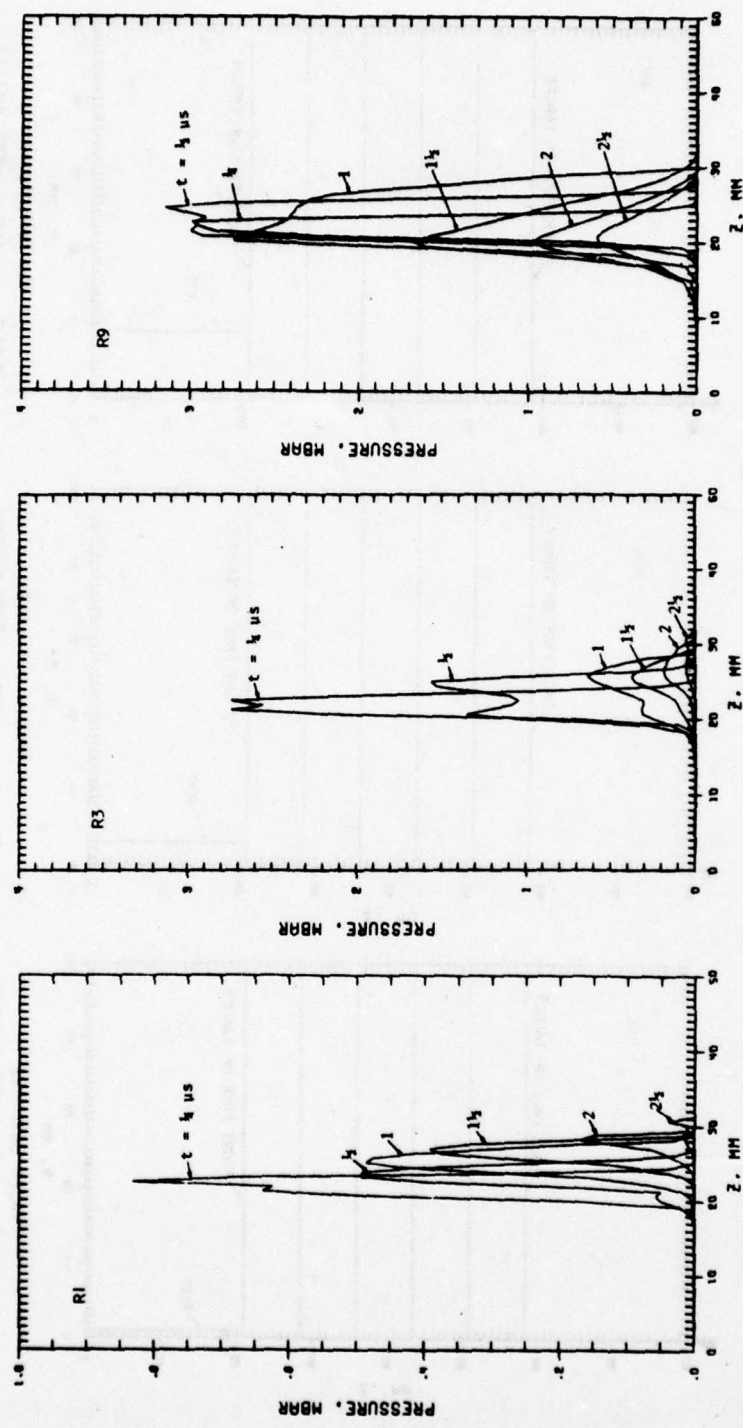


Figure 26. Comparison of Pressure Profiles along the Axis of Symmetry

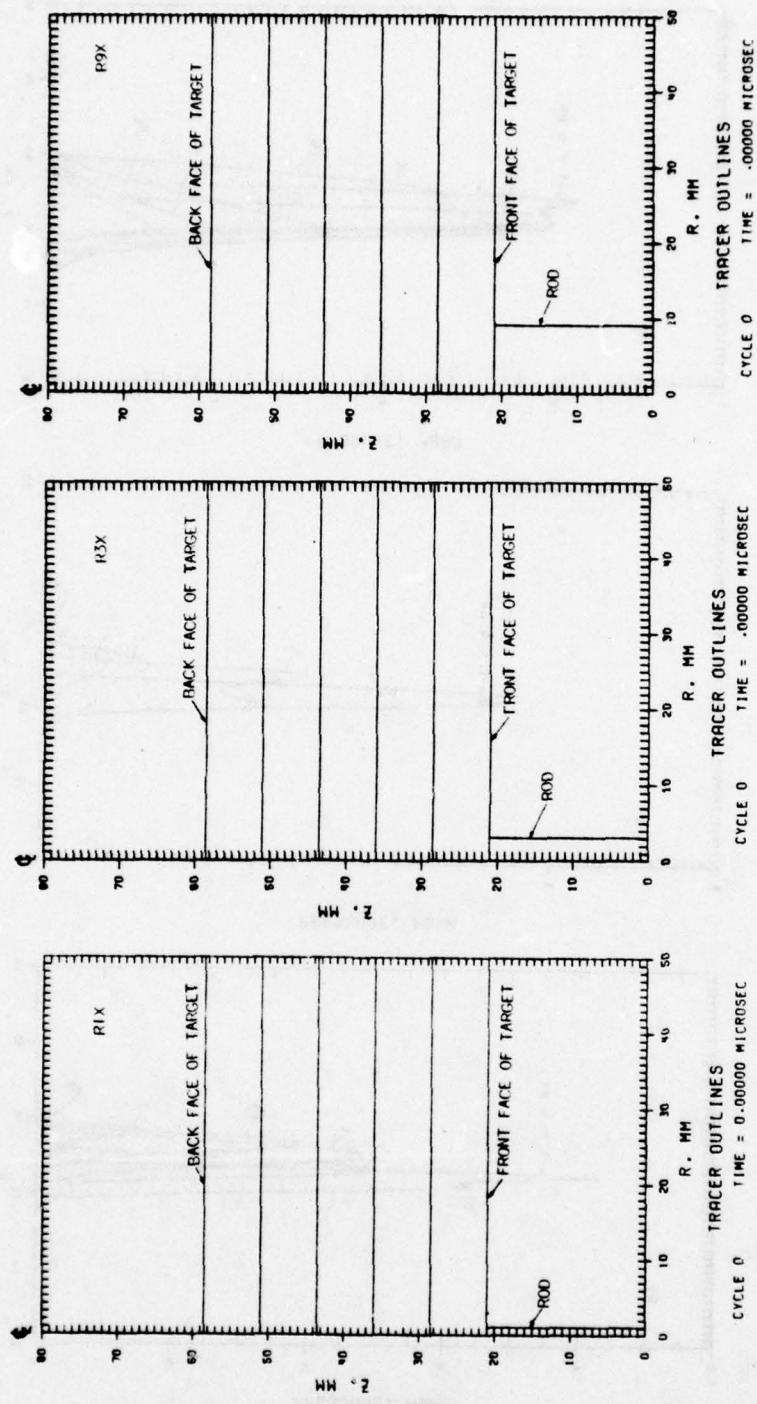


Figure 27. Comparison of the Deformation of a 37.5-mm Steel Target Impacted by 1, 3, and 9-mm Copper Rods

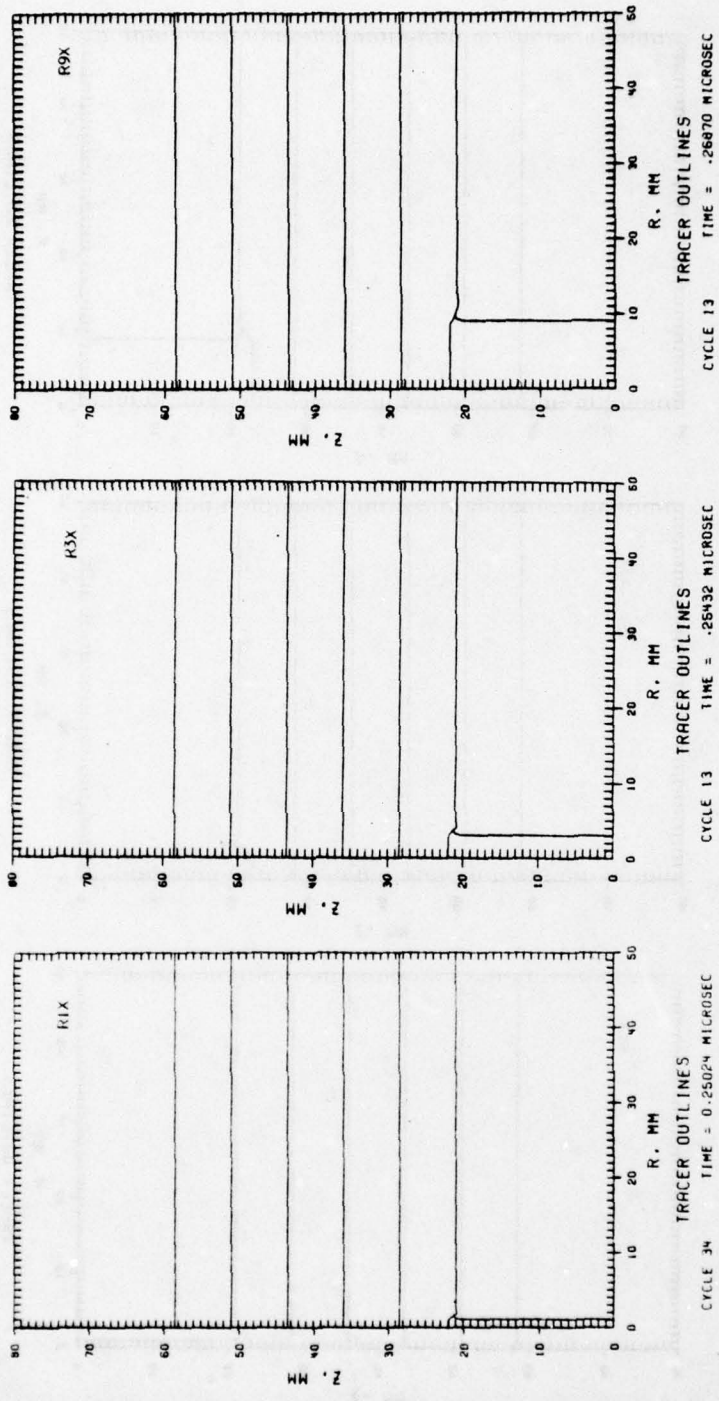


Figure 28. Comparison of the Deformation of a 37.5-mm Steel Target Impacted by 1, 3, and 9-mm Copper Rods

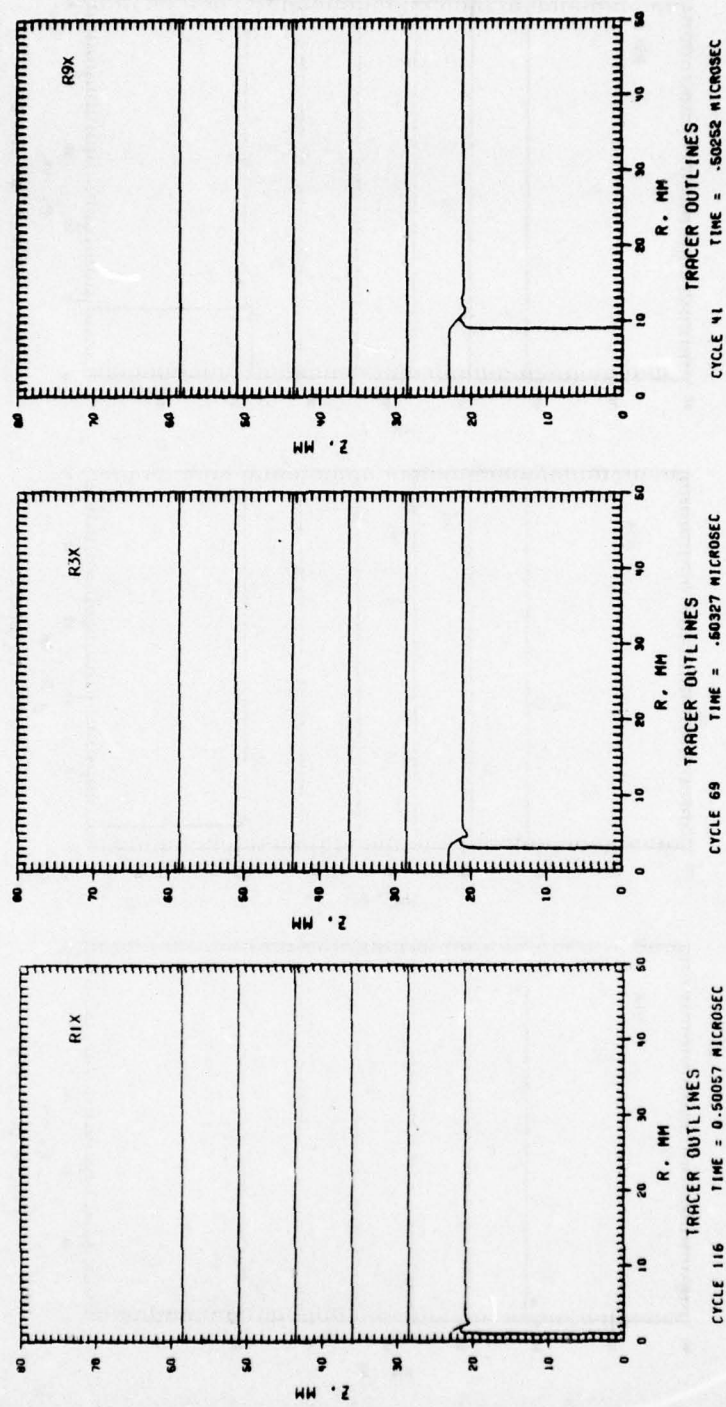


Figure 29. Comparison of the Deformation of a 37.5-mm Steel Target Impacted by 1, 3, and 9-mm Copper Rods

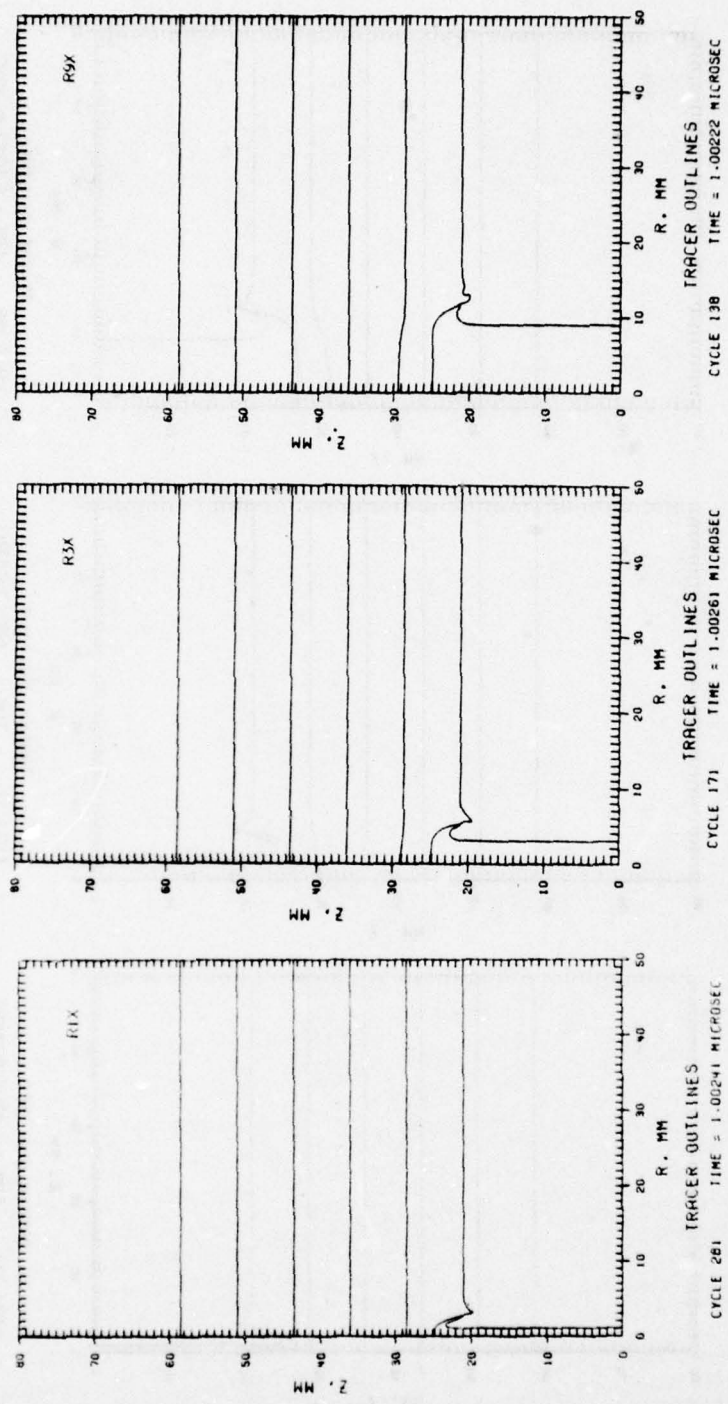


Figure 30. Comparison of the Deformation of a 37.5-mm Steel Target Impacted by 1, 3, and 9-mm Copper Rods

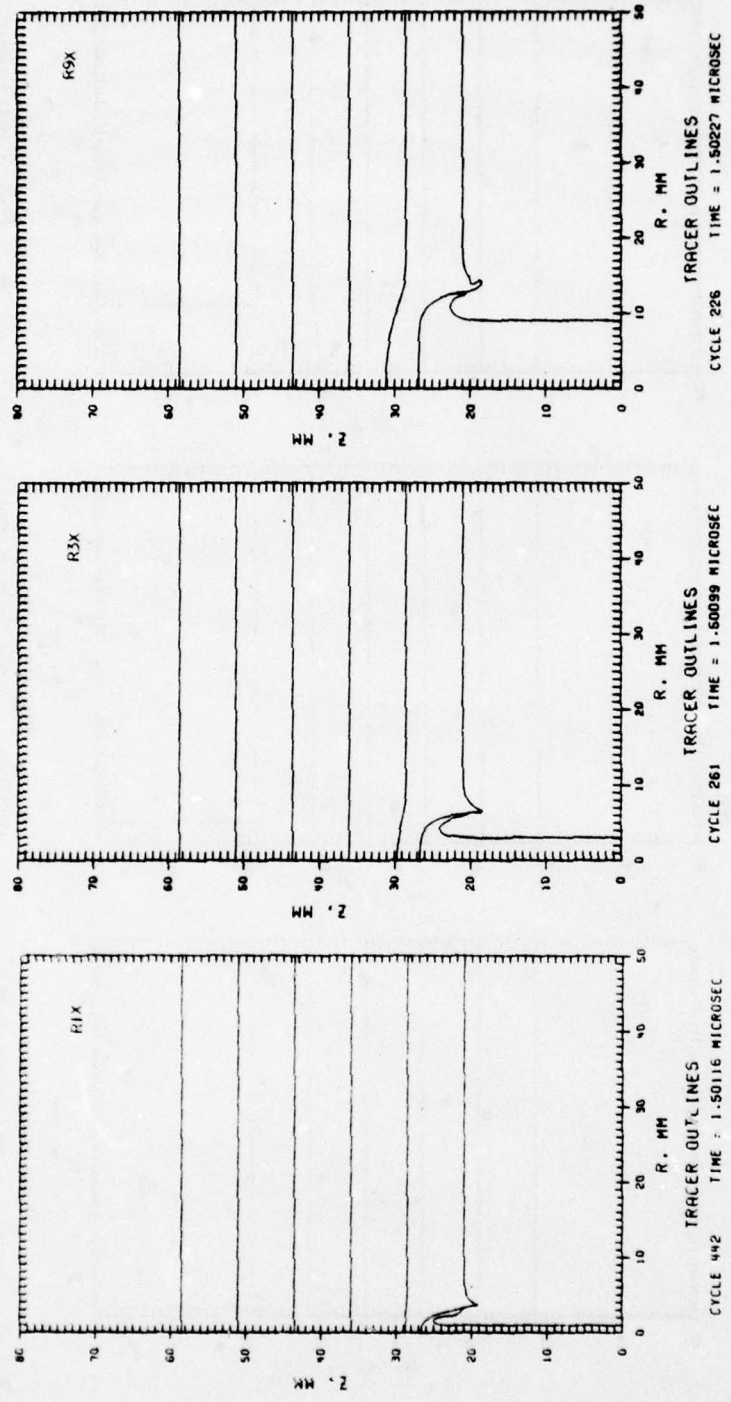


Figure 31. Comparison of the Deformation of a 37.5-mm Steel Target Impacted by 1, 3, and 9-mm Copper Rods

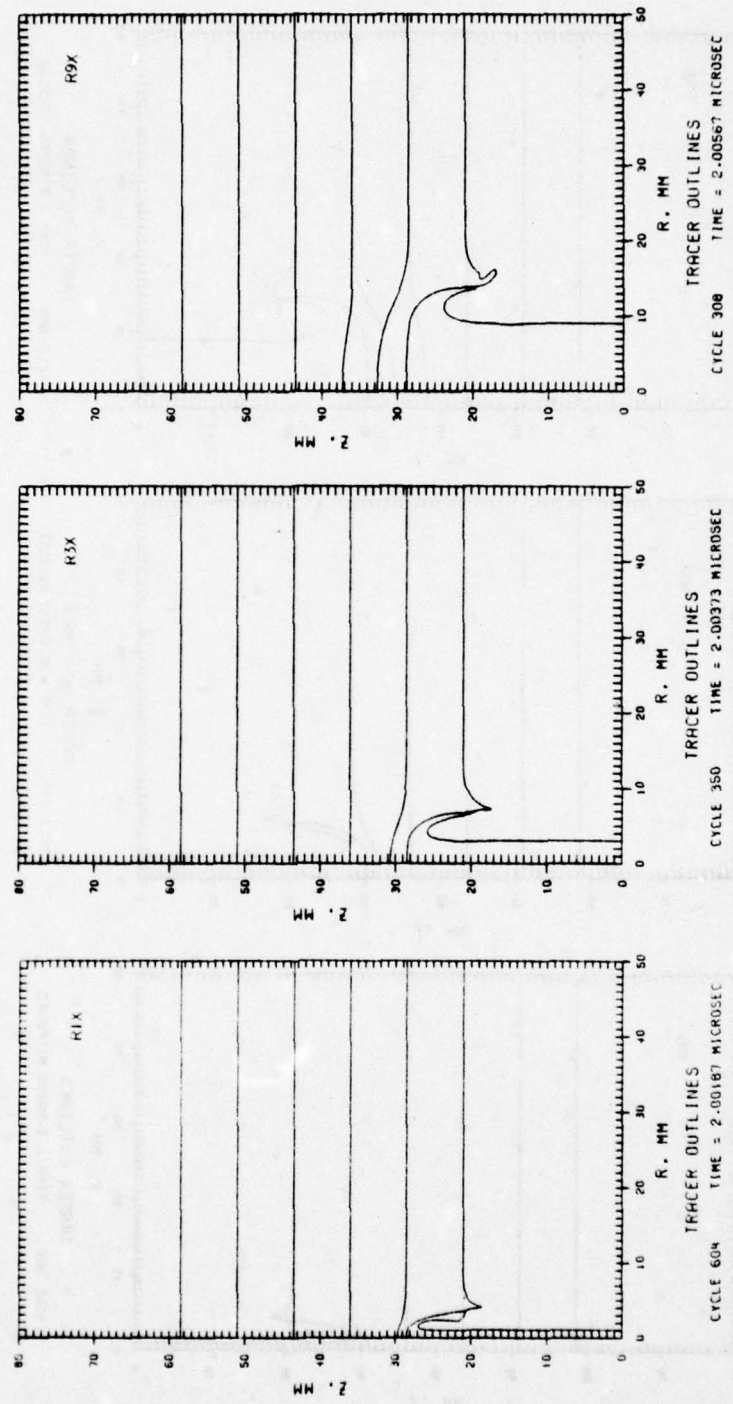


Figure 32. Comparison of the Deformation of a 37.5-mm Steel Target Impacted by 1, 3, and 9-mm Copper Rods

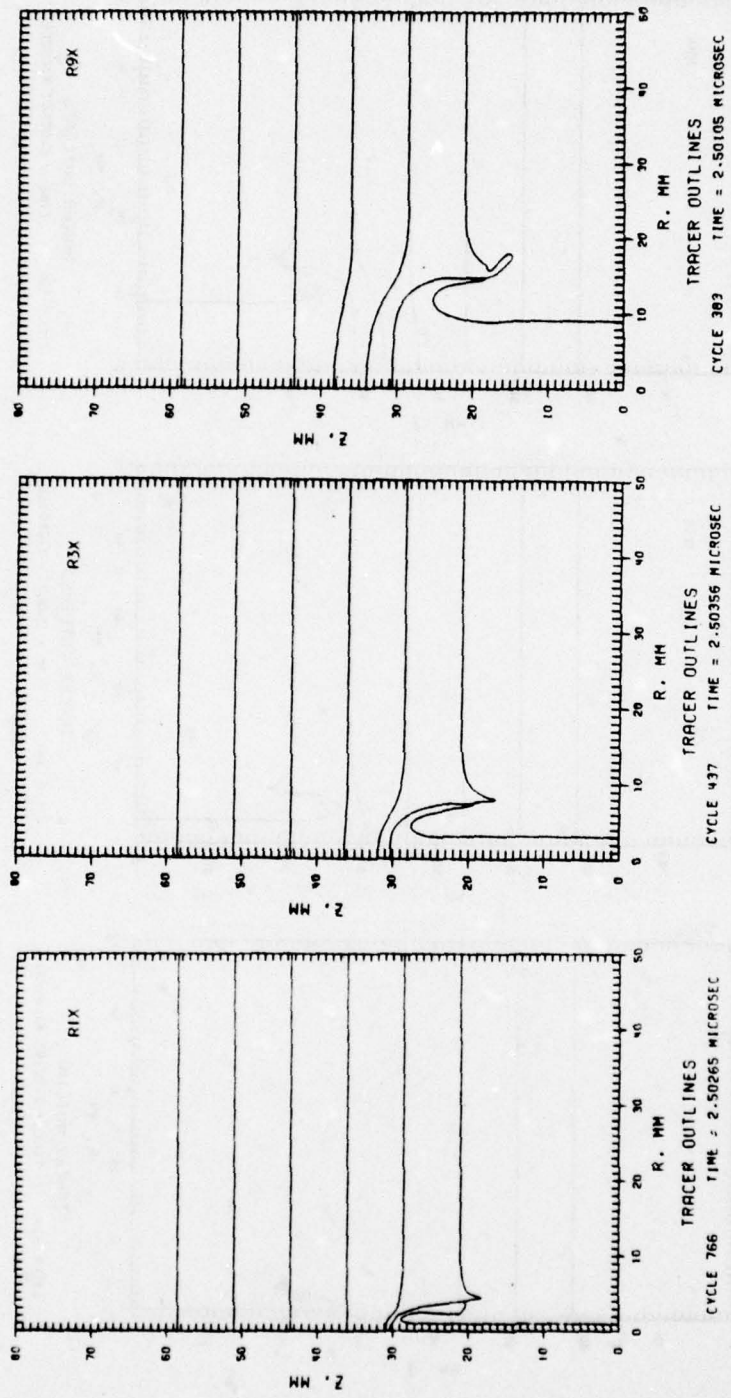


Figure 33. Comparison of the Deformation of a 37.5-mm Steel Target Impacted by 1, 3, and 9-mm Copper Rods

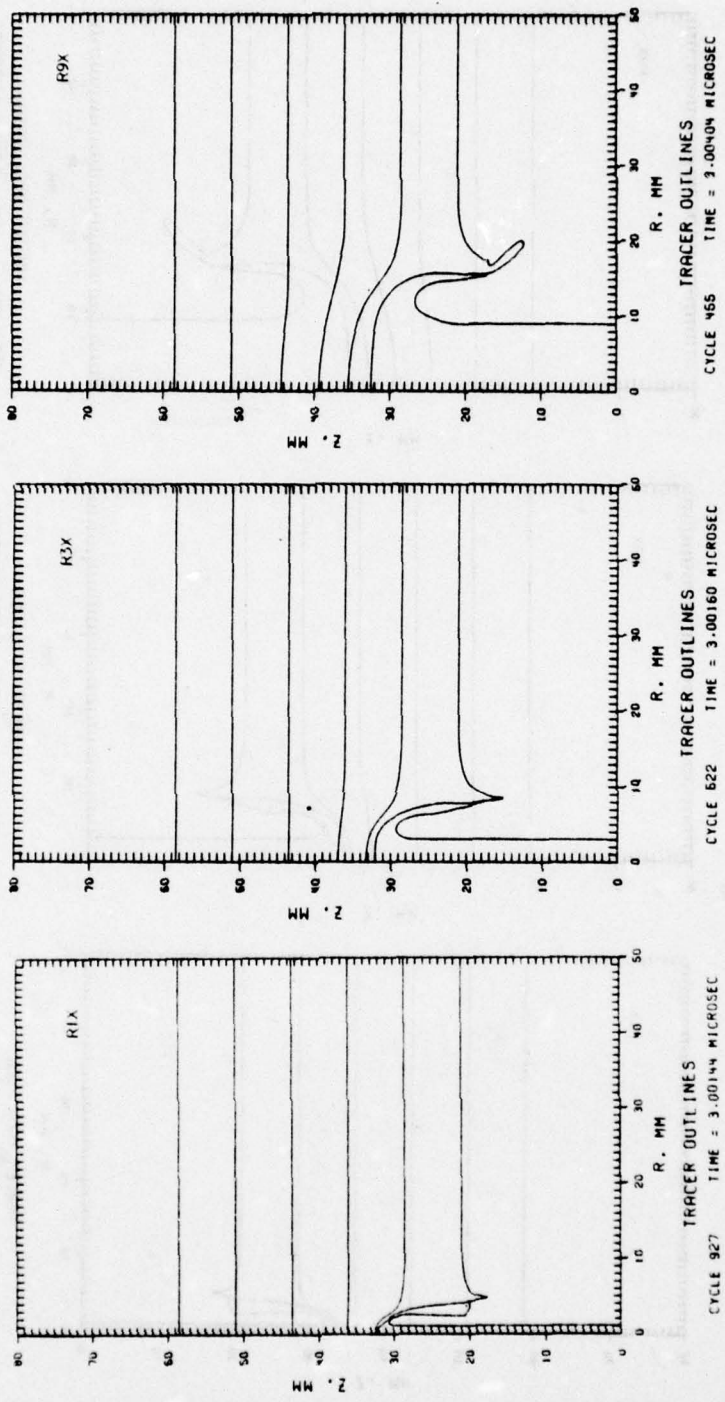


Figure 34. Comparison of the Deformation of a 37.5-mm Steel Target Impacted by 1, 3, and 9-mm Copper Rods

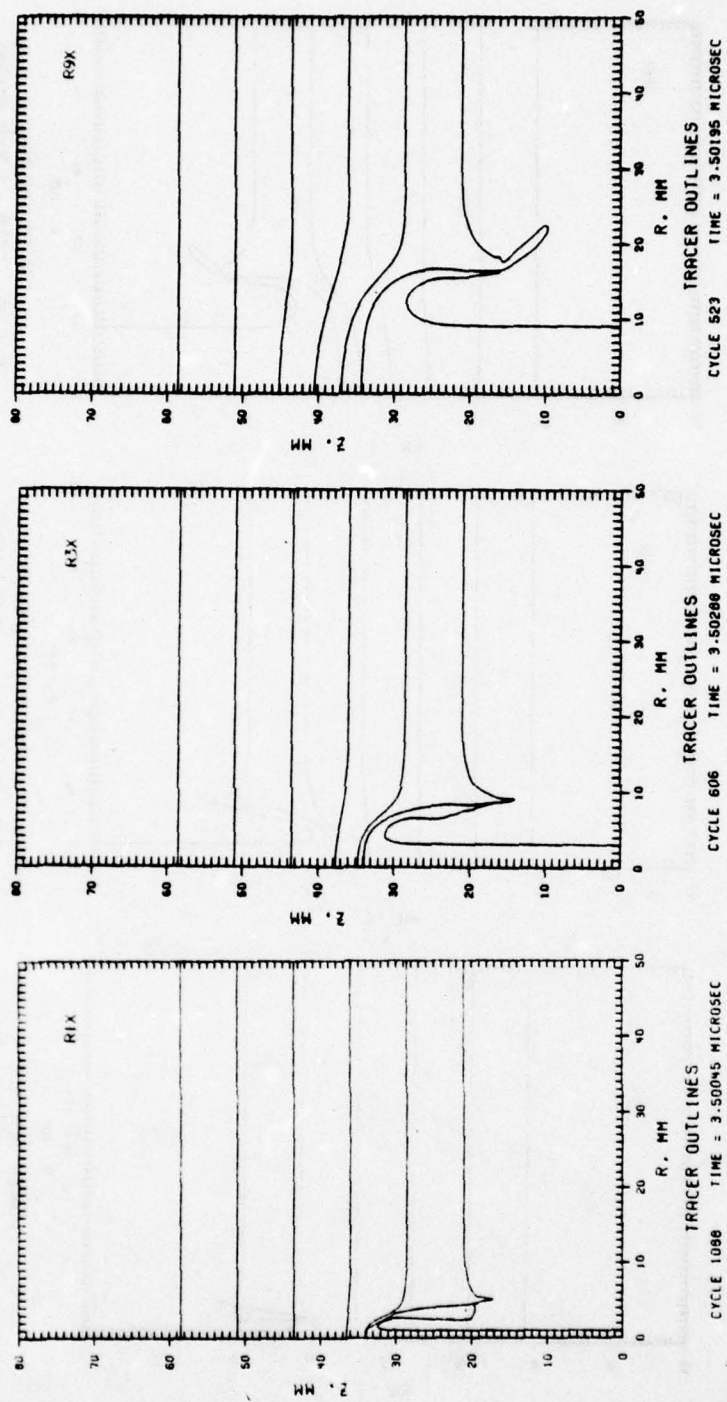


Figure 35. Comparison of the Deformation of a 37.5-mm Steel Target Impacted by 1, 3, and 9-mm Copper Rods

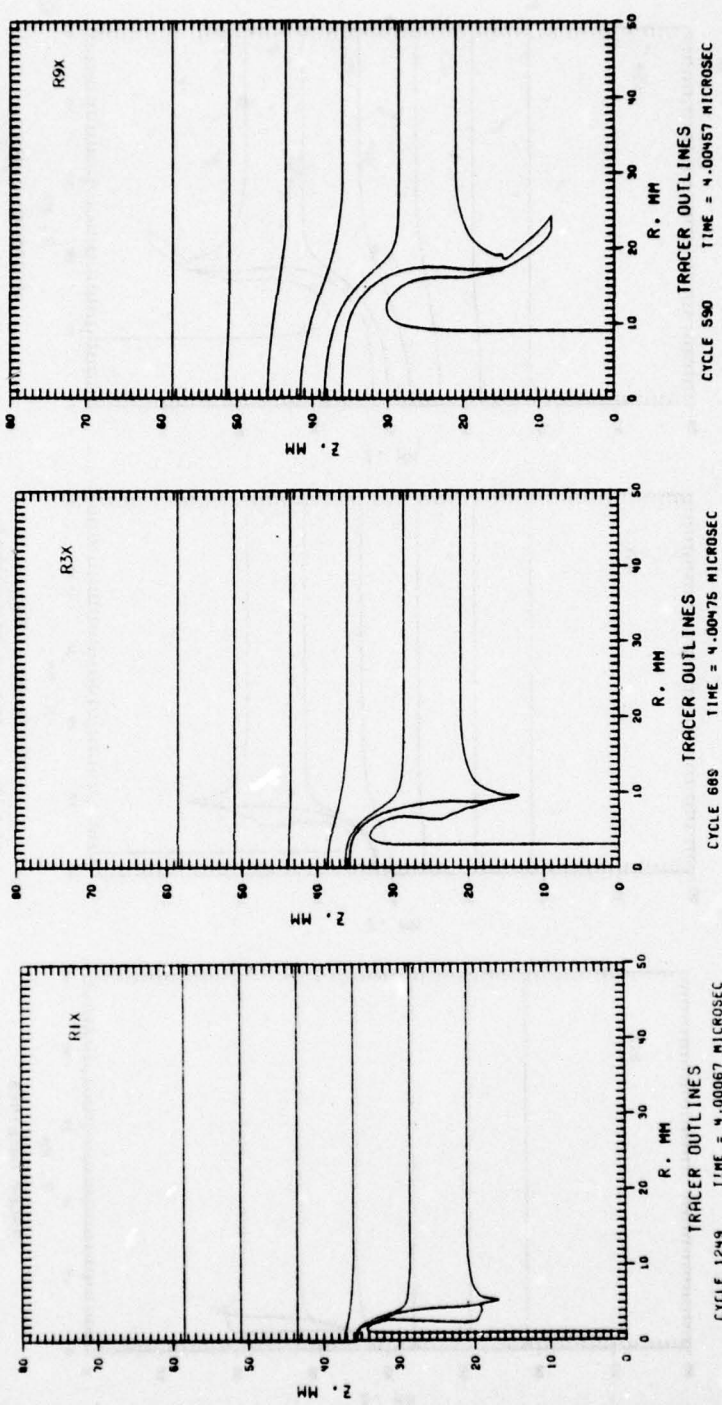


Figure 36. Comparison of the Deformation of a 37.5-mm Steel Target Impacted by 1, 3, and 9-mm Copper Rods

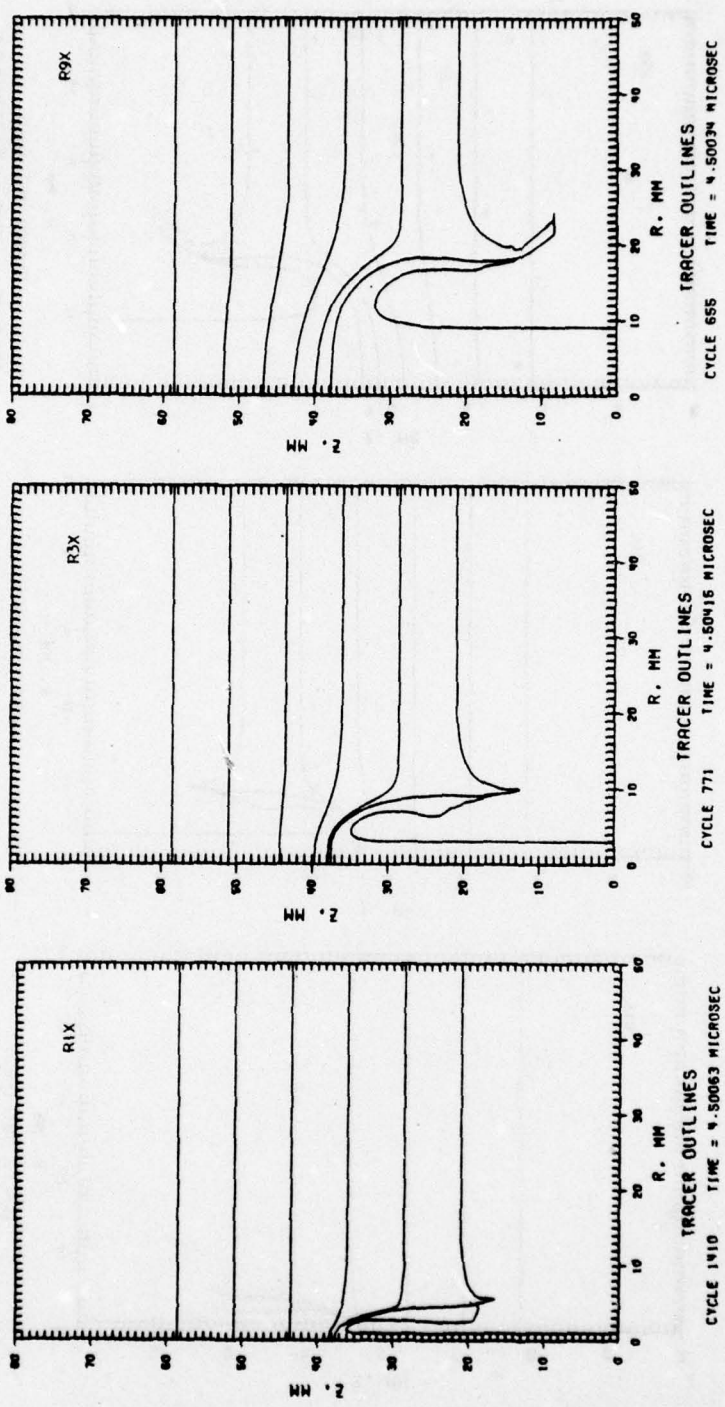


Figure 37. Comparison of the Deformation of a 37.5-mm Steel Target Impacted by 1, 3, and 9-mm Copper Rods

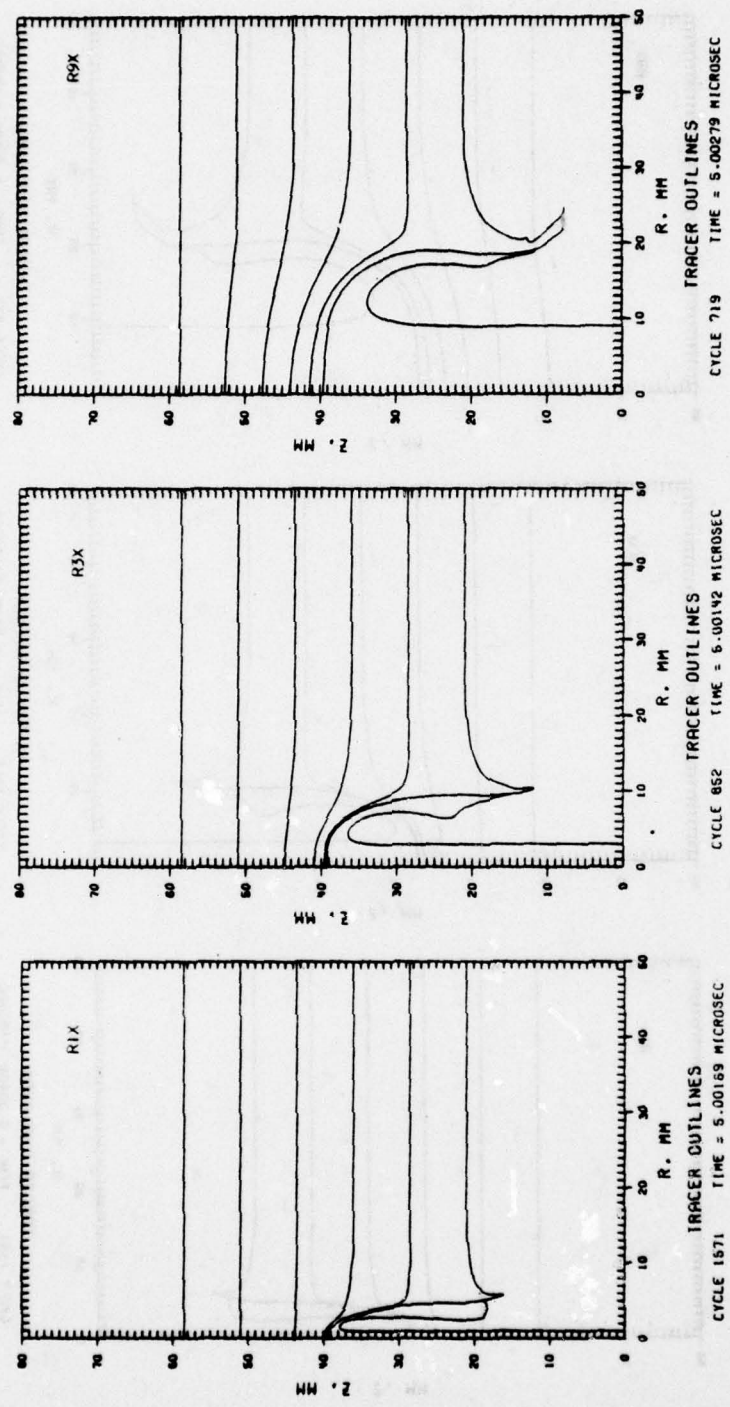


Figure 38. Comparison of the Deformation of a 37.5-mm Steel Target Impacted by 1, 3, and 9-mm Copper Rods

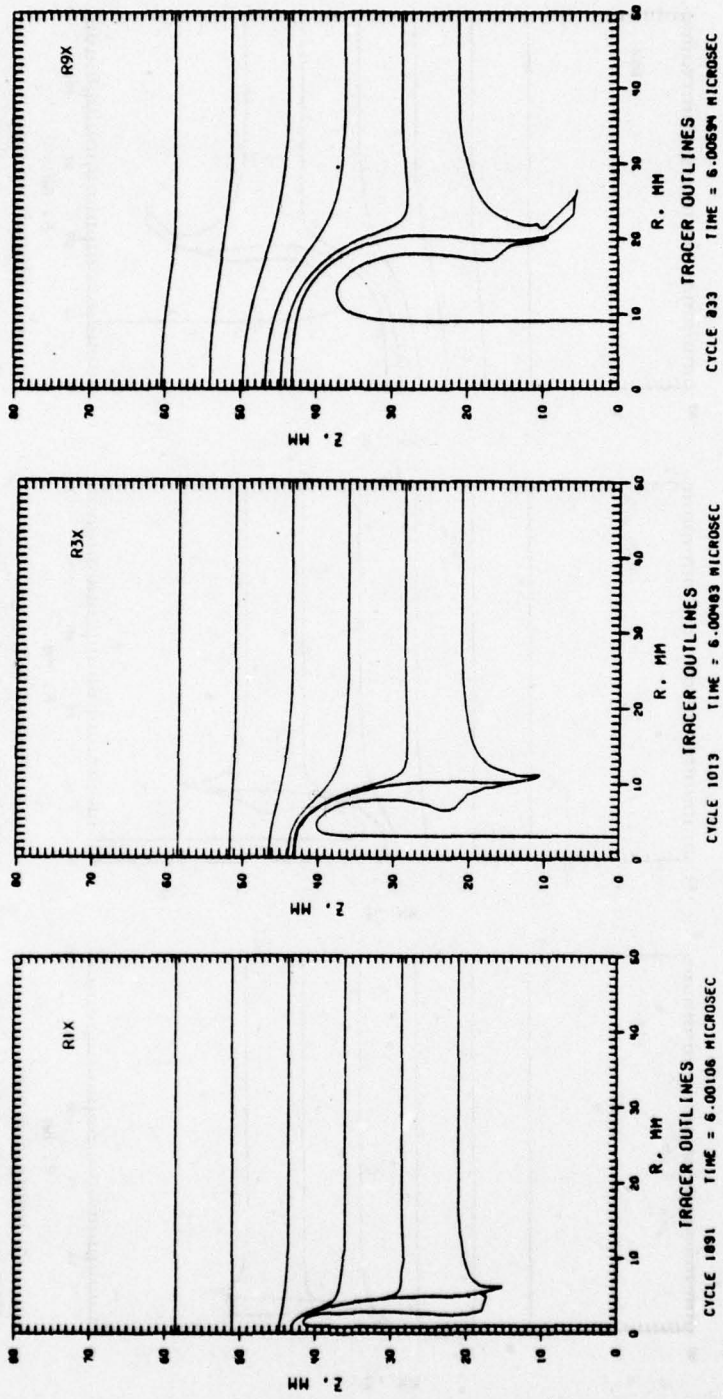


Figure 39. Comparison of the Deformation of a 37.5-mm Steel Target Impacted by 1, 3, and 9-mm Copper Rods

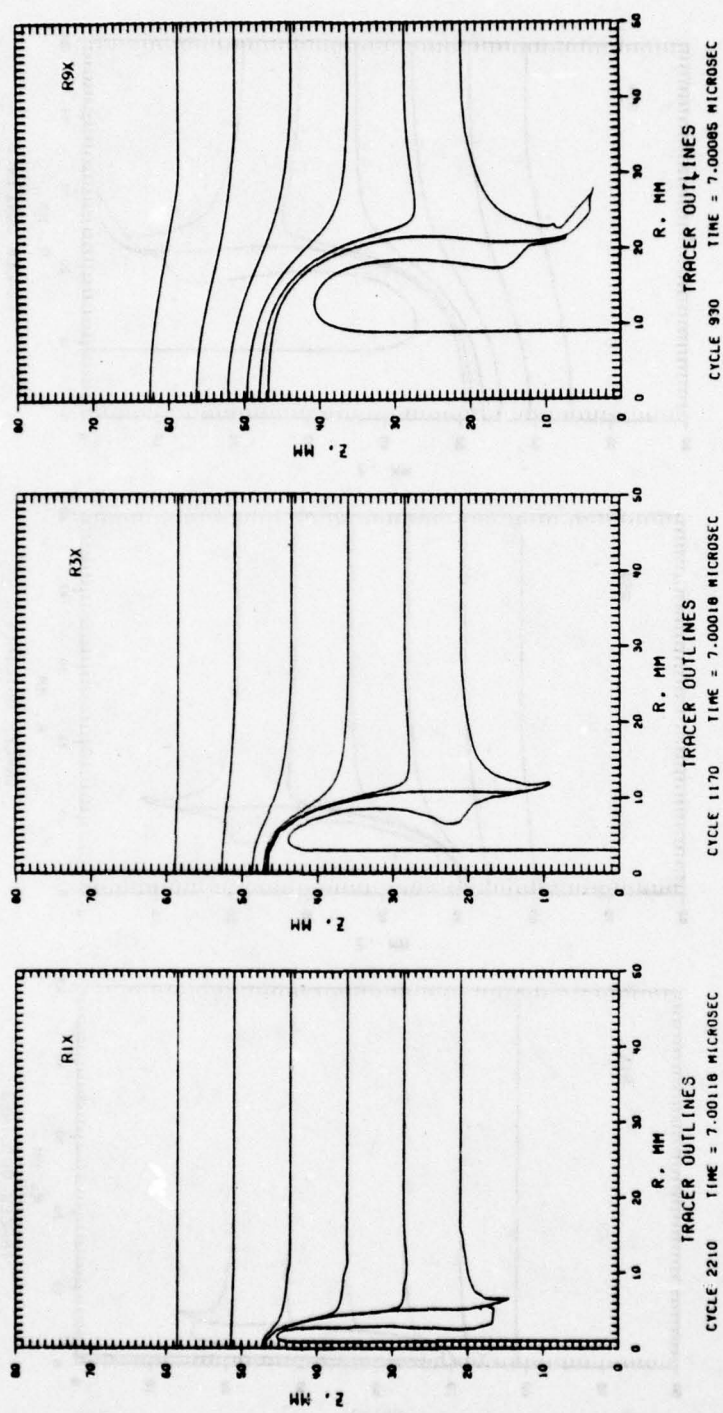


Figure 40. Comparison of the Deformation of a 37.5-mm Steel Target Impacted by 1, 3, and 9-mm Copper Rods

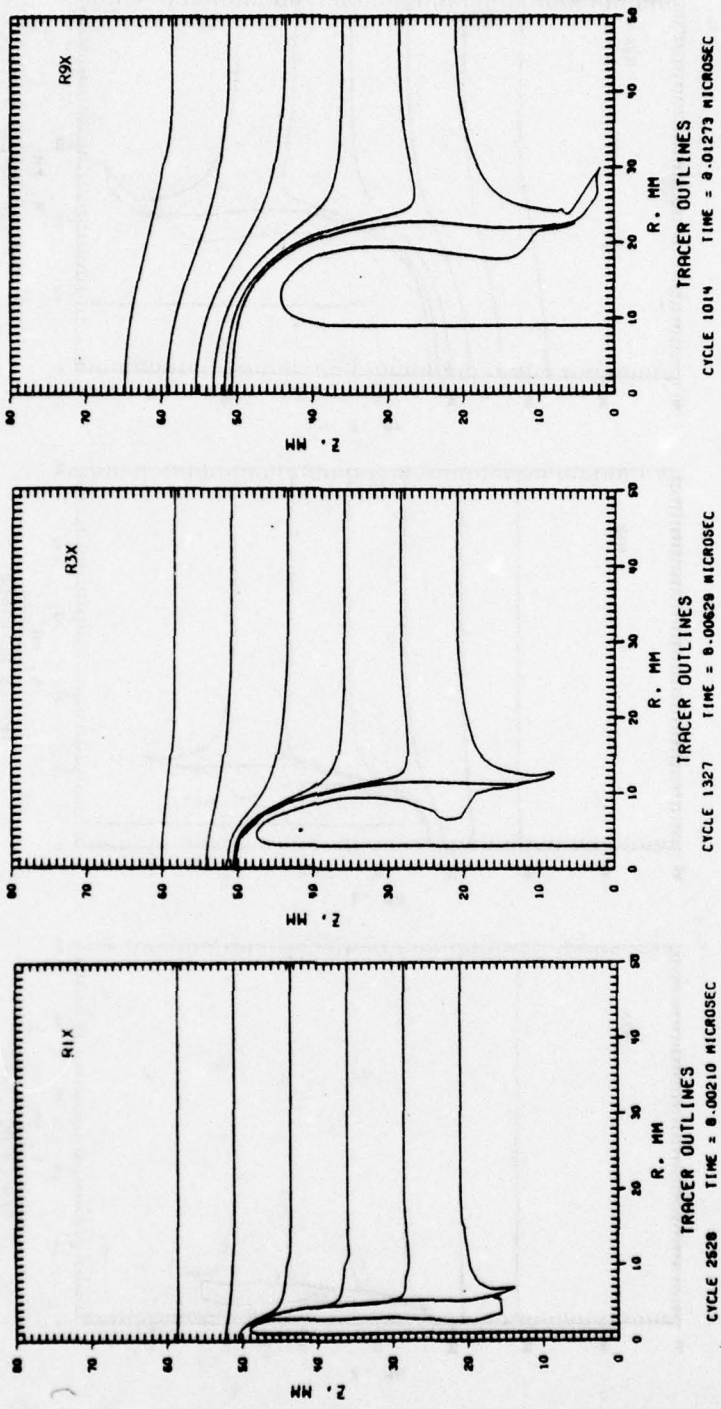


Figure 41. Comparison of the Deformation of a 37.5-mm Steel Target Impacted by 1, 3, and 9-mm Copper Rods

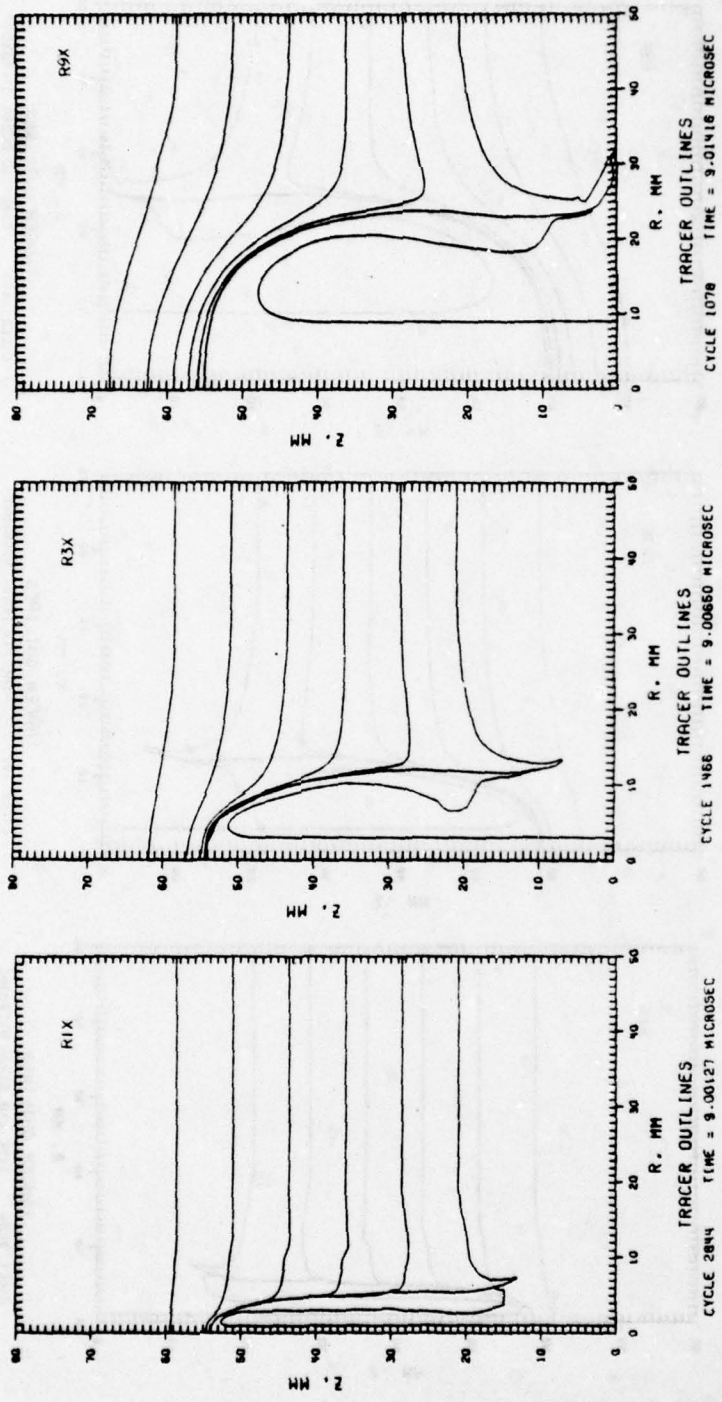


Figure 42. Comparison of the Deformation of a 37.5-mm Steel Target Impacted by 1, 3, and 9-mm Copper Rods

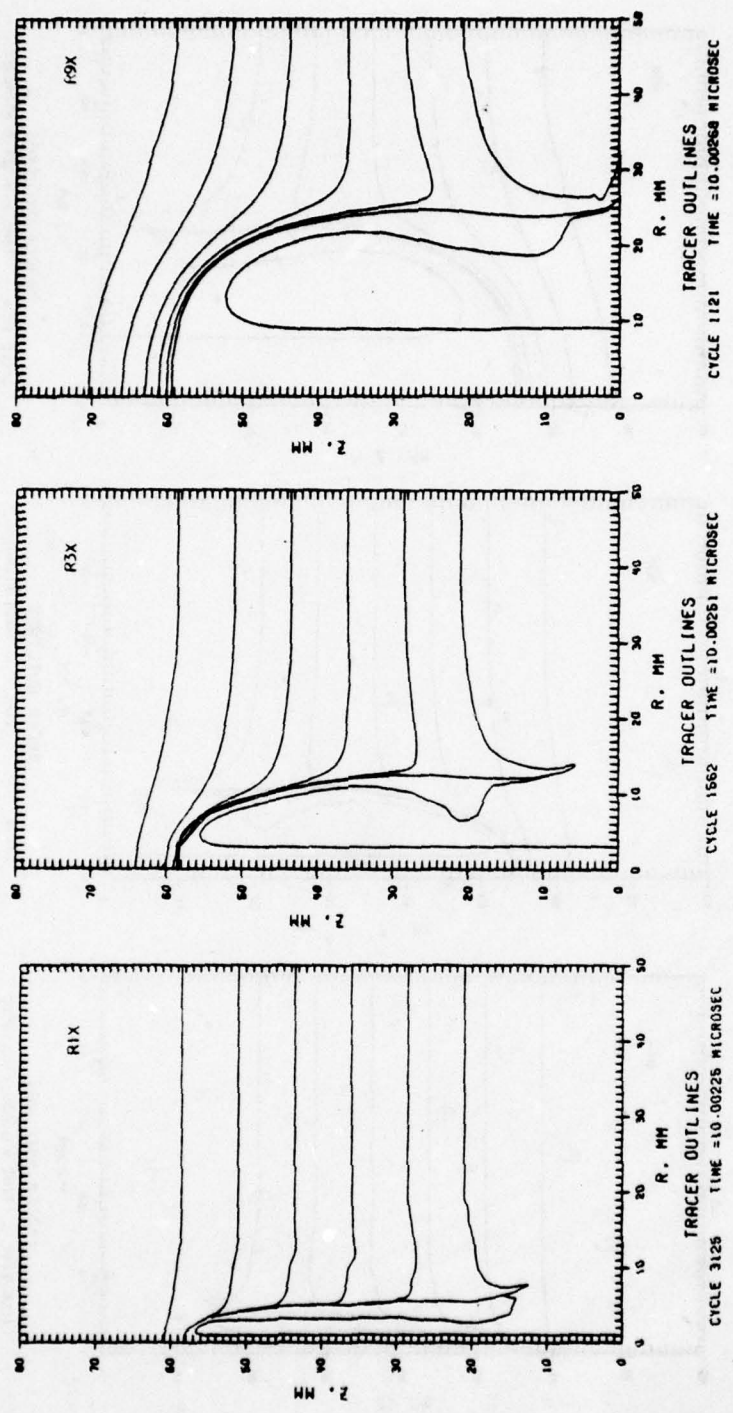


Figure 43. Comparison of the Deformation of a 37.5-mm Steel Target Impacted by 1, 3, and 9-mm Copper Rods

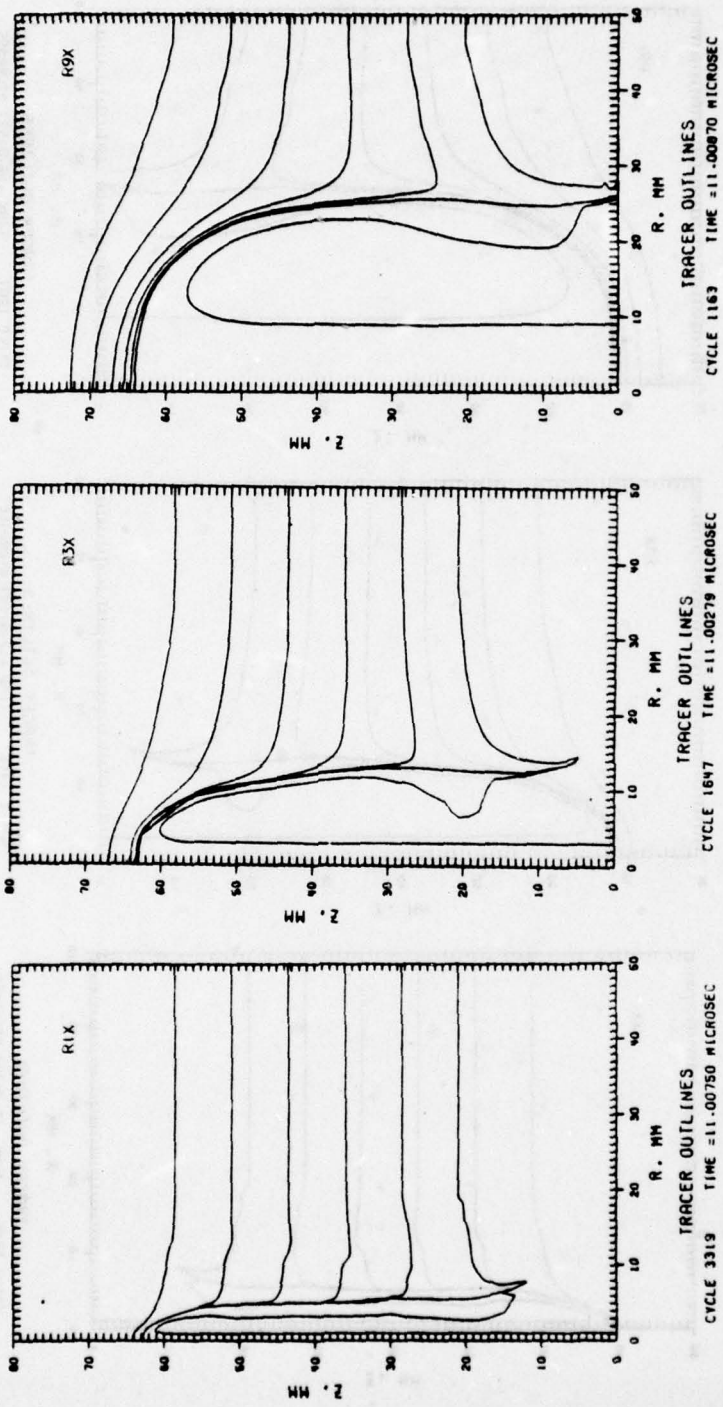


Figure 44. Comparison of the Deformation of a 37.5-mm Steel Target Impacted by 1, 3, and 9-mm Copper Rods

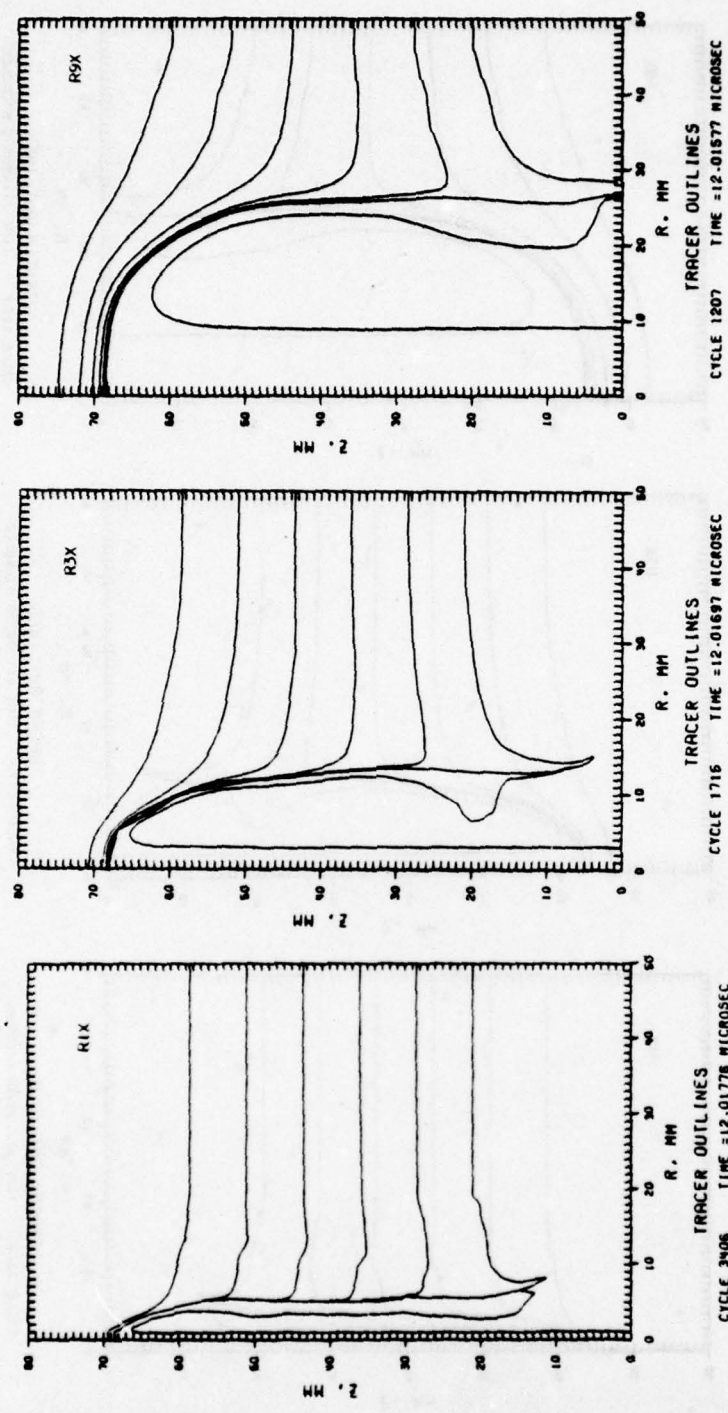


Figure 45. Comparison of the Deformation of a 37.5-mm Steel Target Impacted by 1, 3, and 9-mm Copper Rods

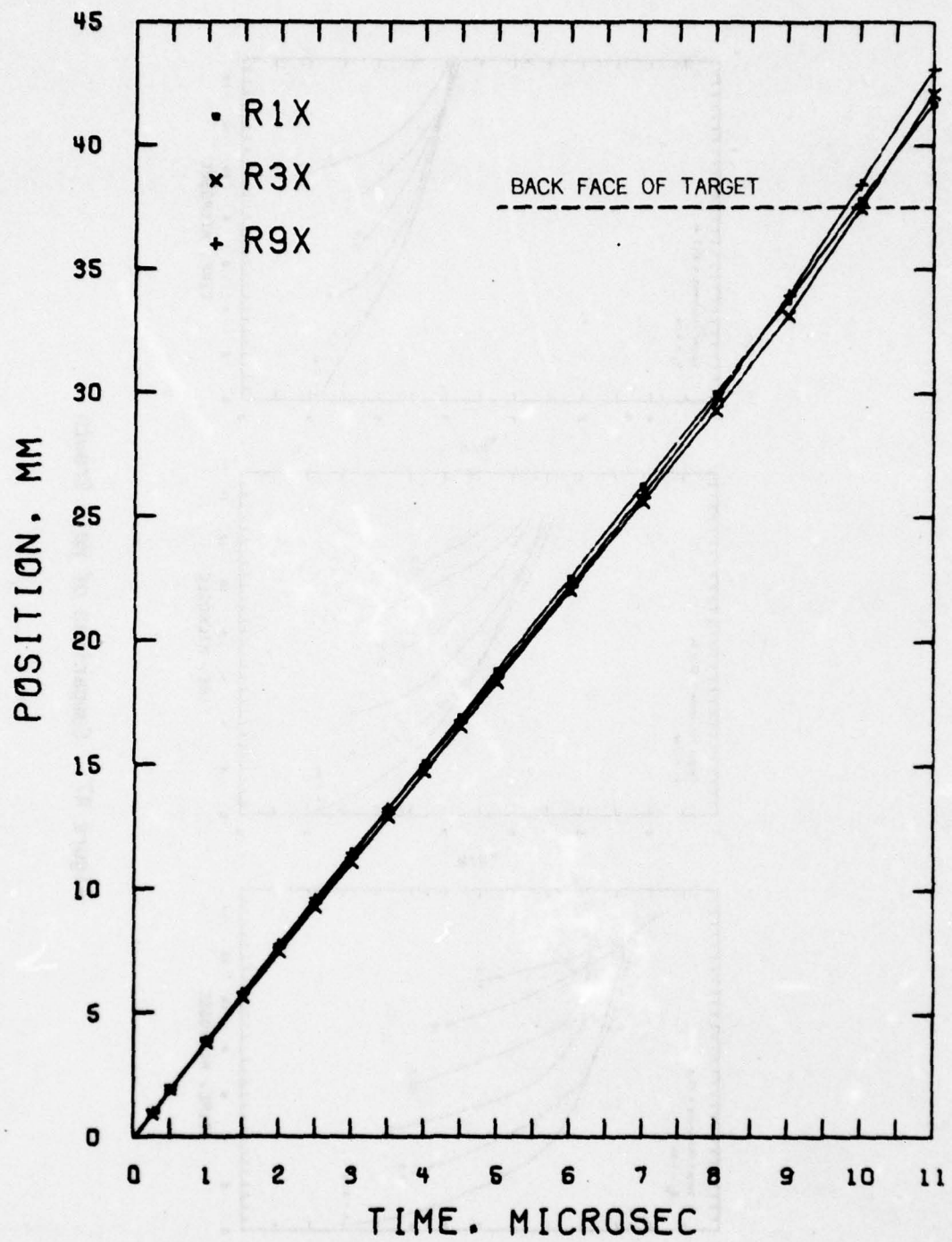


Figure 46. Position of the Rod-Target Interface
on the Axis of Symmetry Versus Time

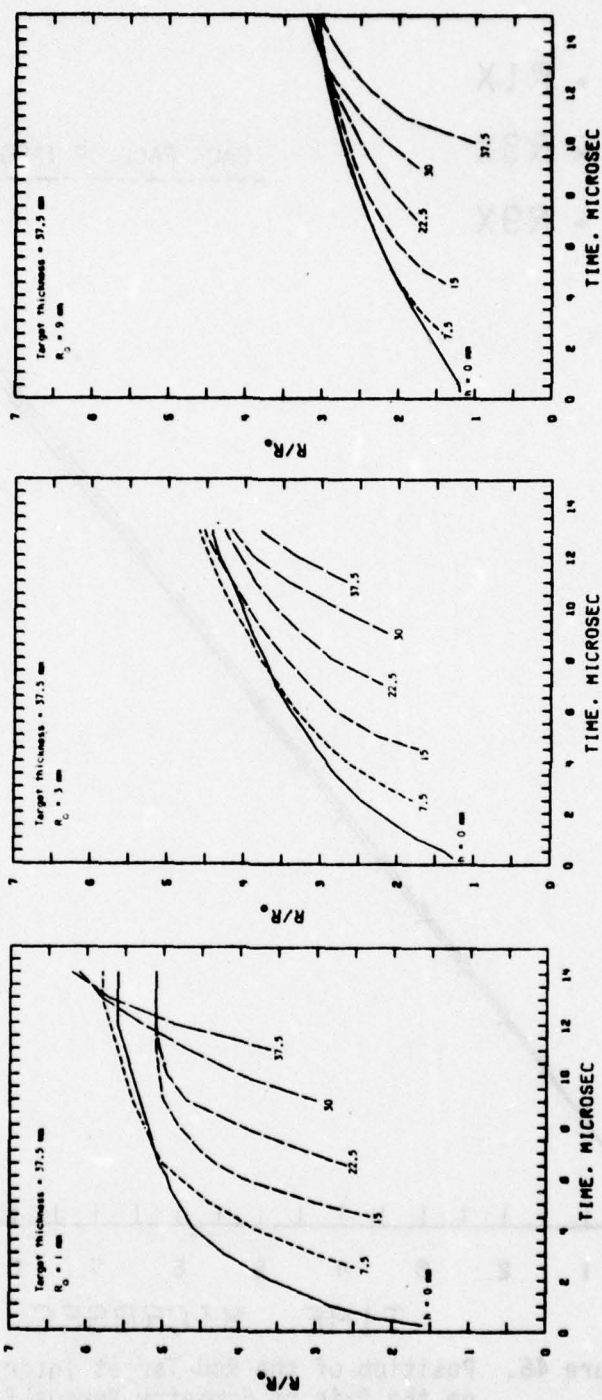


Figure 47. Comparison of Hole Growth

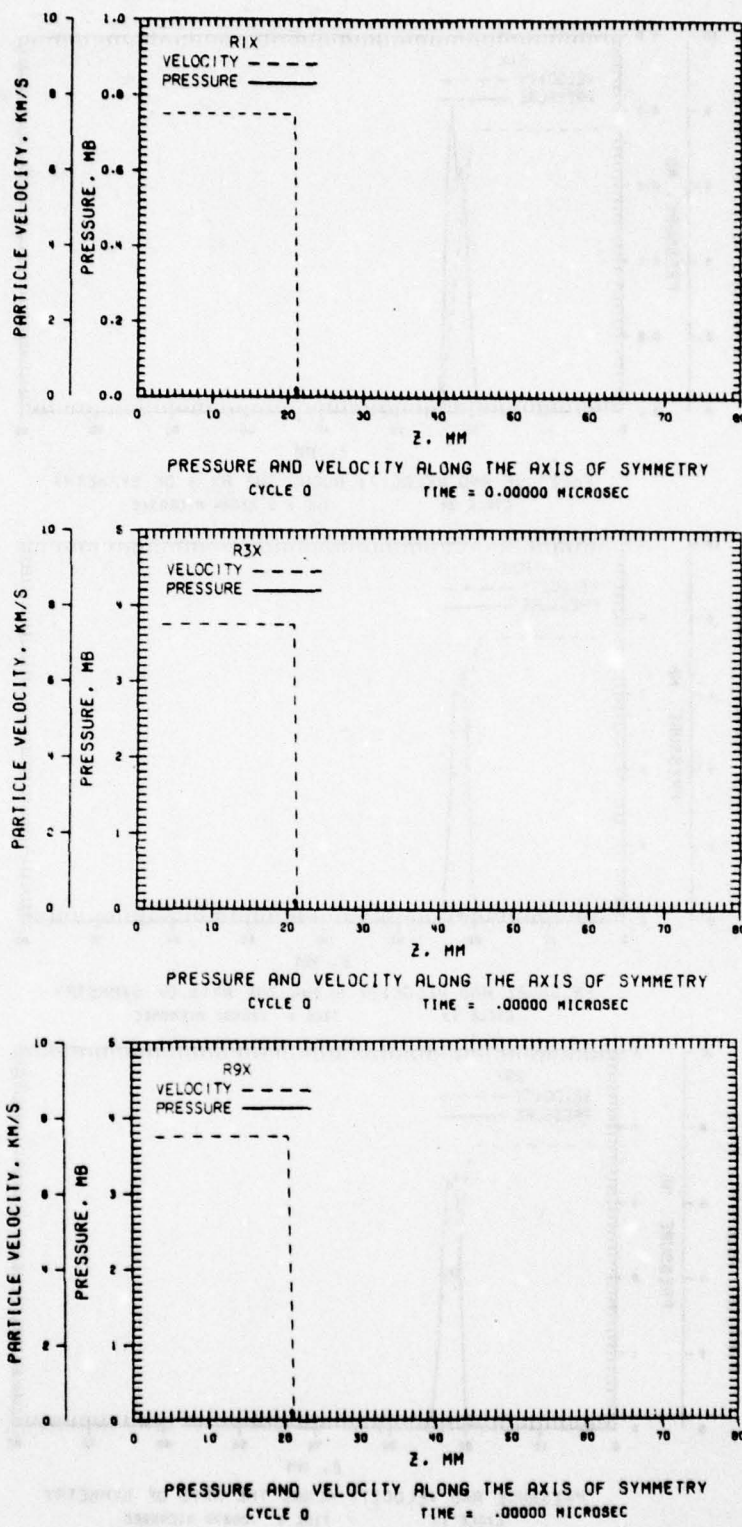


Figure 48. Comparison of Pressure and Velocity Profiles

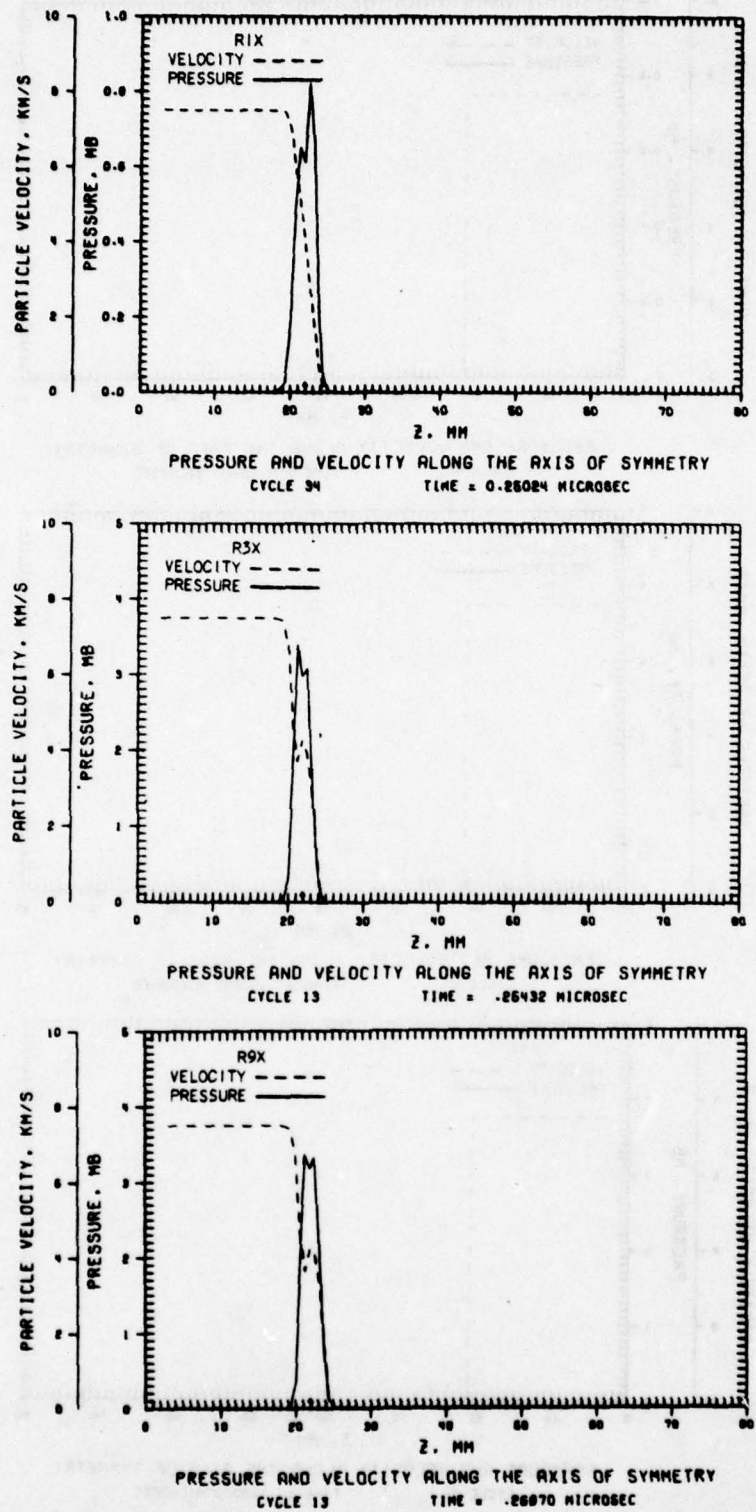


Figure 49. Comparison of Pressure and Velocity Profiles

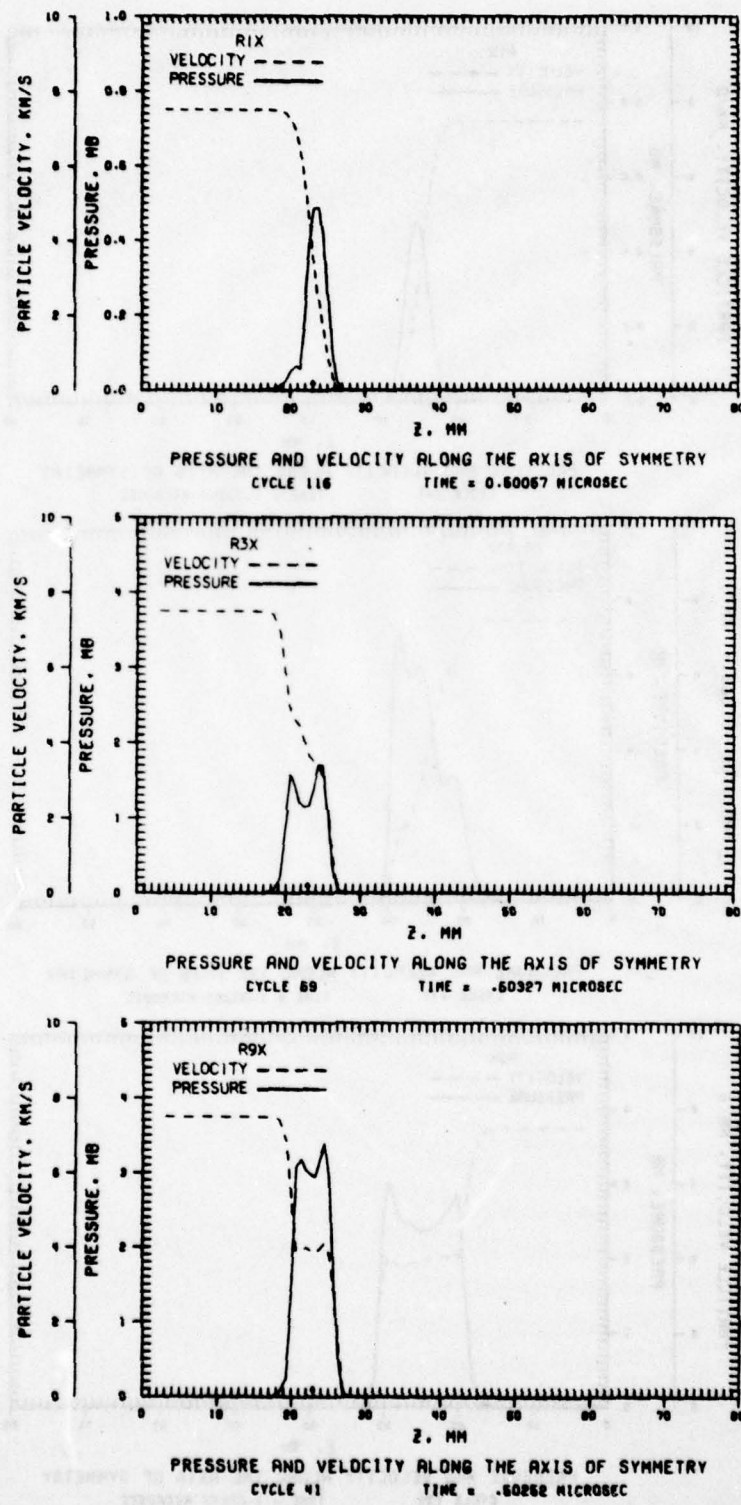


Figure 50. Comparison of Pressure and Velocity Profiles

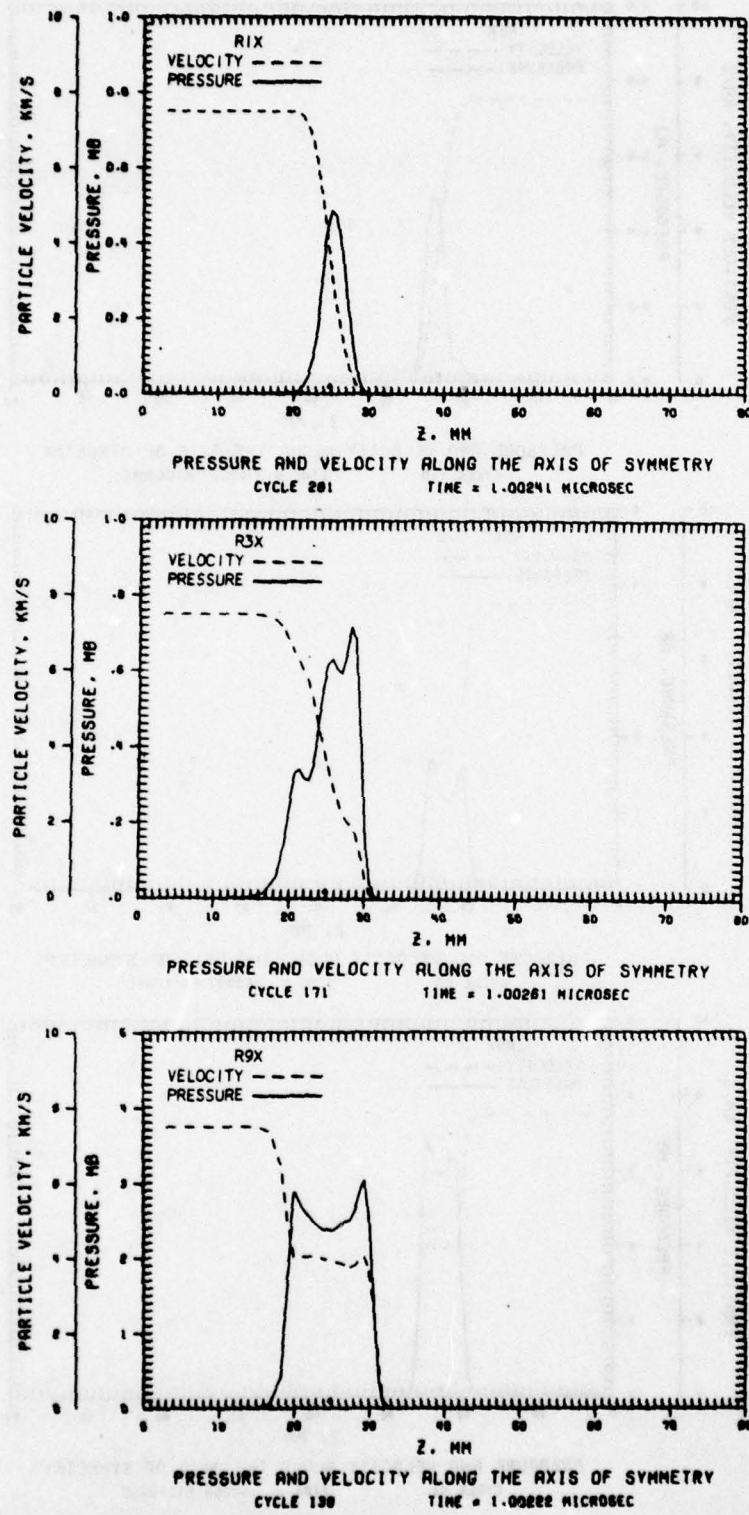


Figure 51. Comparison of Pressure and Velocity Profiles

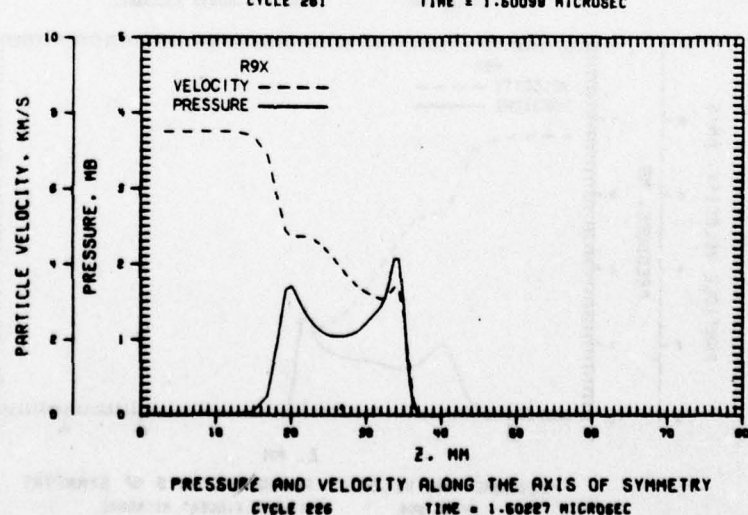
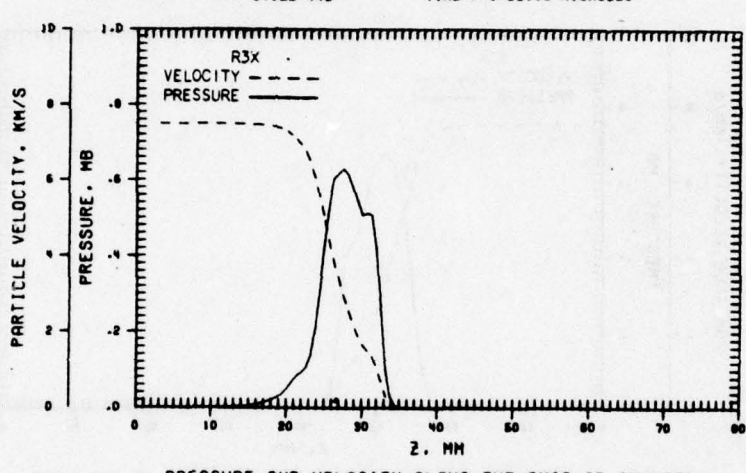
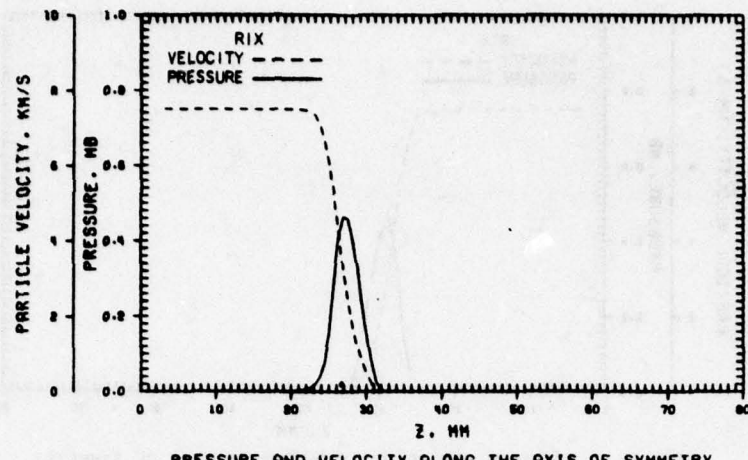


Figure 52. Comparison of Pressure and Velocity Profiles

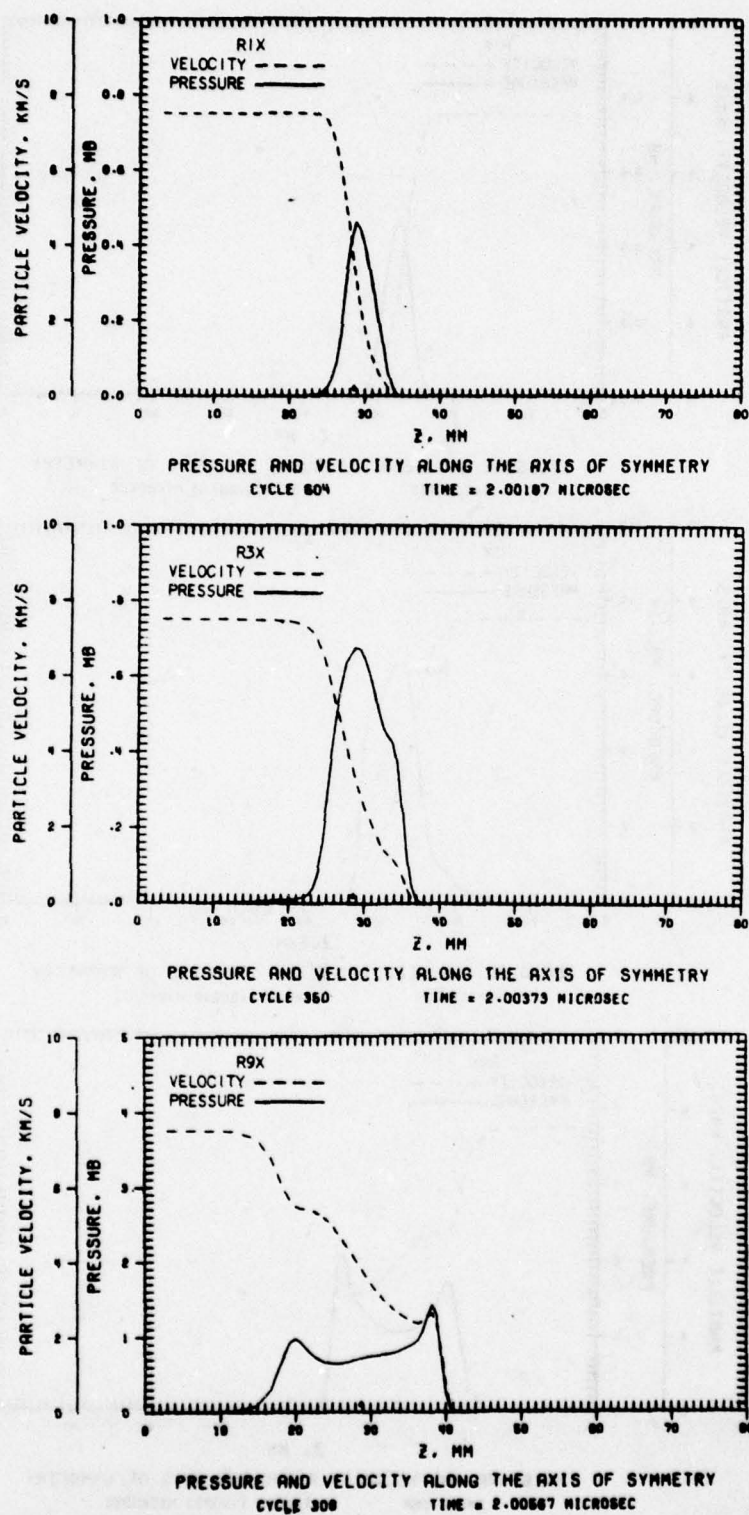


Figure 53. Comparison of Pressure and Velocity Profiles

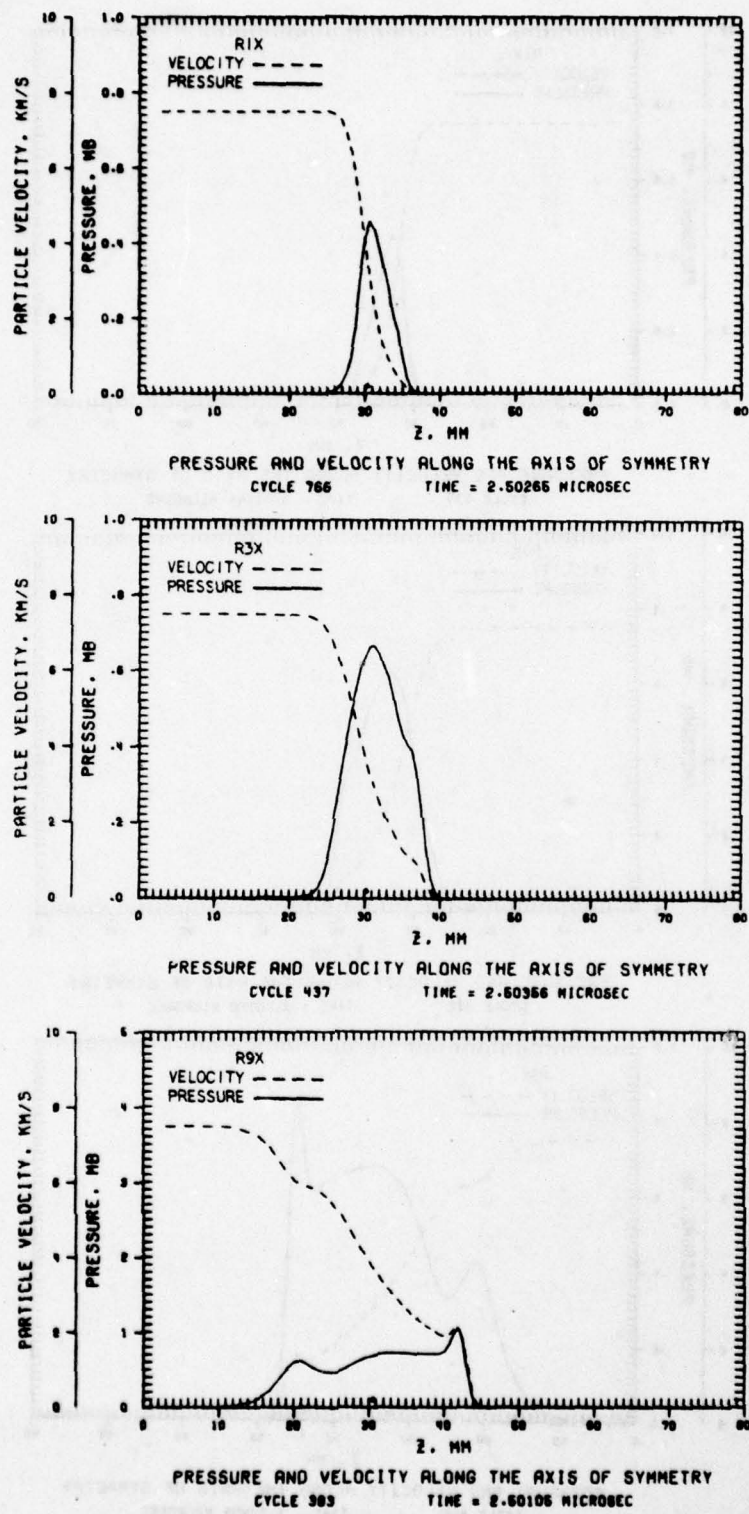


Figure 54. Comparison of Pressure and Velocity Profiles

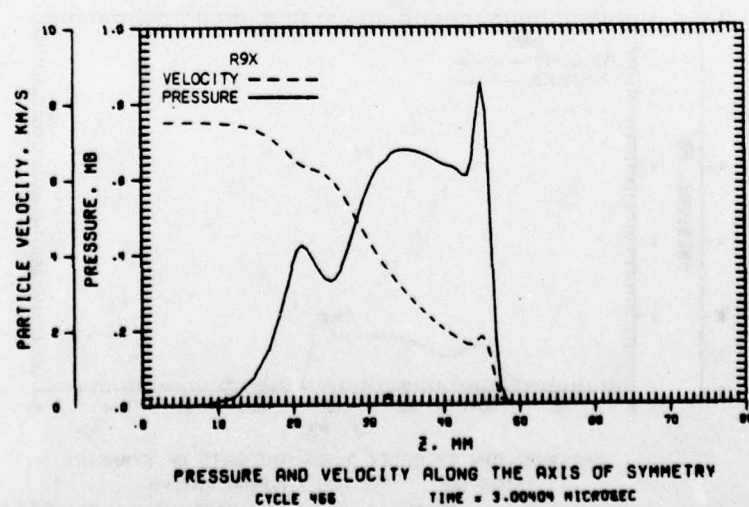
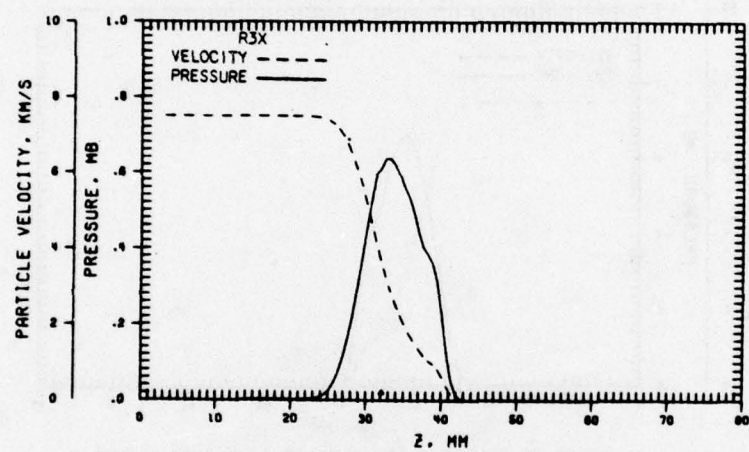
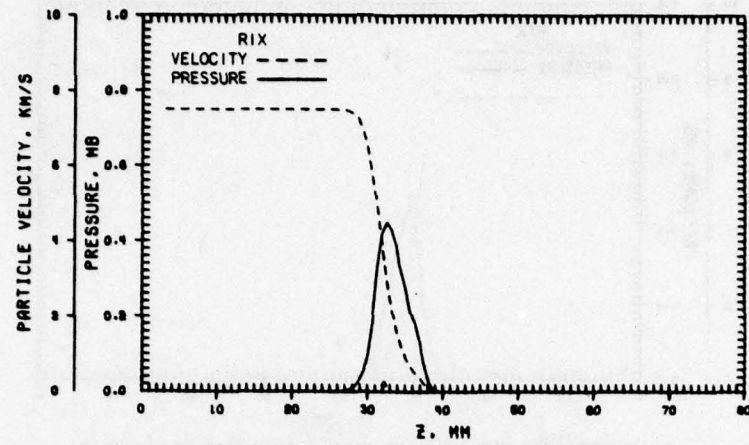


Figure 55. Comparison of Pressure and Velocity Profiles

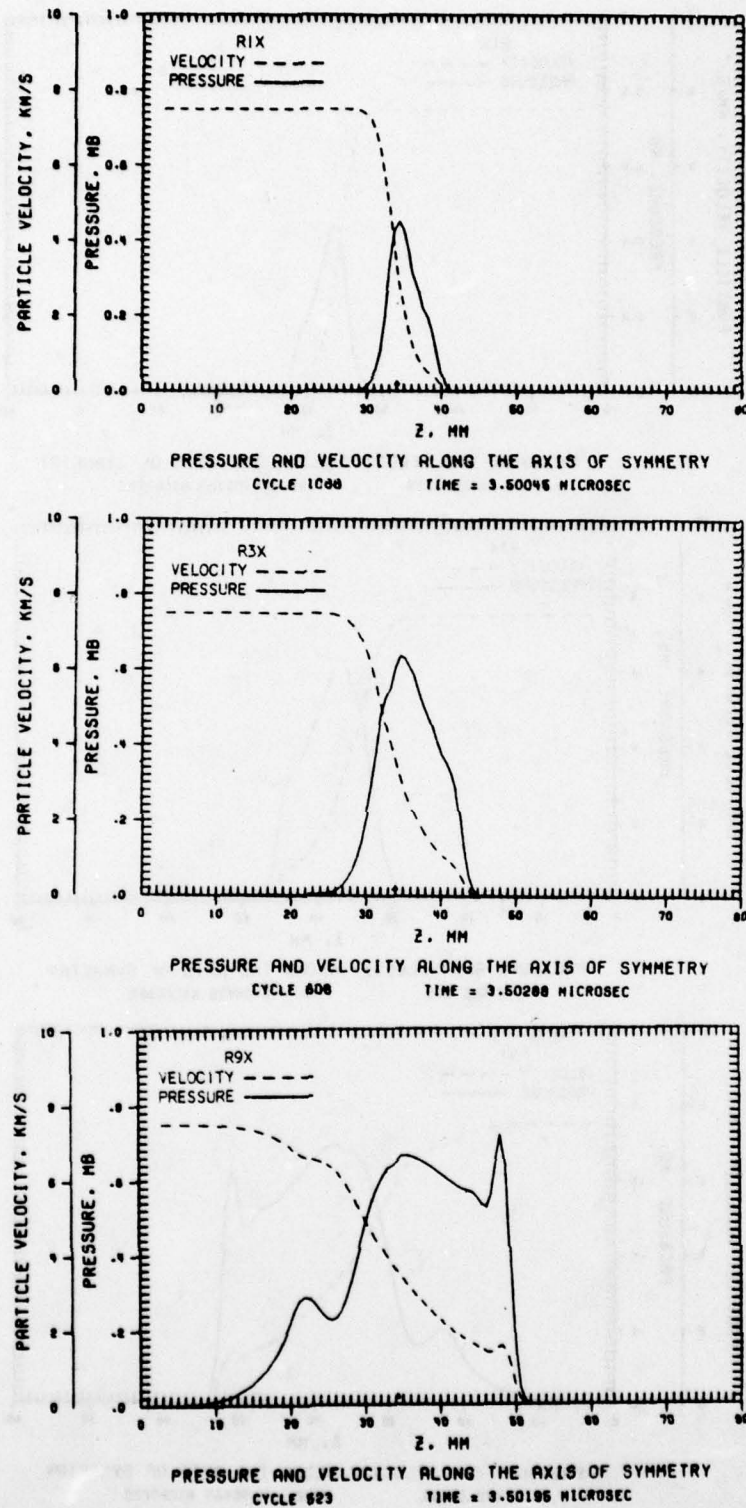


Figure 56. Comparison of Pressure and Velocity Profiles

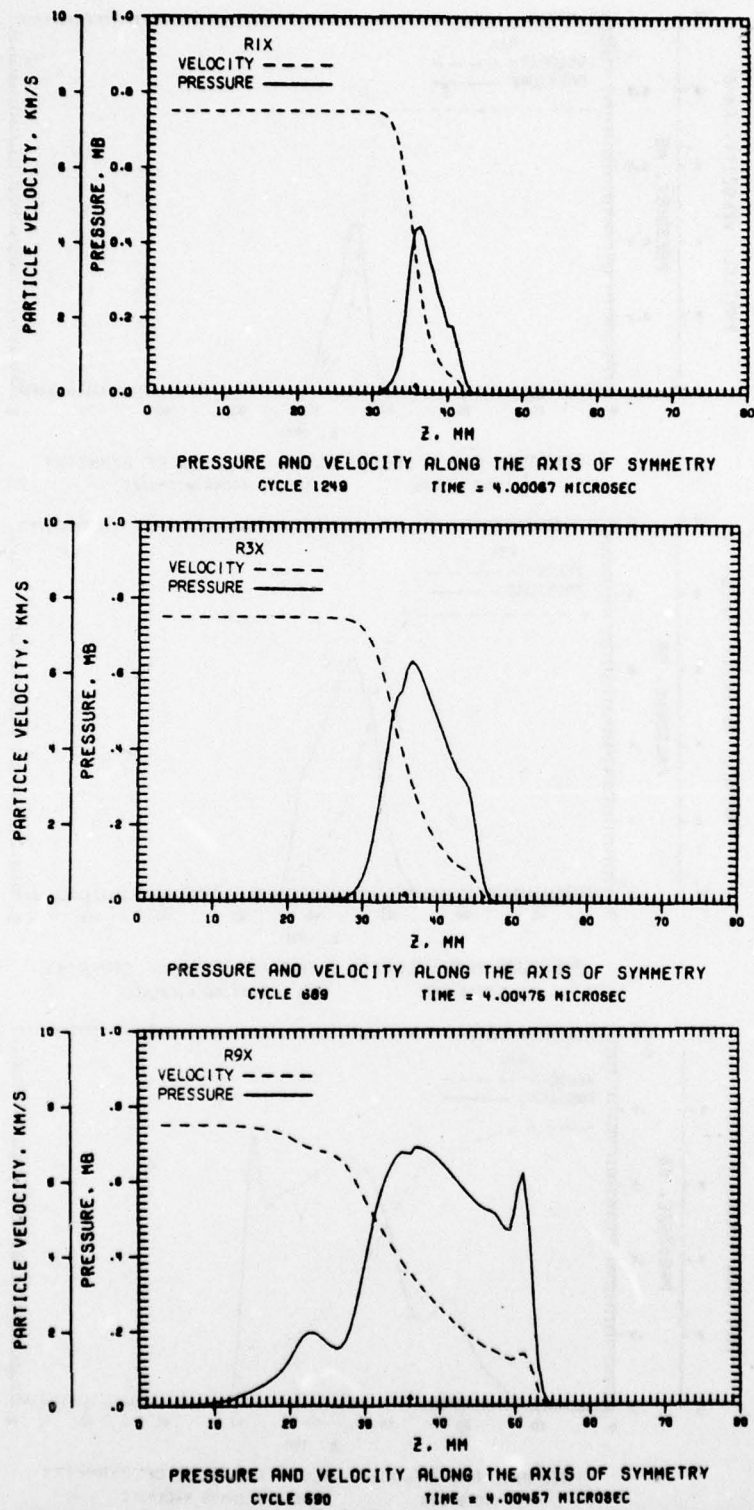


Figure 57. Comparison of Pressure and Velocity Profiles

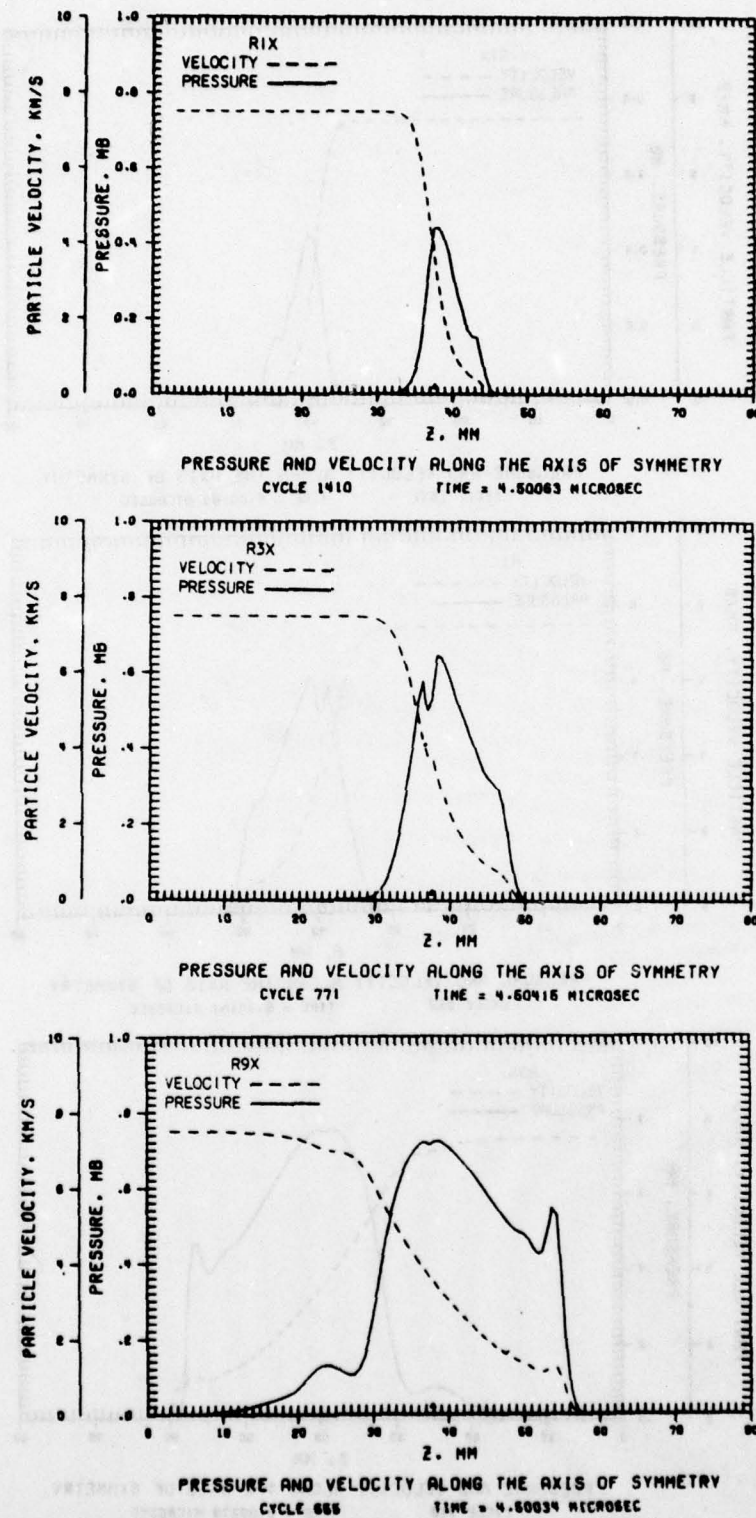


Figure 58. Comparison of Pressure and Velocity Profiles

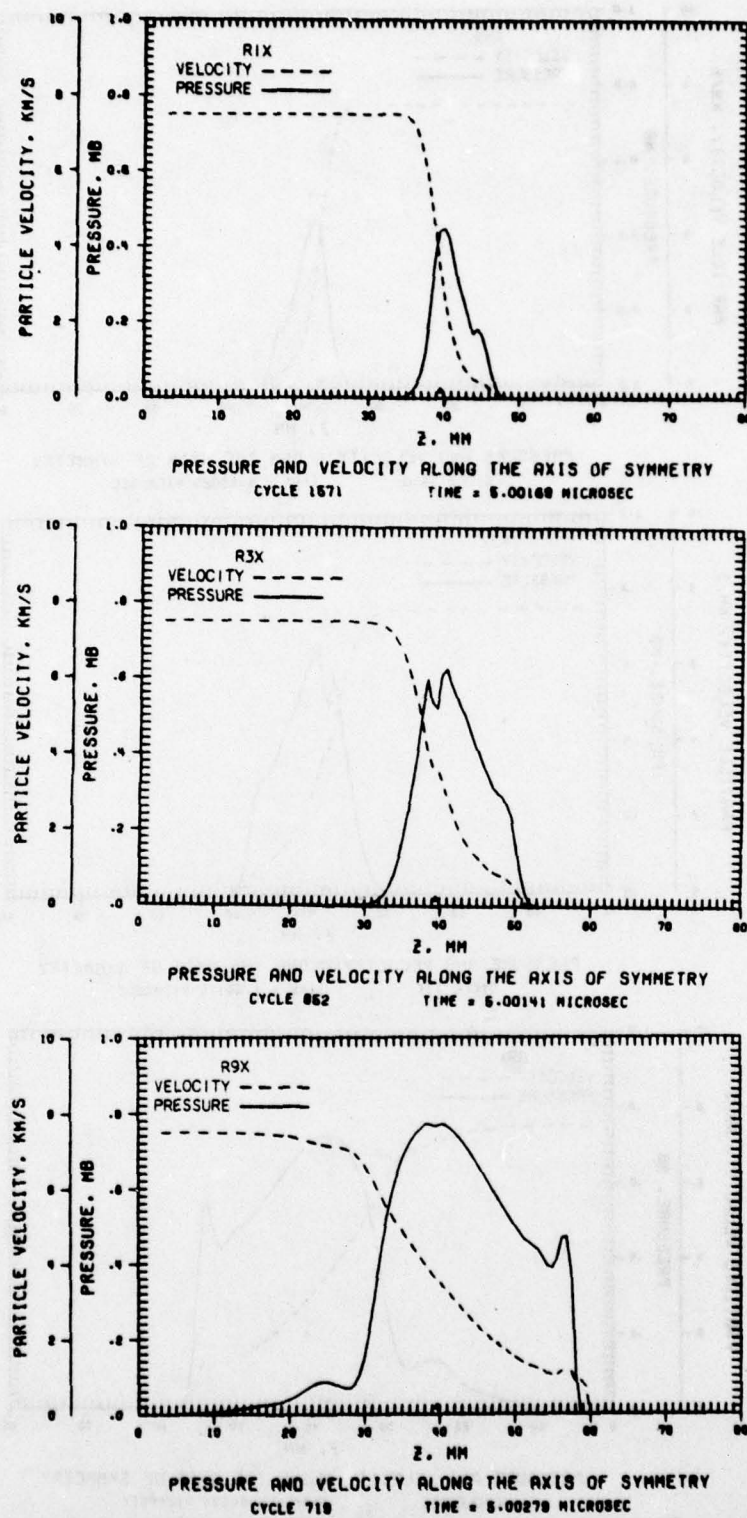


Figure 59. Comparison of Pressure and Velocity Profiles

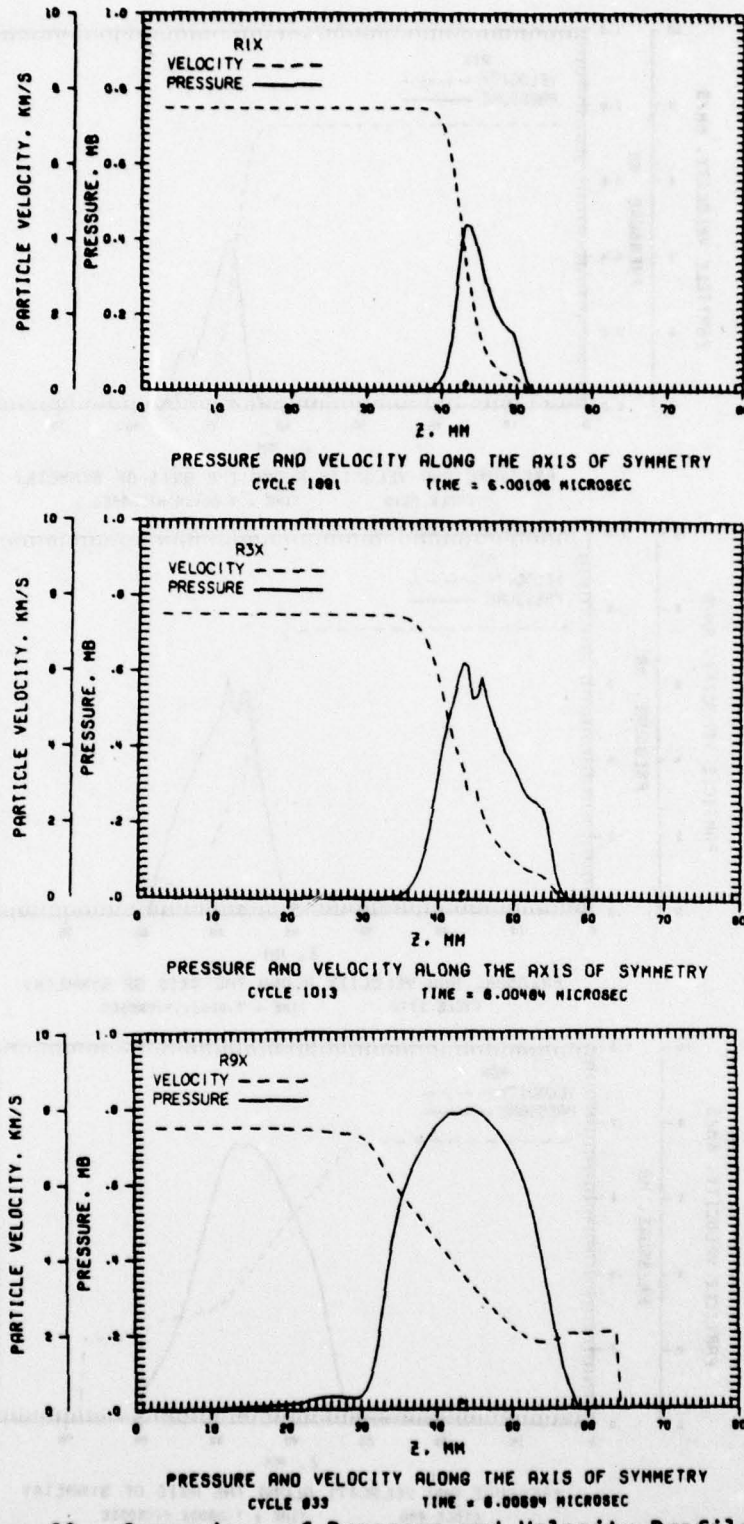


Figure 60. Comparison of Pressure and Velocity Profiles

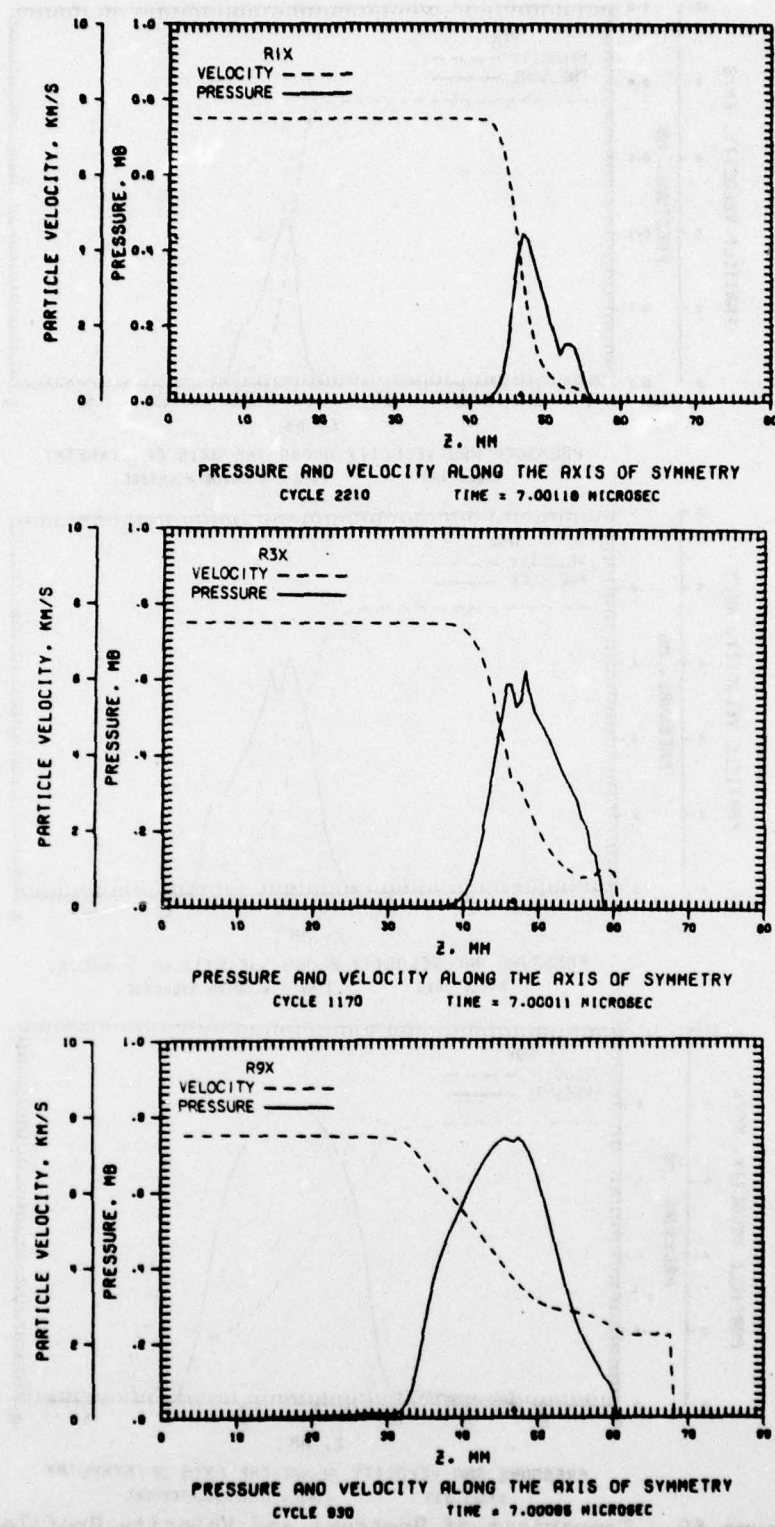


Figure 61. Comparison of Pressure and Velocity Profiles

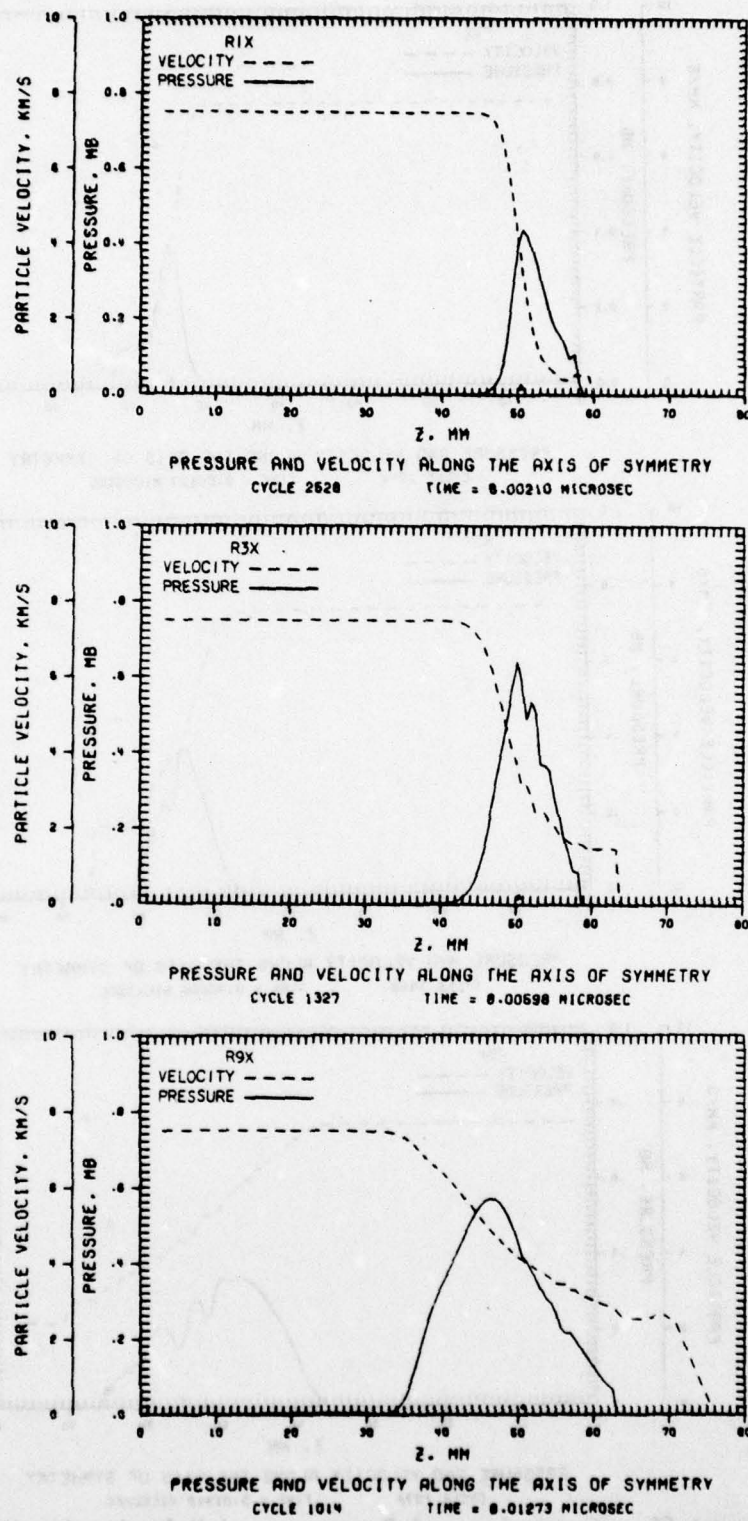


Figure 62. Comparison of Pressure and Velocity Profiles

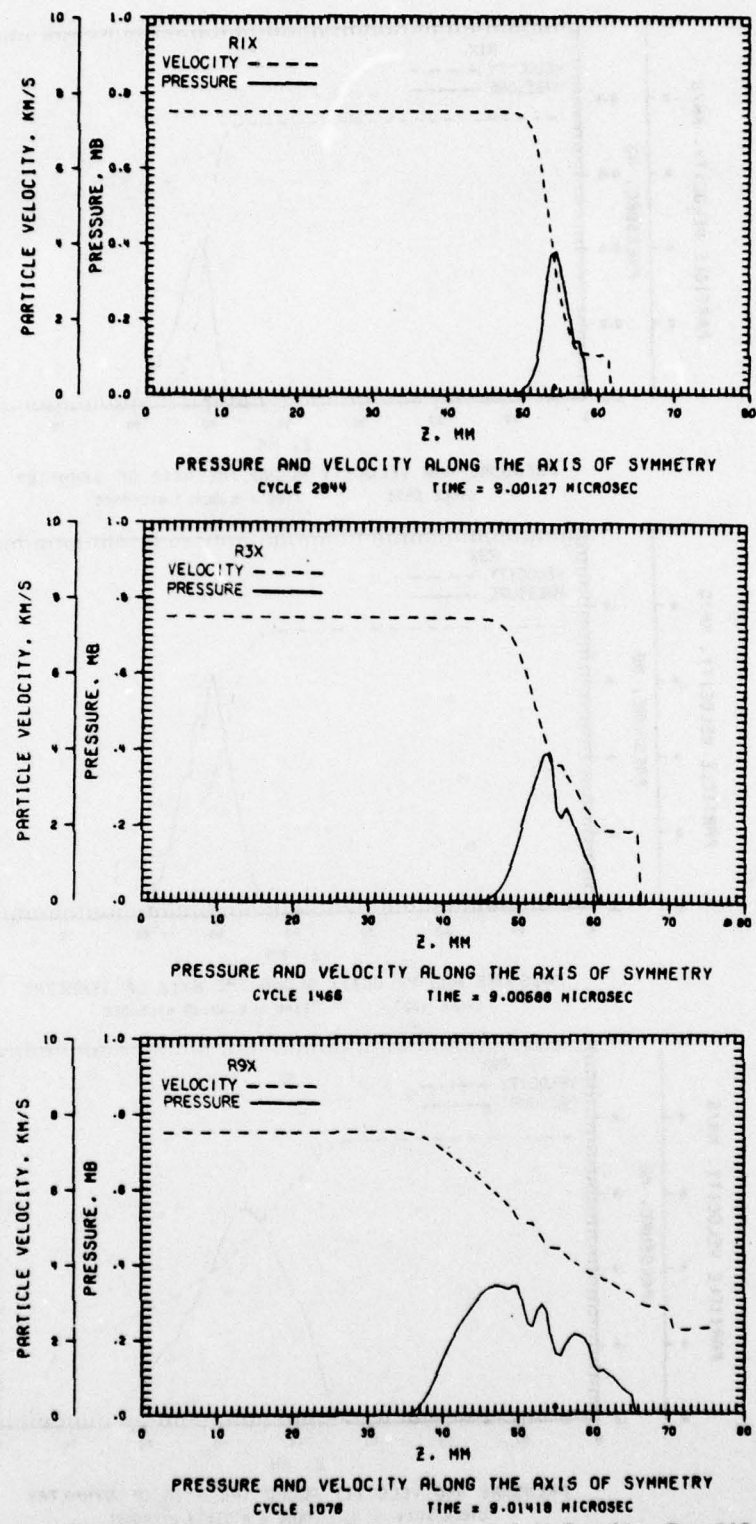


Figure 63. Comparison of Pressure and Velocity Profiles

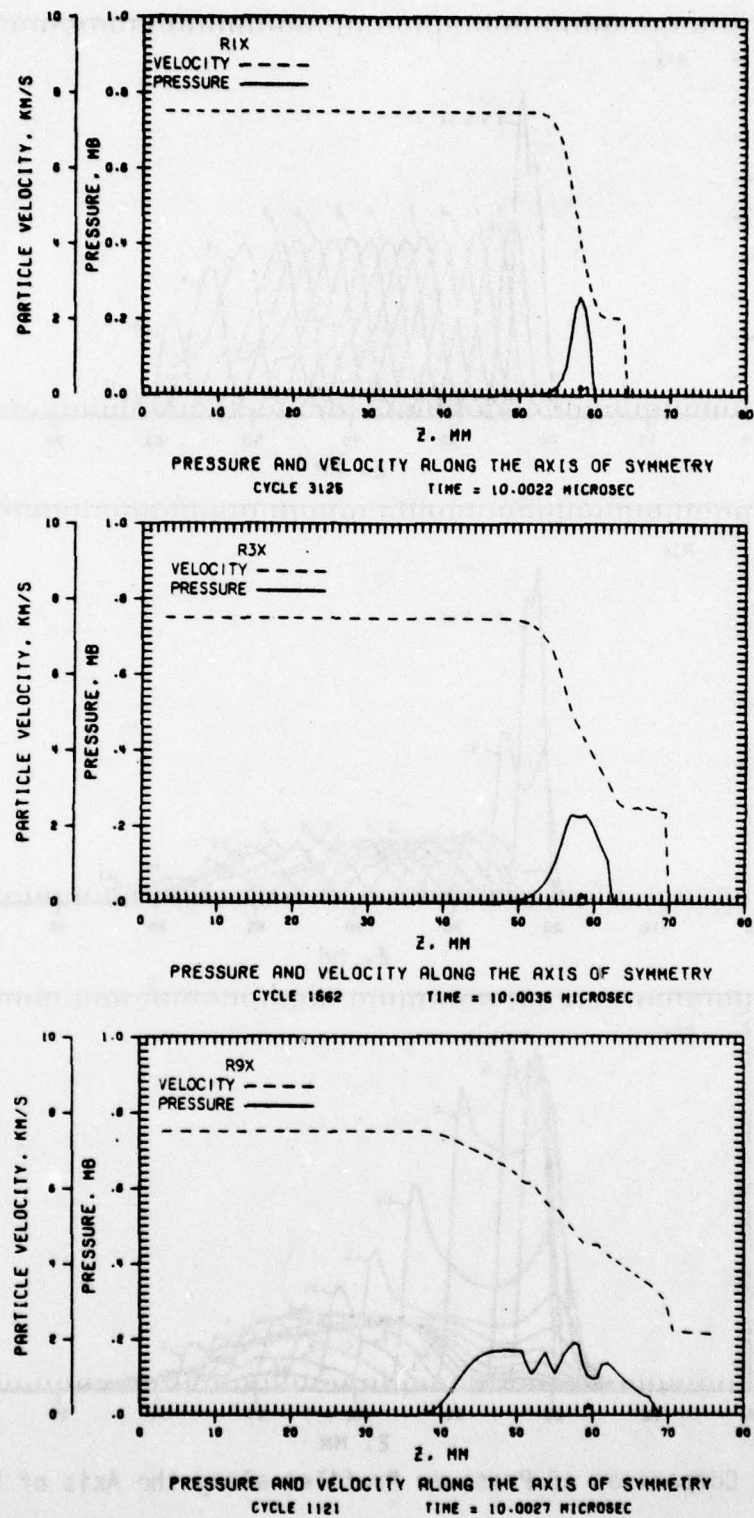


Figure 64. Comparison of Pressure and Velocity Profiles

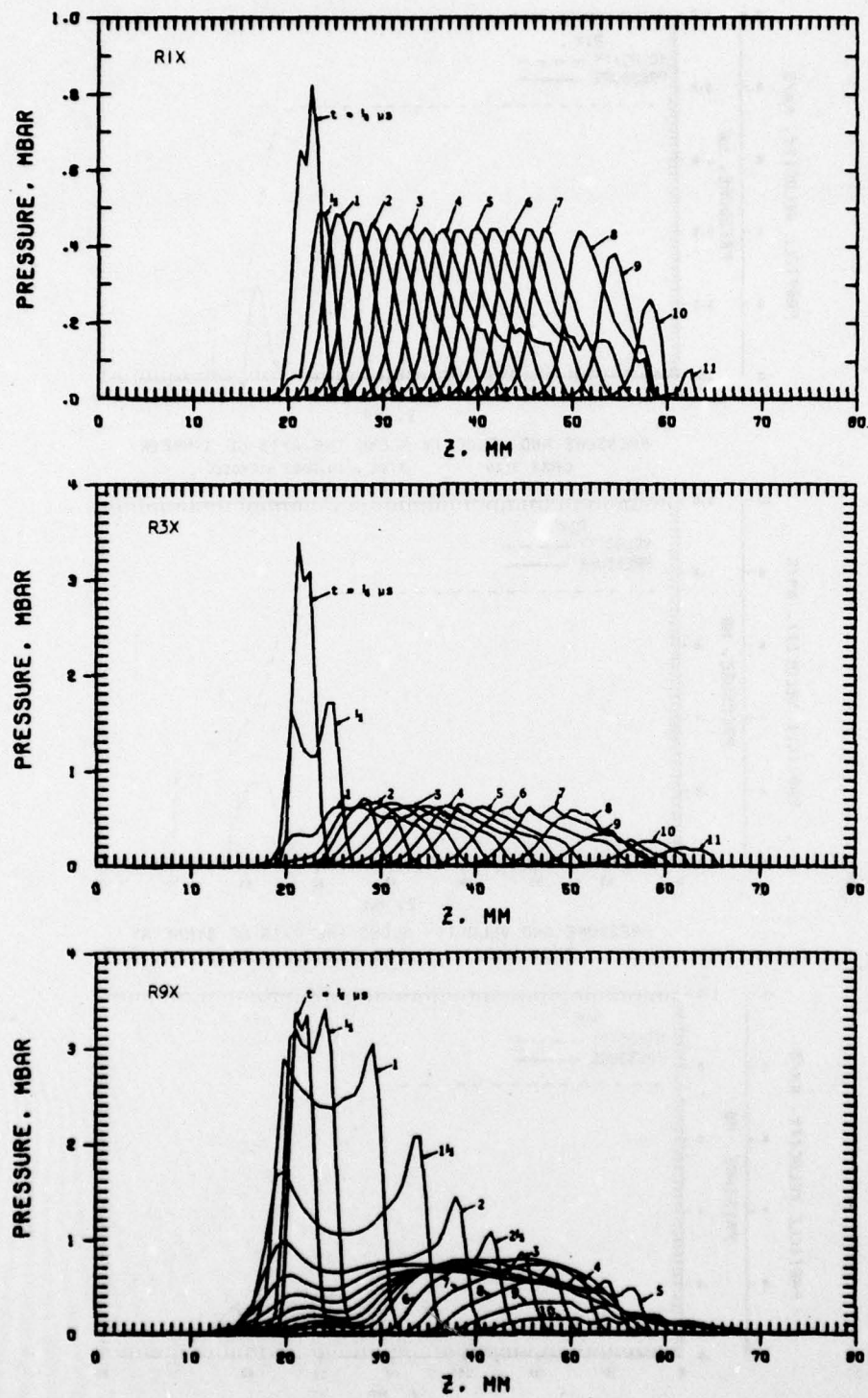


Figure 65. Comparison of Pressure Profiles along the Axis of Symmetry

DISTRIBUTION LIST

<u>No. of Copies</u>	<u>Organization</u>	<u>No. of Copies</u>	<u>Organization</u>
12	Commander Defense Documentation Center ATTN: DDC-TCA Cameron Station Alexandria, VA 22314	2	Commander US Army Mobility Equipment Research & Development Cmd ATTN: Tech Docu Cen, Bldg 315 DRSME-RZT Fort Belvoir, VA 22060
1	Commander US Army Materiel Development and Readiness Command ATTN: DRCDMA-ST 5001 Eisenhower Avenue Alexandria, VA 22333	1	Commander US Army Armament Materiel Readiness Command ATTN: DRSAR-LEP-L, Tech Lib Rock Island, IL 61299
1	Commander US Army Aviation Research and Development Command ATTN: DRSAV-E 12th and Spruce Streets St. Louis, MO 63166	2	Commander US Army Armament Research and Development Command ATTN: Mr. J. Pearson Tech Lib Dover, NJ 07801
1	Director US Army Air Mobility Research and Development Laboratory Ames Research Center Moffett Field, CA 94035	1	Commander US Army Harry Diamond Labs ATTN: DRXDO-TI 2800 Powder Mill Road Adelphi, MD 20783
1	Commander US Army Electronics Command ATTN: DRSEL-RD Fort Monmouth, NJ 07703	1	Commander US Army Materials and Mechanics Research Center ATTN: Tech Lib Watertown, MA 02172
1	Commander US Army Missile Research and Development Command ATTN: DRDMI-R Redstone Arsenal, AL 35809	1	Director US Army TRADOC Systems Analysis Activity ATTN: ATAA-SL, Tech Lib White Sands Missile Range NM 88002
1	Commander US Army Tank Automotive Research & Development Cmd ATTN: DRDTA-RWL Warren, MI 48090	1	Assistant Secretary of the Army (R&D) ATTN: Asst for Research Washington, DC 20310

DISTRIBUTION LIST

<u>No. of Copies</u>	<u>Organization</u>	<u>No. of Copies</u>	<u>Organization</u>
2	Chief of Naval Research Department of the Navy ATTN: Code 427 Code 470 Washington, DC 20325	1	US Air Force Academy ATTN: Code FJS-RL (NC) Tech Lib Colorado Springs, CO 89040
2	Commander US Naval Air Systems Command ATTN: Code AIR-310 Code AIR-350 Washington, DC 20360	1	Commander ATTN: Code OOAMA (MMECB) Hill AFB, UT 84401
1	Commander US Naval Ordnance Systems Cmd ATTN: Code ORD-0332 Washington, DC 20360	1	AFWL (SUL) Kirtland AFB, NM 87116
1	Commander US Naval Surface Weapons Center ATTN: DX-21 Dahlgren, VA 22448	1	AFLC (MMWMC) Wright-Patterson AFB, OH 45433
1	Commander US Naval Surface Weapons Center ATTN: Code 730, Lib Silver Spring, MD 20910	1	AFAL (AVW) Wright-Patterson AFB, OH 45433
1	Commander US Naval Weapons Center ATTN: Code 45, Tech Lib China Lake, CA 93555	1	Director National Aeronautics and Space Administration Langley Research Center Langley Station Hampton, VA 23365
1	Commander US Naval Research Laboratory Washington, DC 20375	2	Director Lawrence Livermore Laboratory ATTN: Mr. M. Wilkins Dr. C. Godfrey P. O. Box 808 Livermore, CA 94550
1	USAF (AFRDDA) Washington, DC 20330	1	Computer Code Consultants ATTN: Mr. W. Johnson 527 Glencrest Drive Solana Beach, CA 92075
1	AFSC (SDW) Andrews AFB Washington, DC 20331	3	Honeywell, Inc. Government and Aerospace Products Division ATTN: Mr. J. Blackburn Dr. G. Johnson Mr. R. Simpson 600 Second Street, NE Hopkins, MN 55343

DISTRIBUTION LIST

<u>No. of Copies</u>	<u>Organization</u>	<u>No. of Copies</u>	<u>Organization</u>
1	Physics International Corp ATTN: Mr. L. Behrmann 2700 Merced Street San Leandro, CA 94577	1	Drexel Institute of Technology Wave Propagation Rsch Center ATTN: Prof. P. Chou 32nd & Chestnut Streets Philadelphia, PA 19104
1	Sandia Laboratories ATTN: Dr. L. Bertholf Albuquerque, NM 87115	1	Southwest Research Institute Dept of Mechanical Sciences ATTN: Mr. A. Wenzel 8500 Culebra Road San Antonio, TX 78228
1	Shock Hydrodynamics ATTN: Dr. L. Zernow 4710 Vineland Avenue North Hollywood, CA 91602	2	University of California Los Alamos Scientific Lab ATTN: Dr. J. M. Walsh Tech Lib P. O. Box 1663 Los Alamos, NM 87545
1	Systems, Science & Software ATTN: Dr. R. Sedgwick P. O. Box 1620 La Jolla, CA 92037		

Aberdeen Proving Ground

Marine Corps Ln Ofc
Dir, USAMSA